

https://dspace.org/

Inverse opals and waveguides to enhance optical absorption and efficiency of photovoltaic devices

Mayimele, Nhluvuko

2022

https://hdl.handle.net/10539/34622

Downloaded from a DSpace repository. https://dspace.org/

Inverse opals and waveguides to enhance optical absorption and efficiency of photovoltaic devices

Doctor of Philosophy

by

Nhluvuko Mayimele

(Student No. 889250)

Supervisors:

Prof. A Quandt

Prof. D Wamwangi



WITS

UNIVERSITY

School of Physics

Faculty of Science

University of the Witwatersrand

July 2021

To my beloved son (*Nhlohlori Rosh*) and my darling mother (*Nxalati Baby*).

In loving memory of *Fortunate Mayimele*

"the big boss".

Declaration

I declare that this written submission represents my ideas in my own words and where others ideas or words have been included, I have adequately cited and referenced the original sources. I also declare that I have adhered to all principles of academic honesty and integrity and have not misrepresented or fabricated or falsified any idea/data/fact/source in my submission. I understand that any violation of the above will be cause for disciplinary action by the Institute and can also evoke penal action from the sources which have thus not been properly cited or from whom proper permission has not been taken when needed.



Date: 22/02/2022

Nhluvuko Mayimele

Student No: 889250

Abstract

Photovoltaic (*PV*) is an environmental friendly technology that promises efficient and effective harvesting of solar energy. Studies shows that, hydrogenated amorphous silicon (*a-Si:H*) has been used as photoactive and doped layers in thin-film solar systems, but its photo-conversion efficiency (*PCE*) is very low due to a thinner absorption layer and light degradation issues. To overcome these constraints, a better understanding of system structure, material properties, and device architecture is needed, as even a small increase in photocurrent has a major impact on photoconversion efficiency. The study explores the effect of using optically active layers onto amorphous silicon-based thin-film solar cells such as plasmonic nanoparticles (*NPs*) and waveguides to modify the optical response. Incorporating spherical shaped silver (*Ag*) or gold (*Au*) nanoparticles (*NPs*) in *PVs* will take full advantage of surface plasmon resonance through the enhancement absorption and scattering of light.

The metallic *NPs* were synthesized through wet chemistry, where hydrogen tetrachloroaurate ($HAuCl_4$) was reduced in 1% trisodium citrate to produce *Au NPs* and with *Ag NPs*, silver nitrate ($AgNO_3$) was reduced in 1% sodium citrate. The TEM and SEM images revealed 20 *nm* spherical *Au/Ag NPs* with plasmon resonance at 500 *nm* and 550 *nm*, respectively.

Silica and titania nanoparicles were synthesized through sol-gel process, in which tetraethylorthosilicat (*TEOS*) and titanium tetraisopropoxide (*TTIP*) were reduced in an ethanolic solution, respectively. SEM images revealed spherically shaped *NPs* for both SiO_2 and TiO_2 with varying sizes. They both showed absorption resonance at 550 *nm* and 680 *nm*, respectively, with absorption intensity increasing, accompanied by blue

shift, as the size of the nanospheres increases (same trend is observed by Tsekov *et al* [1]).

The $Ag@TiO_2$, $Ag@SiO_2$ and $Au@SiO_2$ core–shell *NPs* were also synthesized by sol-gel technique (modified Stöber method), TEM images showed 58 *nm* spherical core-shell *NPs* having a shell thickness of about 20 *nm* and core of 20 *nm* for $Ag@SiO_2$ and $Au@SiO_2$ core-shell *NPs*. They showed a plasmon resonance at 500 *nm* and 550 *nm* respectively, with a higher absorption intensity, while spherical 50 *nm* $Ag@TiO_2$ core-shell *NPs* showed multiple plasmon resonance between 500 *nm* and 650 *nm*.

Furthermore, waveguides were studied where Silica (SiO_2), Titania (TiO_2) and SiO_2:TiO_2 waveguides films were fabricated through sol-gel technique. The wavegiudes thickness was varied from 30 *nm* to 300 *nm*. They also showed a transmittance between 30% and 60% at 460 *nm* and also exhibited absorption at 450 *nm* to 500 *nm*, as result of the film thickness increase.

The surface plasmon resonance by *Ag/Au NPs* and core-shell *NPs* ($Ag@TiO_2$, $Ag@SiO_2$, TiO_2, SiO_2) has been modelled using MATLAB software based on Mie theory, to calculate the absorption and scattering cross-sections. The simulations showed spherical *Ag/Au NPs* and $Ag/Au@SiO_2$ core-shell *NPs* have plasmon resonance between 400 *nm* and 550 *nm* respectively, with an increased absorption intensity. The $Ag/Au@TiO_2$ core-shell *NPs* showed a plasmon resonance between 500 *nm* and 750 *nm* respectively, also an improved absorption intensity. The optical absorption from simulation for $Ag@SiO_2$ core-shell *NPs* is in good agreement with experimental data for the same core-shell dimensions and structures.

The *PV* performances of *a-Si* solar cells incorporated with metallic *NPs*, core-shell *NPs* and waveguide were investigated. The result revealed that the *PCE* of the *PV* devices were all significantly enhanced due to the plasmonic effect of the noble metal nanostructures. For example, Under AM1.5 illumination, a *PCE* of 9.86% was obtained in *a-Si* solar cell incorporated with $Ag@TiO_2$ core-shell *NPs*, while a reference *a-Si* solar cell had a *PCE* of 6.73%. The *PCE* of *a-Si* solar cell incorporated with SiO_2 waveguide was increase to 7.53%, which is a good improvement compared to the reference *a-Si* solar cell with the *PCE* of 6.74% this might have occurred due to the carrier recombination

resulting from the fill factor which improved from 50% up to 55%.

Finally, numerical modelling of crystal-silicon (*c-Si*) solar cell was studied as to improve the photon absorption efficiency. Device simulations were carried out by solving Poisson equations for multi-dimensional systems incorporating Plasmonic resonance dependent core-shell *NPs* or nanostructures to calculate drift and diffusion currents. The *c-Si* solar cell were incorporated with $Ag@TiO_2$, $Ag@SiO_2$, TiO_2, SiO_2 core-shell *NPs* and *Ag NPs* at the top/front end of the device, to promote photon/light trapping and or forward scattering on the device. The simulation showed an increase on the flow of current as the core-shell *NPs* were introduced onto the device and each of these core-shell *NPs* had a unique absorption coefficient. The results predicted the highest increase in *PCE* of 28.05% in a *c-Si* solar cell with $Ag@TiO_2$ core-shell *NPs*.

List of Publications

Journals

1. N. Mayimele, F. Otieno, S.R. Naidoo, D. Wamwangi and A. Quandt "*Efficiency enhancement of organic solar cell using surface Plasmon resonance effects of Ag nanoparticles*": *Optical and Quantum Electronics. 2021 Nov;53(11):1-4.*

2. S. Kumalo, N. Mayimele, A. Quandt, D. Wamwangi, D. Billing, A. Shnier and R. Erasmus "Plasmonics and Magnetoplasmonics as Approaches to Enhance Photo-Conversion Efficiency of PV Devices": *submitted to Optical Materials.*

3. N. Mayimele, S. Kumalo, A. Quandt, D. Wamwangi "Photon management using plasmonic and photonic structures in a-Si based solar cells": *under review to be submitted to Optical Materials*

Conferences

1. *National conferences:* Center of Excellence-Strong Materials Student Presentation:

(a) *Poster Presentation:* N. Mayimele, A. Quandt, D. Wamwangi, F. Otieno and M. Naidoo "Approaches to enhance optical absorption and efficiency of photovoltaic device" DST-NRF Centre of Excellence in Strong Materials, 2018, Johannesburg, South Africa

(b) *Oral Presentation:* N. Mayimele, A. Quandt and D. Wamwangi "Solar cell efficiency enhancement" DST-NRF Centre of Excellence in Strong Materials, 2019, Johannesburg, South Africa

(c) *Poster Presentation:* N. Mayimele, A. Quandt and D. Wamwangi "SiO_2 opals and $Ag@SiO_2$ core-shell NPs to improve light trapping on OPV/PV devices" DST-NRF Centre of Excellence in Strong Materials, 2020, Johannesburg, South Africa

(d) N. Mayimele, A. Quandt and D. Wamwangi "SiO2 opals and Ag@SiO2 core shell to improve light trapping on OPV/PV devices" DST-NRF Centre of Excellence in Strong Materials, 2020, Johannesburg, South Africa

2. *International conferences:* 3rd Generation PV in the Developing World conference:

(a) *Poster Presentation:* N. Mayimele, S. Kumalo, A. Quandt and D. Wamwangi "Photon management using Plasmonic, opal and waveguide structures in Si based solar cells" 3rd Generation PV in the Developing World, 2021, Durham, United Kingdom

Acknowledgments

I wish to record a deep sense of gratitude to Prof. A Quandt and Prof. D Wamwangi, my supervisors for their valuable guidance and continued support at every stage of my research and studies to complete my Ph.D. I would also like to thank the Center of Excellence for Strong Materials (CoE-SM DST/NRF) for their financial support which allowed me to achieve this accomplishment. To the Schools of Physics and Chemistry for provision of research infrastructure. Dr. F Otieno and Mr. S Kumalo thank you for assisting with the experiments and further analysis of the result. To my group, which is led by Prof. A. Quandt here at Wits, thank you for the support and time you gave me to become what I am today, as well the Materials for Energy Research Group (MERG). I would further like to thank Mr. TM Ngobeni, a man close to my heart for motivating and supporting all the time. My in-laws, friends, Family and Mr. MA Mayimele for support you gave me. Special thanks to Mrs. ER Nukeri and Mrs. MS Ngobeni (*mother in-law*) for the love and support. To the almighty God.

Contents

Declaration i

Abstract i

List of Publications iv

Acknowledgments vi

List of Tables xi

List of Figures xii

1 Introduction 1

1.1 Background 1

1.2 Problem statement 5

1.3 Motivation 6

1.4 Aim 7

1.5 Research objectives 7

1.6 Thesis outline 8

2 Photovoltaics in a Nutshell 10

2.1 Introduction 10

2.2 Renewable energy generation 10

2.3 The Fundamentals of Solar Cells. 14

2.3.1 Shockley-Queisser Limit for *P-N* junction 17

2.3.2 The External Quantum Efficiency 20
2.3.3 Surface Recombination Effects 21
2.4 Metallic *NPs* on the solar cell 25
2.5 Core-Shell *NPs* in solar cells 27
2.6 Waveguides to guide light in a solar cell 28

3 Numerical modelling of *PV* devices 32
3.1 Introduction 32
3.2 Theoretical principles of plasmonic resonance in single and core-shell *NPs* 32
3.2.1 Theoretical point of view 32
3.2.2 Optical data modeling results. 36
3.3 The *J–V* characteristics simulations of the solar cells 44
3.3.1 *J–V* Simulation Methods 44
3.3.2 *J–V* Simulation Results 48
3.4 Conclusion 52

4 *PV* devices incorporated with metallic and core-shell *NPs* 54
4.1 Introduction 54
4.2 Materials 59
4.3 Sample Preparation 59
4.3.1 Synthesis of *Ag* nanoparticles 59
4.3.2 Synthesis of *Au* nanoparticles 60
4.3.3 Synthesis of SiO_2 nanospheres 60
4.3.4 Synthesis of $Ag@SiO_2$ core-shell *NPs* 60
4.3.5 Synthesis of $Au@SiO_2$ core-shell *NPs* 61
4.3.6 Synthesis of TiO_2 *NPs* 61

4.3.7 Synthesis of $Ag@TiO_2$ core-shell *NPs* 61
4.4 Morphology analysis: 62
4.4.1 TEM Morphology analysis of *Ag NPs* 63
4.4.2 TEM Morphology analysis of *Au NPs* 64
4.4.3 SEM Morphology analysis of SiO_2 nanospheres 65
4.4.4 SEM Morphology analysis of $Ag@SiO_2$ core-shell *NPs* 69
4.4.5 TEM Morphology analysis of $Au@SiO_2$ core-shell *NPs* 70
4.5 Optical Properties Analysis 72
4.6 The *J–V* characteristics 80
4.6.1 Introduction 80
4.6.2 The *J–V* characterization for *Ag NPs* SiO_2 and $Ag@SiO_2$ core-shell *NPs* on *a-Si* solar cell 80
4.6.3 The *J–V* characteristics *Ag NPs*, TiO_2 *NPs* and $Ag@TiO_2$ core-shell *NPs* on *a-Si* solar cell 85
4.6.4 Dark current *I–V* characteristics 88
4.7 Conclusion 92

5 *PV* Devices with Silica Titania Waveguides **94**
5.1 Introduction 94
5.2 Resonant Waveguide Gratings *(RWGs)* 95
5.3 Sample Preparation 97
5.3.1 Synthesis of SiO_2 waveguides 97
5.3.2 Synthesis of TiO_2 waveguides 98
5.3.3 Synthesis of SiO_2:TiO_2 waveguides 98
5.4 Optical Properties Analysis 99
5.4.1 Transmittance of the *WG* 99

5.4.2 Absorption of the *WG* 102

5.4.3 The refractive index 103

5.5 The *J–V* characterization for silica waveguides on *a-Si* solar cell 107

5.6 Conclusion 108

6 Summary and Outlook **111**

References **115**

Appendix A Techniques and methods applied **138**

A.1 Experimental techniques 138

A.1.1 Sol-gel method 138

A.1.2 Depositing methods 139

A.2 Data analysis techniques 141

A.2.1 The UV-Vis spectrophotometer analysis 141

A.2.2 *I-V* characteristics of photovoltaic device analysis 141

List of Tables

3.1 Parameters used to calculate absorption and scattering cross-section of *Au/Ag NPs*, $Au/Ag@SiO_2$ and $Au/Ag@TiO_2$ core shells *NPs* 36

3.2 The parameters used in simulating the *J-V* characteristics for a single crystalline silicon solar cell 49

3.3 The summary of *J-V* characteristics for a single crystalline silicon solar cell 52

4.1 Temperature dependence on the diameter and shape of single and core-shell nanoparticles 72

4.2 Parameters calculated from *J-V* curve a commercial *a-Si* solar cells . . 84

4.3 Parameters calculated from *J-V* curve from the enhanced commercial *a-Si* solar cells. 87

4.4 Parameters calculated from Semi-Log dark current of the enhanced commercial *a-Si* solar cells. 91

5.1 The calculated refractive index 106

5.2 Parameters calculated from *J-V* curve from the doped commercial *a-Si* solar cells. 110

List of Figures

3.2 The absorption and scattering cross-section of 30 *nm* spherical *Ag And Au NPs* 37

3.3 The absorption and scattering cross-section of 30 *nm* spherical *Ag and Au NPs* 38

3.4 The absorption and scattering cross-section of $Ag/Au@SiO_2$ core-shells *NPs* having different shell thickness with the same core size of 30 *nm*. . 38

3.5 The absorption and scattering cross-section of $Ag/Au@TiO_2$ core-shells *NPs* having different shell thickness with the same core size of 30 *nm*. . 40

3.6 The absorption and scattering cross-section of $Ag/Au@SiO_2$ core-shells having different core sizes with the same shell thickness of 30 *nm*. . . . 42

3.7 The absorption and scattering cross-section of $Ag/Au@TiO_2$ core-shell *NPs* having different core sizes with the same shell thickness of 30 *nm*. 43

4.3 TEM image (a) of *Ag NPs* distributed on the *Cu* grid surface at magnification of 200× and image (b) shows zoomed in image of *Ag NPs* with 20 *nm* diameter shown in image (c) from the histogram showing of the average size of *Ag NPs*. 63

4.4 TEM image (a) of *Au NPs* distributed on the *Cu* grid surface at magnification of 50× and image (b) shows zoomed in image of *Au NPs* with 20 *nm* diameter shown in the histogram of image (c) 64

4.5 The SEM image (a) shows the resulting film comprising of SiO_2 nanospheres (thermally treated at 70 $^{\circ}C$), image (b) shows the uniformly distributed *NPs* on the surface and image (c) shows histogram of the average size of SiO_2 nanospheres with a diameter of 35 *nm*. 65

4.6 Image (a) shows the SiO_2 (thermally treated at 100 $^{\circ}C$) spheres, image (b) shows uniformly shaped spheres magnified. Image (c) shows the histogram of the average size of SiO_2 *NPs* with a diameter of 65.8 *nm* . 66

4.7 SEM image (a) shows the SiO_2 nanospheres (which were thermally treated at 150 $^{\circ}C$), image (b) shows how the spheres are distributed on the surface and image (c) shows the histogram of the average size of SiO_2 *NPs* with a diameter of 72.28 *nm*. 67

4.8 SEM image (a) shows the SiO_2 nanospheres (thermally treated at 200 $^{\circ}C$) uniformly distributed, image (b) and (c) shows the magnified nanosphere uniformly distributed and ahaped *NPs*. Image (d) show the histogram of the average size of SiO_2 *NPs* with a diameter of 85.51 *nm*. 68

4.10 TEM images (a) showing the $Ag@SiO_2$ (thermally treated at 100 $^{\circ}C$) spheres non-uniformly distributed and shaped. Image (b) shows the histogram of the average size of the core-shell *NPs* with a diameter of 60 *nm* 70

4.11 TEM images (a) showing the $Au@SiO_2$ core-shell *NPs* (thermally treated at 100 $^{\circ}C$). Image (b) is the histogram showing the average size of the core-shell *NPs* 71

4.12 Absorption spectra of $Ag@SiO_2$ core-shell *NPs* deposited with two different methods (dip and spin coating). 73

4.13 The absorption spectra of spherical like SiO_2 *NPs* synthesized at 70, 100, 150 and 200 $^{\circ}C$ respectively 75

4.14 The absorption of *Au NPs* and $Au@SiO_2$ core-shell *NPs* having different *Au NPs* concentrations. 76

4.15 Absorption spectra of SiO_2 nanospheres, *Ag NPs* and $Ag@SiO_2$ core-shell *NPs*. 76

4.16 Absorption spectra of *Ag NPs*, TiO_2 *NPs* and $Ag@TiO_2$ core shells *NPs*. 77

4.17 The transmittance of spherical Ag NPs, SiO_2 NPs and $Ag@SiO_2$ core-shell NPs deposited on a microscopic glass slide. 79

4.19 The J-V curve of a commercial a-Si solar cell incorporated with Ag NPs, SiO_2 and $Ag@SiO_2$ core-shell NPs. 82

4.20 The J-V curve of a commercial a-Si solar incorporated with Ag NPs, $Ag@TiO_2$ and TiO_2 core-shell NPs 85

4.21 Semi-Log dark current of a commercial a-Si solar incorporated with Ag NPs, SiO_2 NPs and $Ag@SiO_2$ core-shell NPs. 89

4.22 Semi-Log dark current flowing in a commercial a-Si solar incorporated with Ag NPs, TiO_2 NPs and $Ag@TiO_2$ core-shell NPs. 90

5.2 Transmission spectra of silica waveguides with different number of layers dip coated on a microscope glass slab, that were thermal treated after a layer or all layers were deposited. 100

5.3 The transmission spectra of SiO_2, TiO_2 and $SiO_2 : TiO_2$ waveguides. . . 101

5.4 The absorption spectra of SiO_2, TiO_2 and $SiO_2 : TiO_2$ waveguides. . . . 103

5.5 The J-V characteristics of commercial a-Si solar with silica waveguide . 107

Chapter 1

Introduction

1.1 Background

Current efforts to find long term, environmentally friendly solutions to power production has necessitated harnessing of light energy from the sun. The conversion of sunlight into electricity is known as photovoltaics *(PVs)*. Research indicates that *PVs* is a promising technology which allows for a large scale production of electrical power. Currently, *PV* production exceeds 637–653 gigawatts (*GW*) world wide [2, 3] which suggest to be one of the best way to solve energy problems (see Figure 1.1). The solar-cells market at the moment is mostly focused on the costly crystalline silicon in form of wafers, which are 180–300 μm thick, which amounts to an inefficient and thus costly waste of precious bulk material [4]. This then attracts the growth or study of thin-film solar cells, which are about 1–2 μm thick, and are easily deposited on cheap module-sized substrates such as plastic, stainless steel or glass [5]. Thin-film solar cells are composed of a variety of semiconductors that are either amorphous and polycrystalline such as *Si, GaAs, CdTe* or $CuInSe_2$, as well as inorganic semiconductors [5, 6].

However the thin-film solar-cells innovations still have severe shortcomings, such as bandgap mismatched to the solar emission spectrum which lead to insufficient light absorption [5]. To date, several light trapping features aimed at improving photon conversion efficiency on thin-film solar cells have been developed. These include nanowires, nanocones, photonic crystals, nanoparticles and waveguides [7]. Improving light absorption in thin-film solar cell using metallic nanostructures is based on surface plasmons: i.e. optical excitations of the conduction electrons at the interface between a metal and a

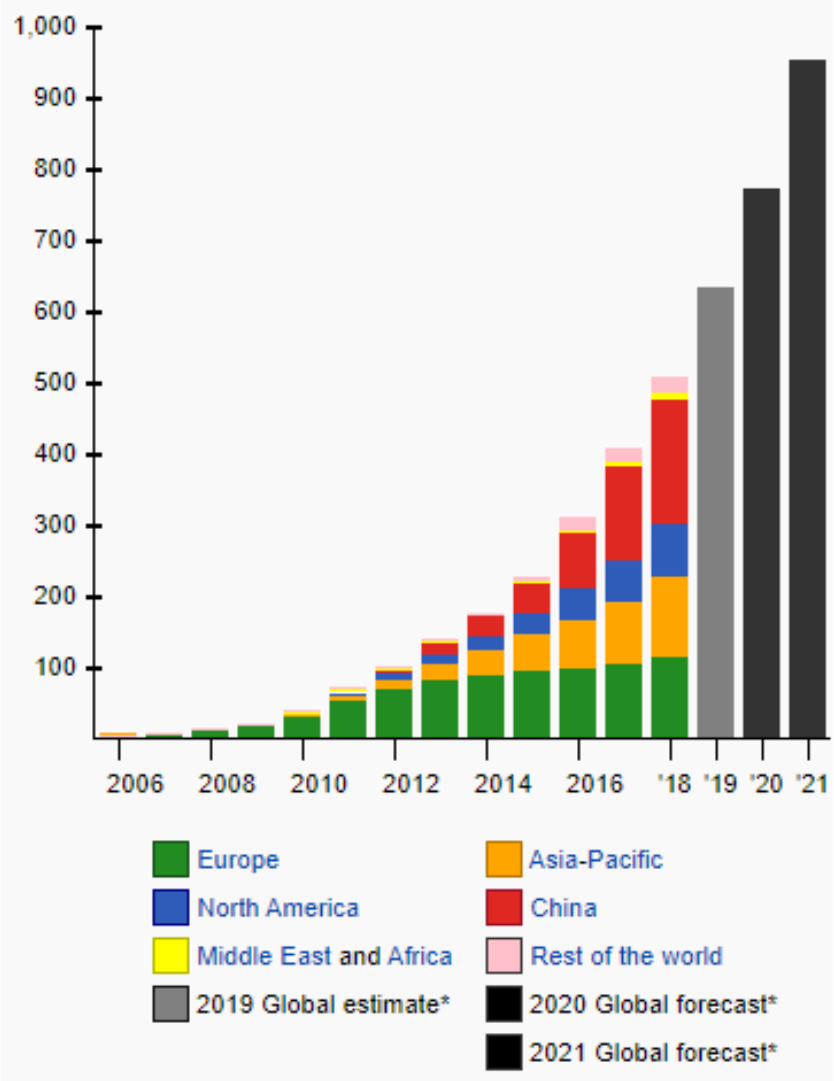


Figure 1.1: Worldwide growth of photovoltaics [3] .

dielectric [8]. Through a definitive design and synthesis of these metallo-dielectric structures, light can be concentrated and 'folded' into a thin semiconductor layer, thereby increasing photo absorption. Both, localized surface plasmons excited in metal nanoparticles, and surface plasmon polaritons *(SPPs)* propagating at the metal/semiconductor interface are of interest to this study [5, 8].

The plasmonic resonance effect of metallic nanoparticles (*NPs*) have already been implemented in solar cells to enhance the photo–conversion efficiency by at least 10% [9]. However, the surface of metallic *NPs* can lead to quenching effects due to the interaction of metallic *NPs* with their environment [10, 11]. Also, metallic *NPs* deposited on solar cells undergo thermalization over time, which then reduces the effectiveness of

the device. Covering such metallic *NPs* with one or more dielectric coatings such as core-shells structure could be effective in addressing these issues, [12]. Additionally, encapsulating dielectric shells allow for changes in the plasmonic edge thereby enabling resonant absorption of the photoactive layer. Introducing silica (SiO_2) photonic sphere containing gold *(Au)* or silver *(Ag) NPs* or any other metallic *NPs* [13, 14] is one of the strategies to incorporate tunable plasmonic resonance with reduced degradation of the metal plasmonic nanostructures.

Advantages of using SiO_2 as core-shells *NPs* embedded with metallic *NPs* include, but are not limited to [15, 16, 17]:

1. Preventing metallic *NPs* from interacting with oxygen or acidic environment,
2. Influencing the plasmonic behaviour by changing the dielectric environment of *Au/Ag NPs*,
3. Preventing *Ag/Au NPs* core from agglomeration and enhance their chemical stability and optical transparency,
4. Improving the water dispersibility of *Au/Ag NPs*,
5. Employing the ability to tune the resonance band of the noble metal nanostructures,
6. Lowering the in degradation of charge carrier mobility, usually caused by local recombination of excitons and other perturbations of the electronic band structure. To this end, core–shell nanoparticles consisting of metallic *(Au, Ag or Cu)* core coated with an insulating dielectric shell-layer (e.g., of SiO_2) can be applied in photovoltaic devices.

Furthermore thin film based solar cells present a compromise between bulk properties like the absorption coefficient and the thickness of the absorber active layer. This calls for the implementation of novel light trapping and scattering mechanisms to the photovoltaic device [18]. Since resonant light coupling to waveguide modes is only feasible in small spectral regions, an engineered light-trapping system is required to effectively address the entire spectrum. Periodic light trapping textures have shown significant improvements to the external quantum efficiency *(EQE)* of solar cells [7].

Note that, improvement in EQE has also been demonstrated by solar cells with

random textures [19]. However, they remain below the values for solar cells with periodic textures at their resonances due to the lack of optical resonance. Light coupling to waveguide modes in a system with disordered gratings usually shows a spectral expansion.

Various techniques such as, ion exchange in glass, chemical vapor deposition *(PECVD, LPCVD)* and the sol-gel method, can be used for the production of waveguides [20]. Moreover, dip coating of sol-gel fabricated waveguides has proven to be a suitable method of synthesis, due to its capability to form waveguides at low temperatures [21]. Depending on the drawing speed, sintering temperature of waveguides varying thickness can be fabricated. The key parameters (refractive index and thickness) are determined by prism coupling techniques [22, 23] and morphology control.

Waveguides in photovoltaics, can be fabricated in many shapes and sizes, can be used as convenient, flexible energy source require heavy cover glasses and alumina frames. The optimized device exhibited a *PCE* of close to 6% and the predicted *PCEs* are extremely high (up to 18%) [24, 25].

Further improvements may come from doping the waveguides with inexpensive luminescent species, leading to luminescent solar concentrators (*LSCs*) which require no solar tracking. They have recently gained interest because of their potential for achieving high optical concentrations with a flat-panel geometry [26].

The advantage of *LSCs* rest on the complete internal reflection, achieved when incident light is absorbed by the luminescent species which is then re-emitted at a blue/red-shifted wavelength. As a result, only a fraction of the emission is retained in the waveguide [27]. Ideal luminescent species should demonstrate the following spectroscopic properties: (1) broad spectral absorption with high absorption efficiency, (2) matching the emitted photons to the spectral response of the edge-attached solar cells, (3) high photoluminescence quantum yield *(PLQY)*, and (4) minimal spectral overlap or large Stokes shift [28].

Unlike conventional concentrators, *LSCs* concentrate both direct and diffuse light, potentially produce a high optical concentration of up to 33.6% [29, 30]. Some portion

of the incident light is caught inside the substrate and guided through internal reflection towards a *PV* cells set at the edge of the waveguide, where it is converted into electricity [31]. Since Webber and Lambe introduced the concept in 1976, several highly efficient *LSCs* have been developed [29, 32] including flexible *LSCs*, which can be obtained by introducing rubber elastomers (such as silicones) and plastic fibers as waveguides [33, 28]. The flexible *LSCs* provides more aesthetic design options in the built environment [28]. Slooff et al. reported the current world-record photoconversion efficiency (*PCE*) is of 7.1%, which was achieved by integrating four *GaAs* cells into an *LSCs III–V* cells. More recently, Desmet et al. used single-crystaline silicon solar cells, which are cheaper than *III–V* cells, to fabricate *LSCs* with a high *PCE* of 4.2% [32, 34]. For this study amorphous silicon *(a-Si)* solar cells considered due to the following reasons:

1. They are the most developed thin film solar cells, because they can be easily deposited on a standard glass substrate through various techniques,
2. Low production costs [35],
3. Their higher optical absorption, makes it easier to incorporate plasmon focused light management schemes on them. This will then allow enhancement in optical absorption efficiencies for commercial *a-Si:H* solar cells in the current market. While keeping production costs as low as possible, which is a vital factor in ensuring the low-cost commercial viability of thin-film solar-cell-based products,
4. Having large scale *PV* plants based on rigid and robust panels will dominate global *PVs* markets,
5. Most importantly, thin film solar cells are easier to produce compared to standard *c-Si* solar cells.

1.2 Problem statement

The efficiency of *a-Si* solar cells is limited, namely; (a) short carrier lifetimes (450 *ps*) in the conduction band, due to recombination leading to charge carrier losses, and (b) relatively sharp absorption bands and in, some cases their mismatch to the maximum

solar emission flux limits the efficient photon harvesting from the sun01 [36].

However they offer a better potential solution to the exigent energy challenges as well as a means to reducing environmental pollution resulting from reliance on fossil fuel. For the widespread usage of *a-Si PVs*, high module efficiency (greater than 15%) and lifetimes suitable for applications are required 00[37, 38].

There is a need to improve light harvesting materials, cost effective device structures, processing methods and modification of the optoelectronic properties of the active layer in *PV* devices are crucial in enhancing efficiency. This includes introducing plasmonics *NPs*, waveguides and photonic crystals or opals as light management schemes in *PV* devices.

1.3 Motivation

PV energy conversion characteristics has ecological effect. As it stands, there are long-term possibilities to replace the current conventional electricity production with *PV* produced electricity. The technological foundation for off-grid electricity determines how far photovoltaics may advance. Currently there's a low power distribution or power supply of *PV* systems in industrial systems due to expensive *PV* systems with good *PCE*, and cheaper solar cells having low *PCE*. This then open a room to improve the *PCE* of less expensive solar cells, which will then lower electricity costs while also being environmentally beneficial. This can achieved by using improved optical absorption and scattering approaches to increase the *PCE* of a low-cost photovoltaic system such as *a-Si* solar cells, which explores and quantifies ways to augment the design of inorganic and organic solar cells in order to increase their efficiencies using: plasmonic nanoparticles, photonic crystals, waveguides and luminescent waveguides. This will result in affordable large-scale production *PV* plants with high efficiencies based on rigid and durable panels dominating the global *PV* industry.

1.4 Aim

The aim of the project was to increase the photon conversion efficiency of a cheap photovoltaic device using several light management schemes through the use of photonic crystals (such as silica and titania *NPs*), core-shell *NPs* (such as $Ag@SiO_2$, $Ag@TiO_2$) and metallic *NPs*. These light managements schemes make use of the plasmonic effects to enhance light trapping on commercial solar solar cells. Metallic *NPs* were fabricated by wet chemistry and sol-gel methods. We therefore also aimed to improve efficiency of sub-receiver modules by combining a single junction solar cells and applying silica and titania waveguides to guide light in a solar spectral range of 300–1800 *nm* onto the device. Furthermore, intermediate reflective layers (*IRL*) were explored to modify the photon distribution in the device.

1.5 Research objectives

The thesis focuses on experimental studies and numerical modelling of *Ag/Au NPs*, core-shell *NPs* and waveguides for the improvement of commercial *a-Si* solar cells.

The experimental objectives of the project are outlined as follows:

- Synthesis of *Au/Ag* nanoparticles using wet chemistry route,
- Synthesis of silica-titania, waveguides using the sol–gel technique,
- Synthesis of photonic crystal (SiO_2 and TiO_2) and core-shell *NPs* ($Ag/Au@SiO_2$ and $Ag/Au@TiO_2$) using sol–gel technique,
- Incorporation of the *Ag/Au NPs* in the *PV* device to promote scattering and absorption of light through plasmonic effect,
- Incorporation, of photonic crystal (SiO_2 and TiO_2) or core-shell *NPs* ($Ag/Au@SiO_2$ and $Ag/Au@TiO_2$) in the device acting as intermediate reflectors to balance the currents,
- Incorporation, of silica waveguides in the device to improve efficiency of sub-

receiver modules through up and down shifting.

The theoretical/numerical objectives of this study are:

- Use Matlab code to simulate the absorption and scattering coefficients of *Ag/Au NP*, photonic crystal (SiO_2 and TiO_2) and core-shells ($Ag/Au@SiO_2$ and $Ag/Au@TiO_2$) *NPs*.
- Employ*PV* device simulation to determine the drift and diffusion currents which are modified by plasmonic resonances due to the presence of core-shell nanoparticles.

1.6 Thesis outline

The structure of the thesis is divided in six chapters as follows;

- ✓ Chapter-1: Discusses the general impact of photovoltaics. The principle concepts and the light harnessing features to trap efficient photons are described and the motivations and the objectives that lead to the present research are stated in some detail.
- ✓ Chapter-2: Elucidates the working principle and important parameters of solar cells. The chapter further gives a survey of the current work done to improve the efficiency of the *PV* devices and points out future advances.
- ✓ Chapter-3: Describes the theory used in the simulation of solar cells embedded with plasmonic *NPs* and core-shell *NPs*. The various developments/applications as well as detailed derivations of the study are included in this chapter.
- ✓ Chapter-4: Presents the synthesis of *Ag/Au NPs*, SiO_2/TiO_2 *NPs* and $Ag/Au@SiO_2/TiO_2$ core-shell *NPs*. These *NPs* are then implemented on a commercial *a-Si* solar cell and experimental studies are carried out to illustrate *PCE* enhancement.
- ✓ Chapter-5: Focuses specifically on the synthesis and optical analysis of SiO_2/TiO_2 waveguides, and their implementations in commercial solar cells.
- ✓ Chapter-6: Final conclusions are drawn in this chapter. We also suggest possible

continuations of this research.

Chapter 2

Photovoltaics in a Nutshell

2.1 Introduction

In this Chapter, the discussions focuses on the function of a basic solar cell and ongoing efforts to improve the efficiency of *PV* devices. The principle mechanisms of light trapping and the geometry needed to trap sufficient photons are described. A comprehensive exploration of all critical factors affecting the surface plasmon signal and absorption of core-shell *NPs* or *PhCs* on *PV* module surfaces which were collected for this study are also in this chapter.

2.2 Renewable energy generation

Ever since the beginning of industrial revolution, fossil fuels have become the dominant energy resources that have been utilized in most nations of the world. This has significant ramifications for the environment, and also affects the well being of the global population. The conversion and subsequent consumption of these petroleum derivatives as energy sources have lead to the depletion of 75% of the ozone layer. Besides, the by products of non renewable energy sources have contributed to adverse effects to human health affecting over 5 million lives annually [39].

As a consequence, there have been concerted global efforts towards reduction of CO_2 emission levels through implementation of green and low carbon emitting energy solutions [39]. Among the initiatives towards reducing reliance on fossil fuel based

technologies include the adoption of an energy mix resource strategy to enable inclusion of renewable energy into the energy matrix. Figure 2.1 illustrates the breakdown of the global renewable energy mix. Despite hydro-power energy being the leading renewable energy source, solar and wind energy have, recently, a rapid increase in the relative contribution.

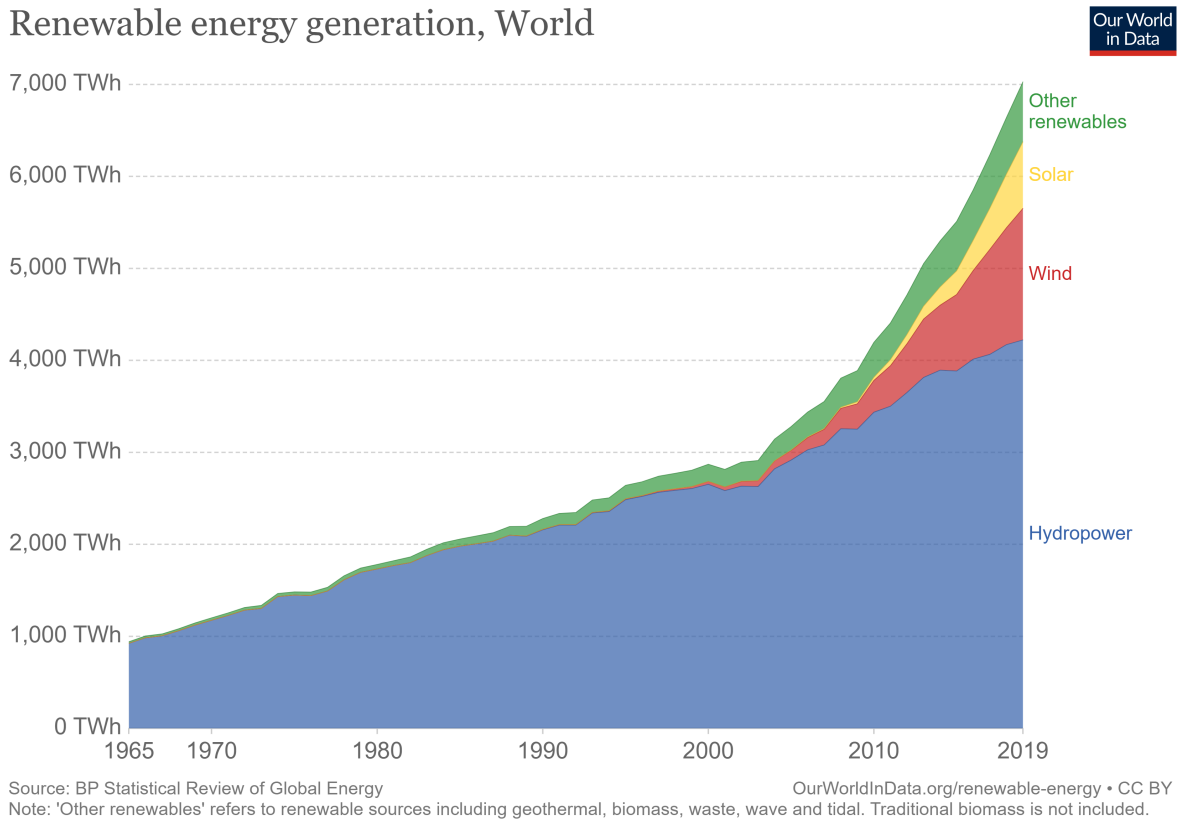


Figure 2.1: The breakdown of the renewable mix, and the relative contribution of each energy resource over a 50 year period [39].

Solar energy has recently gained a lot of attention in various research fields. In this section we shall expound on the families of solar cells that have been developed for harnessing the solar energy. Figure 2.2 illustrates the potential of solar energy as an available resource for *PV*. At every hour there's about 430 quadrillion Joules of energy from the sun that hits the earth. Of which, the total amount of energy that all humans use in a year is about 410 quadrillion Joules [39]. This creates a room for development and improvement to harness solar energy.

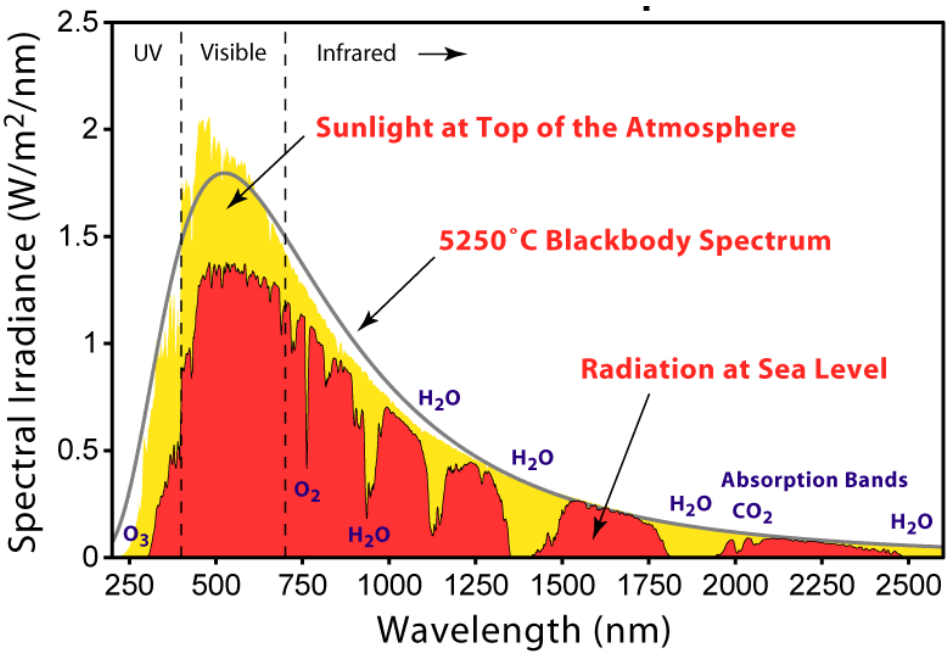


Figure 2.2: Solar cell spectrum (sourced from [40]).

Figure 2.3 illustrates the performance benchmarks of single and multiple junction solar cells that have been developed worldwide. It is evident that *GaAs* based solar cells have the highest efficiency but their high production costs preclude their implementation as *PV* modules on a large scale. Other low cost *PV* options include organic solar cells which are the current subject of intense research to enhance their photo-conversion efficiency of solar cell and submodules results involving high-efficiency under single/multiple-junction devices [41]. Figure 2.3 further shows that the *GaAs* solar cell has highest efficiency thus far and organic solar cells are still the least efficient, clearly showing that there is room for improvement.

Silicon based solar cells are one of the best candidates for large scale photovoltaic conversion of sunlight. However, the indirect bandgap of crystalline *Si* (*c-Si*) normally requires the use of doped layers (100 μm) to obtain sufficient absorption of the near infrared radiation. This increases costs and energy payback time. Hence, strategies for enhanced light absorption need to be explored to enable efficient light harvesting by thinner photoactive layers. One approach is to exploit the large optical cross-sections associated with local surface plasmon resonance *(LSPR)*, which can potentially lead to increased electron-hole pair generation in a nearby *Si* substrates via the strong evanes-

cent near fields close to the particles.

Classification	Efficiency (%)	Area (cm^2)	V_{oc} (V)	J_{sc} (mA/cm^2)	Fill Factor (%)	Test Centre (date)	Description
Silicon							
Si (crystalline cell)	**26.7 ± 0.5**	**79.0 (da)**	**0.738**	**42.65[a]**	**84.9**	**AIST (3/17)**	**Kaneka, n-type rear IBC[5]**
Si (multicrystalline cell)	**21.9 ± 0.4[b]**	**4.0003 (t)**	**0.6726**	**40.76[a]**	**79.7**	**FhG-ISE (2/17)**	**FhG-ISE, n-type[6]**
Si (thin transfer submodule)	21.2 ± 0.4	239.7 (ap)	0.687[c]	38.50[c,d]	80.3	NREL (4/14)	Solexel (35 μm thick)[7]
Si (thin film minimodule)	10.5 ± 0.3	94.0 (ap)	0.492[c]	29.7[c]	72.1	FhG-ISE (8/07)[e]	CSG Solar (<2 μm on glass)[8]
III-V cells							
GaAs (thin film cell)	28.8 ± 0.9	0.9927 (ap)	1.122	29.68[f]	86.5	NREL (5/12)	Alta Devices[9]
GaAs (multicrystalline)	18.4 ± 0.5	4.011 (t)	0.994	23.2	79.7	NREL (11/95)	RTI, Ge substrate[10]
InP (crystalline cell)	**24.2 ± 0.5[b]**	**1.008 (ap)**	**0.939**	**31.15[a]**	**82.6**	**NREL (9/12)**	**NREL[11]**
Thin film chalcogenide							
CIGS (cell)	**21.7 ± 0.5**	**1.044 (da)**	**0.718**	**40.70[a]**	**74.3**	**AIST (1/17)**	**Solar Frontier[12]**
CdTe (cell)	21.0 ± 0.4	1.0623 (ap)	0.8759	30.25[d]	79.4	Newport (8/14)	First Solar, on glass[13]
CZTS (cell)	**10.0 ± 0.2**	**1.113 (da)**	**0.7083**	**21.77[a]**	**65.1**	**NREL (3/17)**	**UNSW[14]**
Amorphous/microcrystalline							
Si (amorphous cell)	10.2 ± 0.3[g,b]	1.001 (da)	0.896	16.36[d]	69.8	AIST (7/14)	AIST[15]
Si (microcrystalline cell)	**11.9 ± 0.3[b]**	**1.044 (da)**	**0.550**	**28.72[a]**	**75.0**	**AIST (2/17)**	**AIST[16]**
Perovskite							
Perovskite (cell)	19.7 ± 0.6[g,h]	0.9917 (da)	1.104	24.67[i]	72.3	Newport (3/16)	KRICT/UNIST[17]
Perovskite (minimodule)	**16.0 ± 0.4[g,h]**	**16.29 (ap)**	**1.029[c]**	**19.51[c,a]**	**76.1**	**Newport (4/17)**	**Microquanta, 6 serial cells[18]**
Dye sensitised							
Dye (cell)	11.9 ± 0.4[j]	1.005 (da)	0.744	22.47[k]	71.2	AIST (9/12)	Sharp[19]
Dye (minimodule)	10.7 ± 0.4[j]	26.55 (da)	0.754[c]	20.19[c,l]	69.9	AIST (2/15)	Sharp, 7 serial cells[19]
Dye (submodule)	8.8 ± 0.3[j]	398.8 (da)	0.697[c]	18.42[c,m]	68.7	AIST (9/12)	Sharp, 26 serial cells[20]
Organic							
Organic (cell)	11.2 ± 0.3[n]	0.992 (da)	0.780	19.30[d]	74.2	AIST (10/15)	Toshiba[21]
Organic (minimodule)	9.7 ± 0.3[n]	26.14 (da)	0.806	16.47[c,l]	73.2	AIST (2/15)	Toshiba (8 series cells)[22]

(a) Single-junction solar cell

Classification	Efficiency (%)	Area (cm^2)	Voc (V)	Jsc (mA/cm^2)	Fill Factor (%)	Test Centre (date)	Description
III-V Multijunctions							
5 junction cell (bonded)	38.8 ± 1.2	1.021 (ap)	4.767	9.564	85.2	NREL (7/13)	Spectrolab, 2-terminal[23]
(2.17/1.68/1.40/1.06/0.73 eV)							
InGaP/GaAs/InGaAs	37.9 ± 1.2	1.047 (ap)	3.065	14.27[a]	86.7	AIST (2/13)	Sharp, 2 term.[24]
GaInP/GaAs(monolithic)	31.6 ± 1.5	0.999 (ap)	2.538	14.18[b]	87.7	NREL (1/16)	Alta Devices, 2 term.[25]
Multijunctions with c-Si							
GaInP/GaAs/Si (mech. stack)	**35.9 ± 0.5[c]**	**1.002 (da)**	**2.52/0.681**	**13.6/11.0**	**87.5/78.5**	**NREL (2/17)**	**NREL/CSEM/EPFL, 4-term.[26]**
GaInP/GaAs/Si (wafer bonded)	**31.3 ± 1.1[c]**	**3.981 (ap)**	**3.046**	**11.7[d]**	**87.5**	**FhG-ISE (3/17)**	**Fraunhofer ISE, 2-term.[27]**
GaInP/GaAs/Si (monolithic)	19.7 ± 0.7[c]	3.943 (ap)	2.323	10.0[e]	84.3	FhG-ISE (8/16)	Fraunhofer ISE[28]
GaAs/Si (mech. stack)	**32.8 ± 0.5[c]**	**1.003 (da)**	**1.09/0.683**	**28.9/11.1**	**85.0/79.2**	**NREL (12/16)**	**NREL/CSEM/EPFL, 4-term.[26]**
Perovskite/Si (monolithic)	23.6 ± 0.6[f]	0.990 (ap)	1.651	18.09[e]	79.0	NREL (8/16)	Stanford/ASU[29]
GaInP/GaInAs/Ge; Si(spectral split minimodule)	34.5 ± 2.0	27.83 (ap)	2.66/0.65	13.1/9.3	85.6/79.0	NREL (4/16)	UNSW/Azur/Trina, 4-term.[30]
a-Si/nc-Si Multijunctions							
a-Si/nc-Si/nc-Si (thin-film)	14.0 ± 0.4[g,c]	1.045 (da)	1.922	9.94[e]	73.4	AIST (5/16)	AIST[31]
a-Si/nc-Si (thin-film cell)	12.7 ± 0.4%[g,c]	1.000(da)	1.342	13.45[h]	70.2	AIST (10/14)	AIST[15,32]

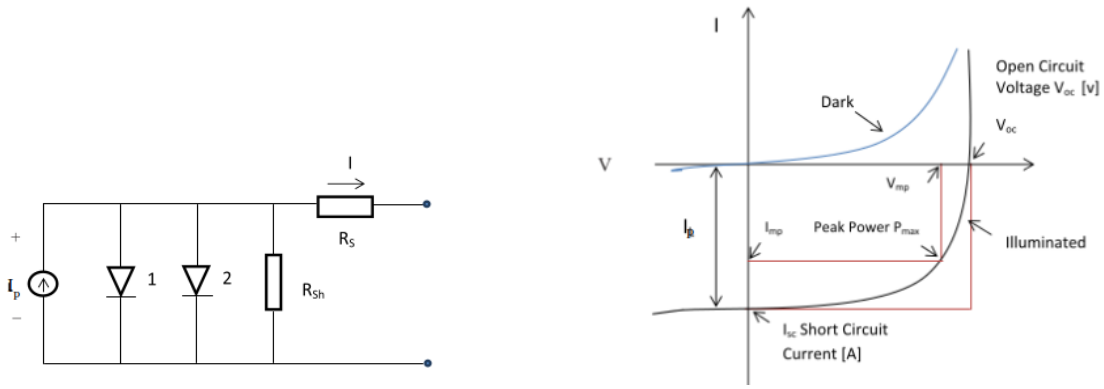
(b) Multiple-junction solar cell

Figure 2.3: Summary of the best-reported measurements for “one-sun" solar cells [41].

2.3 The Fundamentals of Solar Cells.

The production of electricity from the sun can be best understood by the mechanism of photovoltaic effect. This effect involves the absorption of light by the active layer to generate charge carriers within the material, from the sun can be considered as a stream of particles known as photons [42]. These photons contain different amounts of energy that correspond to the different wavelengths of the solar spectrum. When photons strike a *PV* cell, they may be reflected or absorbed, transmitted or scattered diffusely [43]. The energy of a photon is transferred to a bound electron in the valence band of the photoactive layer (e.g semiconductor) of the *PV* device [44]. The photo-absorption leads to the excitation of the valence electron into the conduction leaving behind a quasi particle (a hole) of opposite charge. This electron-hole (an exciton) pair can be either strongly or weakly interacting depending on the dielectric constant of the photoactive material. In the case of *Si*, a weakly bound exciton is produced and it can be separated into free charge carriers using the built in field in the device [45]. Consider the electron gas models which works perfectly fine for electrons and holes in a semiconductor. Special electrical properties of the *PV* cell, include a built in electric field, which provides the voltage needed to drive the current through an external load [46, 44].

The solar cell or *PV* device can be represented by an equivalent circuit comprising of a current source, two diodes in parallel to a resistor and a series resistor. This equivalent circuit is also known as the double diode model and it is useful in extracting the performance parameters of the solar cell [47, 48]. The double-diode model, simulates the space-charge recombination effect by incorporating a separate current component with its own exponential voltage dependence [49] (see Figure 2.4.a)). The double diode model is able to predict the photo and dark currents more precisely and can thus provide a more reliable representation of solar cell behavior than the single diode model [50]. Figure 2.4.a) illustrate the equivalent diode circuit for solar cell and Figure 2.4.b) show the *I–V* curve where characteristics of a solar cell can extracted.



(a) Equivalent diode circuit for solar cell.

(b) *I–V* characteristics of a solar cell.

Figure 2.4: Circuit structure and *I-V* characteristics of a solar cell in the dark and under illumination [51].

The current I flowing in the circuit is determined from Kirchoff's current laws as

$$I = I_D - I_P \tag{2.1}$$

where I_P is the photo-current and I_D is the dark current. The photo-current is described as

$$I_p = I_{sc}(1 + \frac{R_S}{R_{SH}}) - I_o(e^{\frac{I_{sc}R_S}{nTk/q}} - 1) \tag{2.2}$$

where I_{sc} is the short circuit current, R_S is the series resistance and R_{SH} is the shunt resistance. Where R_S accounts for the ohmic losses due to bulk resistance and the metallic contacts, while R_{SH} is associated with the leakage currents across the *p-n* junction. And n is the ideality factor, which is set unity, in case of an "ideal" diode. A full derivation of the expressions above can be found in [52].

The total current flowing is given by

$$I_T = I_o(e^{qv/nkT} - 1) - I_P \tag{2.3}$$

where I_o is the saturation current, which is related to leakage current under no illumination. V is the applied voltage across the diode terminals, q is the electron charge, k is the Boltzmann's constant and T is the absolute temperature (K).

From Figure 2.4.b), for short circuit current (I_{sc})is obtained when V=*0*. Thus ap-

plying equation 3.16 under these conditions yields:

$$I_{sc} = -I_P \tag{2.4}$$

For I_{sc} to have a high value, the front surface reflection, transmission losses, as well as less surface and bulk recombination losses, must be significantly low or minimal [50, 48].

When I=0, the open circuit voltage (V_{oc}) is given as

$$V_{oc} = \frac{nkT}{q} ln(I_P/I_o + 1) \tag{2.5}$$

In order to have a high value of V_{oc} there should be a low flow of I_o, and surface recombination velocities, with high doping densities and large diffusion length [53, 44, 48].

The Fill factor (FF) represents the overall quality of a solar cell. It is the ratio between the maximum power ($P_{max} = J_{mp}V_{mp}$) generated by a solar cell from the product of V_{oc} with J_{sc} (see Figure 2.4.b)),

$$FF = \frac{J_{max}V_{max}}{J_{sc}V_{oc}} \tag{2.6}$$

An ideal device should have a fill factor of 100%. This condition requires that the shunt resistance R_{sh} be infinite. However under normal conditions of most PV devices are far from ideal and thus their shunt resistance is usually several orders of magnitude larger that the series resistance (R_s). FF decreases with increasing size of the band gap, and with increasing size of the absorption layer (refer to Figure 2.5) [54].

The efficiency (η) of a solar cell is calculated as the ratio of generated electrical power (P_{max}) to the input light power (P_{in}).

$$\eta = \frac{P_{max}}{P_{in}} = \frac{J_{mp}V_{mp}}{P_{in}} = \frac{J_{sc}V_{oc}FF}{P_{in}} \tag{2.7}$$

The efficiency of a solar cell is an important metric which determines the amount of the incident solar energy that is converted to useful electrical energy e.g. a 1 m^2 solar panel with 15%, efficiency would convert a radiant energy of 1000 W/m^2 into

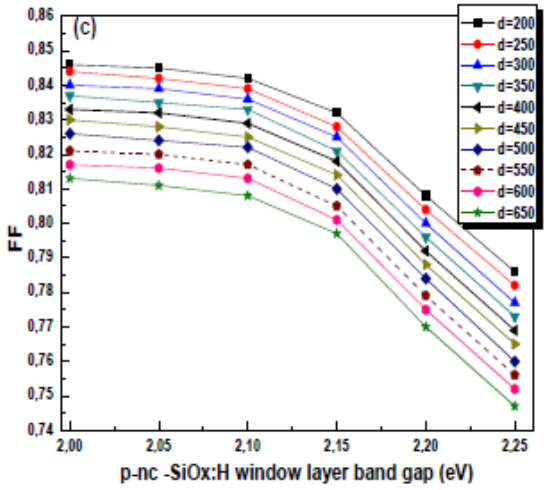


Figure 2.5: *FF* decrease with an increase of the band gap in the semiconductor and with an increase of the absorber layer thickness d [55].

150 W of electrical energy at AM 1.5 spectrum for a standard measurement [56]. The photoconversion efficiency of a solar cell device is limited by the following intrinsic factors such as [54, 56, 57]:

- Transmission losses due to non-absorption of long wavelengths,
- Thermalization of excess energy of photons,
- Total reflection losses at the front and back end,
- Incomplete absorption,
- Carrier recombination losses.

A more detailed discussion on these losses will be presented in the subsequent sections.

2.3.1 Shockley-Queisser Limit for *P-N* junction

Most of the solar cells contains junctions between (different) materials of different doping, these junctions are important in the operation of the solar cells. There are different types of junctions [58]:

- A *p-n* junction which is formed by two chemically different semiconductors,
- *p-i-n* junctions, where the region of the internal electric field is extended by inserting an intrinsic *(i)*, layer between the *p*-type and the *n*-type layers. The *i*-layer behaves like a capacitor and it stretches the electric field formed by the *p-n* junction across itself,
- Finally, the junction between a metal and a semiconductor known as the *MS* junction. The Schottky barrier is formed at the metal-semiconductor interface.

The Shockley–Queisser limit, also known as the Shockley Queisser Efficiency Limit or detailed balance limit or the radiative efficiency limit, is the maximum theoretical efficiency of a solar cell when using a single *p-n* junction to collect power from the cell where the only loss mechanism is radiative recombination in the solar cell [59]. This was first calculated by William Shockley and Hans-Joachim Queisser on the semiconductor in 1961, giving a maximum efficiency of 30% at 1.1 *eV* [60]. The maximum solar conversion efficiency limit is around 33.2% for a *p-n* junction photovoltaic cell under 1.5 AM solar spectrum and at a band gap of 1.34 *eV* [61]. Note that the solar cells with multiple junction are able to exceed this limit [62].

The Shockley-Queisser model in its original form illustrates three fundamental steps on the solar cell, noting the energy losses associated with each of these steps [63]. To understand that, we have a look at Figure 2.6 which shows the setting of the Shockley-Queisser model in its original form. It is presented as sub-figures of Figure 2.6:

a. Shown is a schematic of the Shockley-Queisser model, the sun at temperature, T_{sun} irradiating a solar cell at an ambient temperature T_{amb} (= T_{cell}) =300 K. The solar cell interacts with the surroundings by photons with the sun and its the ambient. The solar cell emits black-body radiation into the environment and delivers electrical power to the external circuit.
b. The three essential steps of photovoltaic power conversion, illustrated by an energy band diagram of a *p–n* junction solar cell; in which the *p (n)* semiconductor on the right (left). The conversion process consists of three steps [64]:

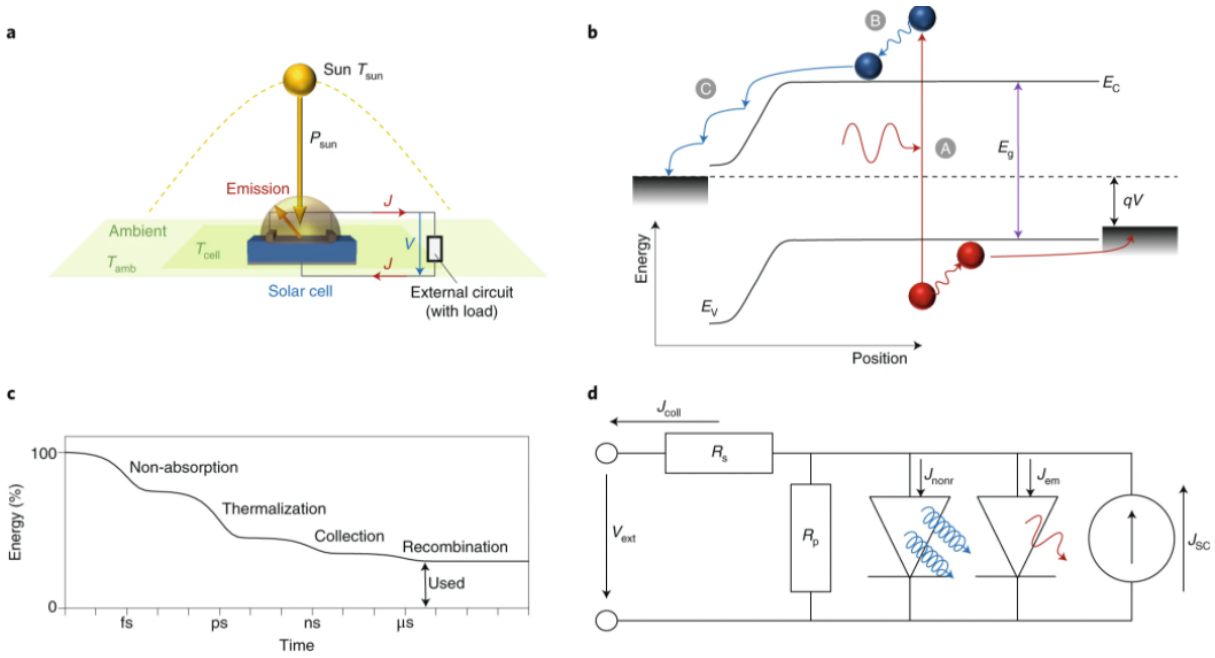


Figure 2.6: Schematic of the Shockley-Queisser model [59].

(a) Light absorption with ensuing local thermalization,

(b) Photogeneration and

(c) Charge collection with further thermalization within the semiconductor and contacts.

The flow of each of charge carrier (electrons in blue and holes in red) into a different contact is governed by the different chemical potentials of the *p* and *n* type semiconductor that make up the junction.

c. Typical timescales of these energy losses (note that in *Si* solar cells, charge transfer collection and recombination times could be much longer). Non-absorption losses refers to the photons that are transmitted through the layer due to their energies being lower than the bandgap (*Eg*) of the photoactive layer [65].

d. In terms of the simple equivalent (electrical engineering) circuit of a solar cell, the Shockley-Queisser model only requires a current source and a diode (the red photon represents radiative recombination with the current J_{em}). However, in non ideal conditions the solar cell equivalent circuit is appropriately described by the addition of a second diode which accounts for the non-radiative recombination, of current J_{nonr} (the wave representation in blue denotes heat dissipation), a parallel

or shunt resistance R_{sh} and a series resistance R_s [66].

The Shockley-Queisser limit is thus determined on the assumption that the fill factor of a solar cell assumes the value for an ideal diode. However this is an oversimplification as real *PV* devices have much lower *FF* values. The low value of Fill factor in most solar cells is attributed to:

1. The voltage drop due to the series resistance R_s of a solar cell, which is introduced by the resistance of the main current path through which the photo-generated carriers arrive to the external circuit [67],
2. Contributions to the series resistance by the bulk resistance of the junction, the contact resistance between the junction and electrodes, and the resistance of the electrodes themselves [54],
3. The voltage drop due to leakage currents, which is characterised by the shunt resistance R_{sh} of a solar cell. The leakage current is caused by the current through local defects in the junction or due to the shunts at the edges of solar cells [68],
4. The recombination of charge carriers in a non-ideal solar cell [69].

2.3.2 The External Quantum Efficiency

The external quantum efficiency (*EQE*) (λ_o) is the fraction of photons incident on the solar cell that create electron-hole pairs in the absorber, and are thus successfully collected [70]. It is wavelength dependent parameter measured from the ratio of the generated photocurrent (I_{ph}) to the incident monochromatic radiation (wavelength, λ_o) illuminated on a solar cell [71]. The external quantum efficiency is given by this expression

$$EQE(\lambda_o) = \frac{I_{ph}(\lambda_o)}{e\Phi_{ph}(\lambda_o)} \tag{2.8}$$

where e is the elementary charge and Φ_{ph} is the photon flux incident on the solar cell. Since I_{ph} is dependent on the fixed bias voltage, the bias voltage on the solar cell. The photon flux is usually determined by measuring the *EQE* of a calibrated photo-diode under the same light source.

2.3.3 Surface Recombination Effects

Generation and recombination processes that occur due to interband transitions are called direct generation rate and recombination. They usually occur in direct bandgap materials, as there is no change in momentum required for an electron that is excited into the conduction band. These processes are radiative, meaning that a photon is absorbed when an electron-hole pair is created, and a photon is emitted if electron-hole pairs recombine directly. The generation rate is dependent on the density of states, the band curvature, the carrier lifetime, etc. This section pertinent concepts for generation and recombination processes.

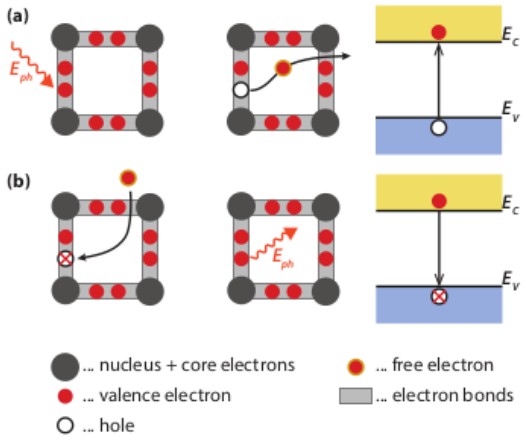


Figure 2.7: Visualisation of bandgap-to-bandgap (a) generation and (b) recombination processes using the bonding model and the energy band diagram [72].

Figure 2.7 illustrates the absorption of a photon by a bound electron in the upper most level of the valence band. The electron will transition to the top of the conduction band and undergo Coulombic interaction with the hole in the valence band. Absorption leads to the generation of an electron-hole pair. The condition for absorption are that the energy of the photon exceeds the band gap energy of the semiconductor or photoactive material [72].

The absorption profile of the material will therefore be dependent on the wavelength of the incident photon and the parameter that describes this property is also known as the absorption coefficient (α). The most frequent approach to calculate the absorption profile of photons in semiconductor devices is by using Lambert-Beer's law. In the present context it means that the photon flux density $\Phi(x,\lambda)$, decreases exponentially with the distance x traversed through the absorber

$$\Phi(x,\lambda) = \Phi_o(\lambda)e^{(-\alpha(\lambda)x)} \tag{2.9}$$

where Φ_o is the incident photon flux density at a certain wavelength λ density and $\alpha(\lambda)$ is the absorption coefficient. The photon flux density is defined as the number of photons per unit area, unit time and unit wavelength. It is related to the spectral power density $P(\lambda)$ associated with the solar radiation through

$$\Phi_o(\lambda) = P(\lambda)\frac{\lambda}{eh} \tag{2.10}$$

The spectral generation rate $g_{sp}(x,\lambda)$, which is the number of electron-hole pairs generated at a depth x in the film per second, per unit volume and unit wavelength, by photons of wavelength λ, is calculated according to

$$g_{sp}(x,\lambda) = \eta_g\Phi_o(\lambda)e^{(-\alpha(\lambda)x)} \tag{2.11}$$

where it is assumed that there's a zero reflection. η_g is the generation quantum efficiency, mostly assumed as an equal unity. From this assumption, it means that every photon generates one and only one electron-hole pair. The optical generation rate $G_L(x)$ is calculated from the spectral generation rate by integrating over a desired wavelength spectrum,

$$G_L(x) = \int_{\lambda_1}^{\lambda_2} g_{sp}(x,\lambda)d\lambda \tag{2.12}$$

It has the unit $[G_L] = cm^{-3}s^{-1}$. The optical generation rate is related to the absorption profile $A(x)$ in the film through

$$G_L(x) = \eta_g A(x) \tag{2.13}$$

hence

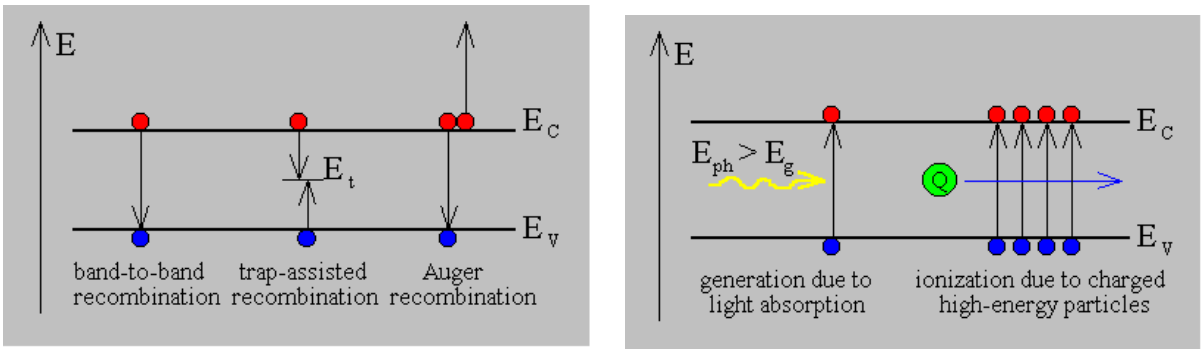
$$A(x) = \int_{\lambda_1}^{\lambda_2} \Phi_o(\lambda) exp[-\alpha(\lambda)x] d\lambda \tag{2.14}$$

Due to the photogeneration excess, electrons and holes are generated. The rates of the generated concentration of generated photo- electrons and holes per second are the same, therefore now have

$$\frac{\partial n}{\partial t}|_{light} = \frac{\partial p}{\partial t}|_{light} = G_L - U \tag{2.15}$$

where U is recombination rate.

The limiting efficiency of solar cells is one of the fundamental interest in PV research. As stated above it is determined by intrinsic recombination processes occurring within the semiconductor material, specifically radiative recombination and Auger recombination. Green [73] and Tiedje [74] et al. both proved that Auger recombination places a severe intrinsic bound under one-sun operation, giving a peak energy conversion efficiency of about 29.8% for a 100 μm cell with an isotropic response [74]. Figure 2.8 shows the possible recombination mechanisms in a semiconductor.



(a) (b)

Figure 2.8: Carrier recombination mechanisms in semiconductors [75].

Band-to-band recombination occurs when an electron tumbles from its state in the conduction band into the unfilled state in the valence band. This band-to-band transition

is usually accompanied by radiative emission especially in direct bandgap semiconductors [75, 76]. We thus define the band to band recombination rate (U) as:

$$U_{b-b} = b(np - n_i^2) \tag{2.16}$$

where b is the bimolecular recombination constant, n, p are the electron and hole density, respectively and n_i is the intrinsic carrier concentration

Trap-assisted recombination takes place when an electron falls into a "trap", inside the bandgap. The trap energy levels are associated with the presence of impurities or vacancies or dislocations within the host semiconductor material. When the trap is filled it cannot accept another electron. The electron possessing the trap energy can in a subsequent advance, fall into an empty/unoccupied state in the valence band [75]. This loop can be visualized as a two-way transition of an electron from the conduction band to the valence band, or as the destruction of the electron and the opening that meet in the trap. We will allude to this process as Shockley-Read-Hall (U_{SRH}) recombination rate and describe it analytically [77], in the form:

$$U_{SRH} = \frac{np - n_i^2}{p + n + 2n_i cosh(\frac{E_i - E_t}{kT})} N_i v_{it} \sigma \tag{2.17}$$

where v_{it} intrinsic trap recombination velocity, $E_{i(t)}$ is the intrinsic/trap energy, $N_{c(v)}$ are the effective densities of states for the conduction and valence band, k_b is the Boltzmann's constant and T is the temperature. σ is the trap capture cross section.

This expression can be simplified further for $p >> n$ to:

$$U_n = G_n - R_n = \frac{n_p - n_{p0}}{\tau_n} \tag{2.18}$$

and for $n >> p$ to

$$U_p = G_p - R_p = \frac{p_n - p_{n0}}{\tau_p} \tag{2.19}$$

where

$$\tau = \frac{1}{N_i v_{it} \sigma}$$

where $\tau_{n(p)}$ are lifetime parameters (for holes and electrons respectively). $R_{n(p)}$ is the radiative recombination rate for holes and electrons, respectively. $G_{n(p)}$ is the generation rate for holes and electrons, respectively.

Auger recombination is a band-to-band transition in which an electron and a hole recombine, but the emitted photon's energy is now re-absorbed by another electron or hole. Since the presence of a third particle influences the recombination rate, Auger recombination must be treated differently than band-to-band recombination [78]. Thus

$$U_{Auger} = \Gamma_n n(np - n_i^2) + \Gamma_p p(np - n_i^2) \tag{2.20}$$

where $\Gamma_{n(p)}$ is the total lifetime for electrons and holes, respectively.

2.4 Metallic *NPs* on the solar cell

Light trapping is a research area that has attracted extensive interest particularly in the enhancement of light absorption and thus photoconversion efficiency of solar cell devices [79]. Among the strategies that have been used to enhance light trapping include the use of metal nanoparticles or nanostructures that exhibit the surface plasmonic resonance in the near field regime [80]. A surface plasmon (*SP*) is the collective oscillation of the free electrons in a metallic nanoparticle can result in a strong enhancement of the electric field in its surrounding [81]. Surface plasmon resonance (*SPR*) is the resonant oscillation of conduction electrons at the interface among metal and dielectric permittivity material invigorated by incident light [82] (see Figure 2.9).

Metallic *NPs* scatter sun light more efficiently at resonance wavelength. The *NPs* scattering and absorption is mostly influenced by shape, size, material composition, host medium, and volume fraction of the *NPs* in the host medium [84]. Silver (Ag) and gold (Au) shows the most effective optical trapping from the material point of view, because of relative stronger scattering efficiency amongst other noble metals in the visible range [85].

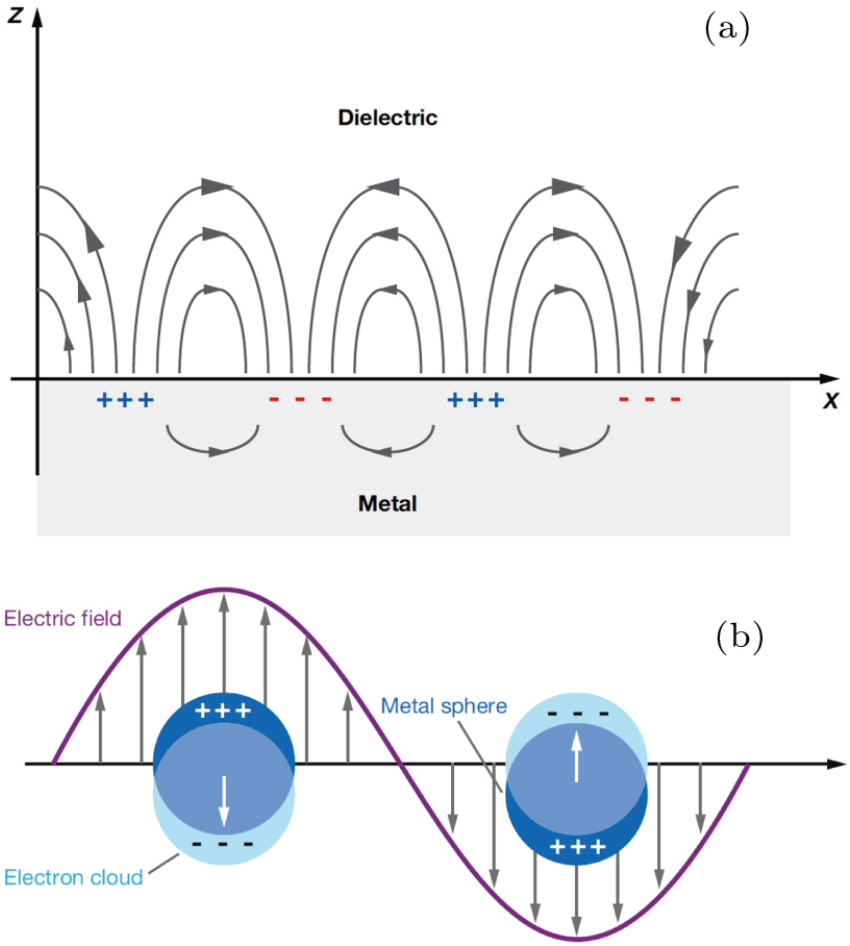


Figure 2.9: Incident light on a metallic *NPs* causes the conduction band electrons to oscillates and is known as the localized surface plasmon [83] .

Metallic *NPs* are oftenly incorporated at the top surface of a solar cell when designing a plasmonic enhanced solar cell as displayed in Figure 2.10. The interaction of light with the metallic *NPs* at the surface of the solar cell is mediated through forward scattering into the photoactive layer of the solar cell. In this geometry the path length of light is elongated within the absorbing layer and this leads to increased optical absorption in the device [86]. The optical absorption of semiconductors is promoted by the induced localized surface plasmon of metallic *NPs* from the concentrated near field intensity [87]. The plasmonic asymmetric modes in *NPs* have a the ability to improve the broadband optical absorption properties of the solar cells (for a full detailed explanation see [87]).

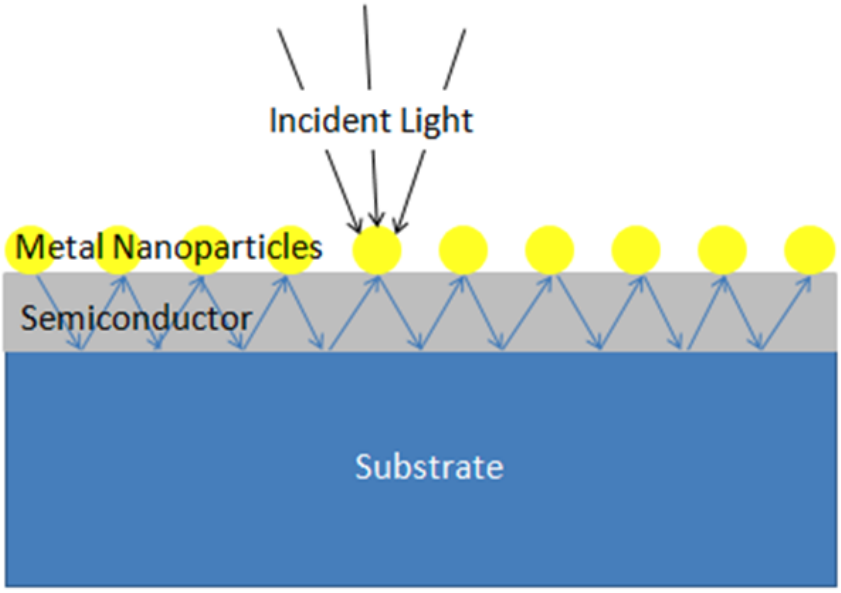


Figure 2.10: Basic solar cell structure with metallic *NPs* [44].

2.5 Core-Shell *NPs* in solar cells

However, the most used metallic nanospheres are *Au and Ag NPs* because of their tunable sizes and shapes, and they also have a narrow-band absorbance (having half-peak width of less than 100 *nm*) at 530 and 350 *nm*, respectively. Despite the promising results of *LSPR* in *PV* cells, the use of bare metal *NPs* is limited by their chemical stability, due to surface corrosion, agglomeration, and thermalization. These effects may lead to heat and recombination losses that affect the performance of the device [88, 89].

Additionally, the *NPs* can act as electron traps,thereby reducing the electron collection efficiency in the device. To mitigate these negative effects associated with instabilities of the bare metal *NPs*, a core shell consisting of a dielectric medium is added. In this work, SiO_2 and TiO_2 have been used as the shell layer to passivate the plasmonic core [89, 90]. The insulating shell protects the underlying particle from oxidative etching and also prevents unwanted electron accumulation [91, 92]. The effect of multiple shells and particle aggregation has also been explored [93]. The position of the *LSPR* band depends on the *NP's* size, shape, and dielectric environments (for multiple shells) [89]. Hence a need to fabricate highly efficient solar cell device that uses plasmonic resonance

to enhance the photoconversion efficiency, by taking the following considerations into account [94]:

- Incorporating broadband plasmonic *NPs* in solar cell devices to extend the spectral response of the photo-anode for maximizing light harvesting,
- Optimizing the geometric configuration of plasmonic *NPs* in solar cells to fully exploit both far-field scattering and near-field plasmonic effects for further light-harvesting management,
- Implementing an appropriate coating layer as a shell on the *NPs* surface for protection against corrosion and suppress electron recombination.

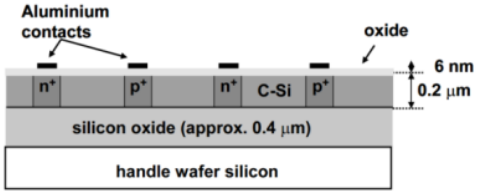
It is demonstrated in this work that the core-shell *NPs* (with metallic *NPs* dielectric) with enhanced forward scattering on *Si* based solar cell. The core-shell *NPs* support electric and plasmonic resonances [95].

2.6 Waveguides to guide light in a solar cell

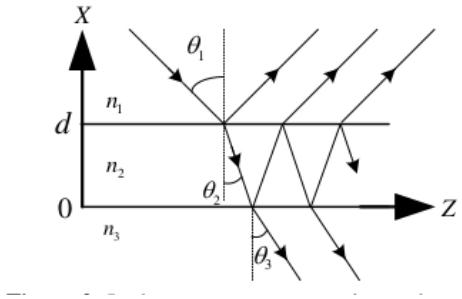
Enhancing photoelectric conversion efficiency of photovoltaic devices with a low efficiency can also be achieved by introducing waveguides on the device [96]. In the present work, waveguide structures comprising of silica will be implemented in the *PV* device as a strategy to enhancing the *PCE* of a commercial *a-Si* solar cell.

In this regard, a theoretical description of a planar solar cell incorporated with a waveguide layer is presented. An incident light beam propagating onto the SiO_2 layer (layer 1) undergoes multiple reflections in the *Si* layer (layer2) -SiO_2 interface to and is transmitted through the 3rd sandwiching SiO_2 layer. If the incident light enters in each layer i at an oblique angle (θ_i) and of refractive index (n_i), then applying Airy's summation for the reflectance and transmittance will yield an absorbance in the active layer of the form Figure 2.11a: take a planar solar cell coated or doped with a silicon waveguide layer, which is sandwiched between two layers of silicon dioxide (see Figure 2.11a). The incident light from layer 1 (silicon oxide) undergoes multi-reflection in layer

2 (silicon) and is finally transmitted into layer 3 (silicon oxide) [97]. Also from Figure 2.11b, we take the refractive indices and light propagation angles in each layer.



(a) ultra-thin crystalline silicon solar cell



(b) Light propagation near a layered structure

Figure 2.11: Basic structure for *c-Si* solar cell and refractive-index profile of the optical waveguide [51, 98].

The properties of a homogeneous dieletric film situated between two homogeneous media are shown in Figure 2.11b. From the Frasnel formulae for a transverse electric (*TE*) wave (see Born and Wolf for full detailed derivation [99]), the reflection (r_{ij}) and transmission (t_{ij}) coefficients are given as

$$r_{12} = \frac{n_1 cos\theta_1 - n_2 cos\theta_2}{n_1 cos\theta_1 + n_2 cos\theta_2} \tag{2.21}$$

$$t_{12} = \frac{2n_1 cos\theta_1}{n_1 cos\theta_1 + n_2 cos\theta_2} \tag{2.22}$$

the above equations can be further expressed as

$$r = \frac{r_{12} + r_{23} e^{2i\phi}}{1 + r_{12} r_{23} e^{2i\phi}} \tag{2.23}$$

$$t = \frac{t_{12} t_{23} e^{2i\phi}}{1 + r_{12} r_{23} e^{2i\phi}} \tag{2.24}$$

where t_{ij} and r_{ij} are the Fresnel transmission and reflection coefficients at the inter-

face of layer i and layer j, respectively,

$$\phi = k_{2x}d = n_2 k_o cos\theta_2 d \tag{2.25}$$

$k_o = \frac{2\pi}{\lambda_o}$ is the wave number in vacuum, and ϕ is the phase retardation for light traveling through layer 2 of thickness d.

Therefore, reflectivity (R) and transmissivity (T) are given by

$$R = |r|^2 = \frac{r_{12}^2 + r_{23}^2 + 2r_{12}r_{23}cos\phi}{1 + r_{12}^2 r_{23}^2 + 2r_{12}r_{23}cos\phi} \tag{2.26}$$

and

$$T = \frac{n_3 cos\theta_3}{n_1 cos\theta_1} \frac{t_{12}^2 t_{23}^2}{1 + r_{12}^2 r_{23}^2 + 2r_{12}r_{23}cos\phi} \tag{2.27}$$

Thus

$$R + T = 1 \tag{2.28}$$

The absorption A is given by application of the law of conservation of energy [100]

$$A = 1 - R - T \tag{2.29}$$

From Airy's summation [99, 101], the absorbance of the active silicon layer can be written as [102].

$$A = 1 - |\frac{r_{12} + r_{23}e^{2i\phi}}{1 + r_{23}e^{2i\phi}}|^2 - \frac{n_3 cos\theta_3}{n_1 cos\theta_1} |\frac{t_{12}t_{23}e^{2i\phi}}{1 + t_{12}t_{23}e^{2i\phi}}| \tag{2.30}$$

When the denominator of the second and third terms vanishes, the absorbance of equation 2.30 has singularities. These singularities are complex wave number plane poles whose positions are determined when

$$r_{12}r_{23}e^{2i\phi} = 1 \tag{2.31}$$

Now for the waveguide modes trapped by the total internal reflection (*TIR*) one must require that $\theta_2 > \theta_c$ and $|r_{21}| = |r_{23}|$ (see Figure 2.11b)

The dispersion relation of the waveguide modes can be written as follows [101].

$$2k_{2x} - 2\phi_{21} - 2\phi_{23} = 2m\pi \tag{2.32}$$

with m representing the mode index number

For light propagating in the the region $\theta_2 < \theta_c$ and $|r_{21}| = |r_{23}| < 1$, the singularities from absorbance transfer to a k_{2x} complex plane, where the poles correspond to waveguide modes on the real axis and escape cone modes on the complex plane.

The phase angles for the escape cone modes are close to zero i.e. $\phi_{21} = \phi_{23} \approx 0$, because the extinction coefficient of silicon is small compared to the actual part of the refractive index in the spectral range of interest.

$$2k_{2x} = 2m\pi \quad (m = 0, 1, 2, 3....) \tag{2.33}$$

Chapter 3

Numerical modelling of *PV* devices

3.1 Introduction

This chapter presents a discussion on the simulations of the absorption and scattering cross-sections of plasmonic spherical nanoparticles, core-shell nanostructures on a solar cell device. This treatment follow the detailed presentation on the physics of *Si* based solar cells.

3.2 Theoretical principles of plasmonic resonance in single and core-shell *NPs*

3.2.1 Theoretical point of view

In this section the mathematical formulations for absorption and scattering from a core-shell nanospheres/nanoparticles are presented. Figure 3.1 shows a spherical core-shell *NP* having a inner radius of the core a and outer radius of the shell b. We computed Mie efficiencies Q of a homogeneous spherical core-shell nanoparticles.

Mie theory was used to solve Maxwell's equations for spherical particles [104, 105]. The Mie theory can be used/implemented in MATLAB software to measure

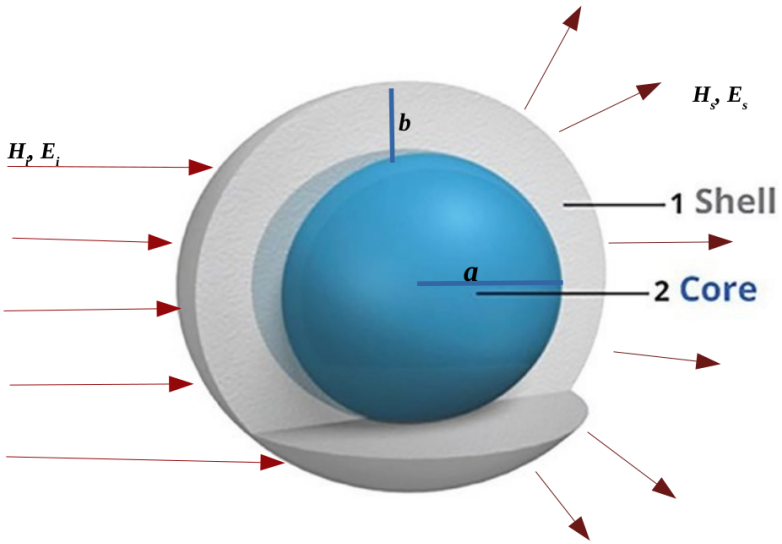


Figure 3.1: Scattering for non-interactive core-shell nano-sphere [103].

the optical efficiency parameters including extinction, absorption, and scattering for nanoparticles of various diameters and shell thicknesses [106]. The absorption Q_{abs}, scattering Q_{sca}, and extinction Q_{ext} efficiency for spherical *NPs* coexist under quasi-static conditions.

The optical efficiency parameters such as the absorption and scattering of spherical nanoparticles with varying dimensions can be calculated from Mie scattering by considering the primary scattering from the surface of the sphere and the secondary component caused by refraction within a particle. We thus compute the efficiency for radiation interaction by normalizing the scattering and absorption cross-sections with the particle cross-section in the form

$$Q_i = \frac{\sigma_i}{a^2\pi} \tag{3.1}$$

where Q_i efficiencies for the interaction of radiation with a scattering coated sphere of radius a, σ_i is the normalized cross-sections, and i it can be either extinction (i=*ext*), or absorption (i=*abs*), as well as scattering (i=*sca*).

The energy conservation law connects efficiencies as follows:

$$Q_{ext} = Q_{abs} + Q_{scat} \tag{3.2}$$

The scattering and extinction efficiency is given as [107].

$$Q_{ext} = \frac{2}{k^2}\sum_{n=1}^{n_{max}}(2n+1)Re\{a_n + b_n\} \tag{3.3}$$

$$Q_{scat} = \frac{2}{k^2}\sum_{n=1}^{n_{max}}(2n+1)(|a_n|^2 + |b_n|^2) \tag{3.4}$$

and

$$n_{max} = x + 4x^{1/3} + 2 \tag{3.5}$$

Mie coefficients a_n and b_n are the amplitudes of the scattered field given as [108]:

$$a_n = \frac{m^2 j_n(mx)[xj_n(x)]' - j_n(x)[mxj_n(mx)]'}{j_n(mx)[xh_n^{(1)}(x)]' - h_n^{(1)}(x)[mxj_n(mx)]'} \tag{3.6}$$

and

$$b_n = \frac{j_n(mx)[xj_n(x)]' - j_n(x)[mxj_n(mx)]'}{j_n(mx)[xh_n^{(1)}(x)]' - h_n^{(1)}(x)[mxj_n(mx)]'} \tag{3.7}$$

Here $m = m_2/m_1$, m_1 and m_2 are the refractive index of the coated sphere, inner and outer layers, respectively, relative to the ambient medium. All infinite series can be truncated after n_{max} terms (see Bohren and Huffman (1983) text book [109]), where $x = \frac{2\pi r}{\lambda}$ is the size parameter, $r = a + b$ is the total coated particle radius as a sum of inner radius and b outer thickness layer (as shown in Figure 3.1). $j_n(Z)$ and $h_n(Z) = j_n(Z) + iy_n(Z)$ are spherical Bessel functions of order n [110].

The quasi-static approximation simplifies the equations significantly and eliminates the need to measure spherical Bessel functions when simulating the absorption, extinction and scattering cross-sections for core-shell *NPs*. In the quasi-static approximation, the expressions for the electric field are obtained by allowing the wavelength to tend to infinity in relation to the particle size [111]. The extinction, scattering and absorption cross-sections are given as

$$\sigma_{ext} = \frac{2\pi\omega}{c} Im\{\alpha(\omega)\} \tag{3.8}$$

$$\sigma_{scat} = \frac{8\pi\omega^4}{3c^4}|\alpha(\omega)|^2 \tag{3.9}$$

and

$$\sigma_{abs} = \sigma_{ext} - \sigma_{scat} = \frac{2\pi\omega}{c} Im\{\alpha(\omega)\} - \frac{8\pi\omega^4}{3c^4}|\alpha(\omega)|^2 \tag{3.10}$$

where c is the speed of light, ω is the angular frequency and α is the complex polarizability of the particle given by

$$\alpha = 4\pi r_{shell}^2 \frac{(\varepsilon_{shell} - \varepsilon_m)(\varepsilon_{core} + 2\varepsilon_{shell}) - f(\varepsilon_{core} - \varepsilon_{shell})(\varepsilon_m + 2\varepsilon_{shell})}{(\varepsilon_{shell} + 2\varepsilon_m)(\varepsilon_{core}) + f(2\varepsilon_{shell} - 2\varepsilon_m)(\varepsilon_{core} - \varepsilon_{shell})} \tag{3.11}$$

where $\varepsilon_{core}, \varepsilon_{shell}$ and ε_m are the dielectric functions of the core, shell and surrounding medium, respectively. r_{core}, r_{shell} are the radius of core and shell respectively, and $f = (r_{core}/r_{shell})^{1/3}$ is the fraction of the total particle volume occupied by the core.

In this study, the simulations of the absorption/scattering cross-sections of *Ag/Au NPs, SiO_2, Ag/Au@SiO_2, TiO_2 and Ag/Au@TiO_2* core–shell *NPs* were computed, by varying the shell size and keeping the core size fixed and visa verse. The dependence of the complex dielectric function of metallic *NPs* on size are presented by replacing the bulk relaxation constant in the Lorentz-Drude dielectric function by a radius r dependent quantity as follows [112].

$$\varepsilon(\omega r) = \varepsilon_{bulk}(\omega) + \omega_p^2\left(\frac{1}{\omega^2\Gamma_\infty^2} + \frac{1}{\omega^2\Gamma(r)^2}\right) + i\frac{\omega_p^2}{\omega}\left(\frac{\Gamma(r)}{\omega^2 + \Gamma(r)^2} - \frac{\Gamma_\infty}{\omega^2 + \Gamma_\infty^2}\right) \tag{3.12}$$

where

$$\varepsilon_{bulk}(\omega) = 1 + \Sigma_{m=1}^{6} \frac{G_m\omega_p^2}{\omega_m^2 - \omega^2 - i\omega\Gamma_m} \tag{3.13}$$

$$\Gamma(r) = \Gamma_\infty + A\frac{v_F}{r} \tag{3.14}$$

and

$$\Gamma_\infty = \frac{v_F}{l_\infty} \tag{3.15}$$

ω is the angular frequency, ω_p is the plasmon frequency of metallic *NPs*, G_m is the strength of each resonance term, Γ_m is the damping factor or collision frequency, v_F is the Fermi velocity, l_∞ is the mean free path in bulk metal, A is a shape-dependent factor and can be taken as 1 for spherical particles. ω_m is the resonant frequency, and Table 3.1 shows the parameter values used in the calculations.

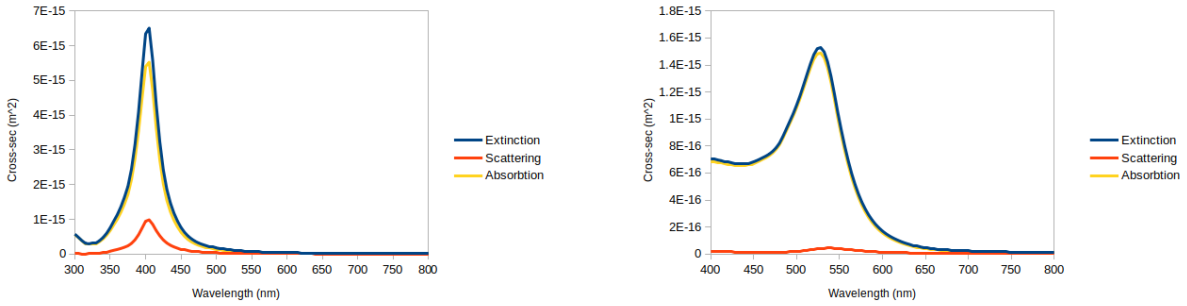
Table 3.1: Parameters used to calculate absorption and scattering cross-section of *Au/Ag NPs*, $Au/Ag@SiO_2$ and $Au/Ag@TiO_2$ core shells *NPs*

Constants used	**Value**
ω_p	Au= 8.6, Ag=9.01, eV
ω_m	[0.000 0.816 4.481 8.185 9.083 20.29] eV
Γ_m	[0.048 3.886 0.452 0.065 0.916 2.419] eV
ε_∞	Au= 6.88, Ag=3.71, SiO_2=3.6, TiO_2=18.9
G_m	[0.845 0.065 0.124 0.011 0.840 5.646]
v_F	$1.39 \times 10^6\ ms^{-1}$
l_∞	52 nm
$\hbar$	6.528×10^{-16} eV.s
e	$1.602 \times 10^{-19} C$
m	$9.011 \times 10^{-34} kg$
ε_o	$8.854 \times 10^{-12} m^{-3} s^{-2} A^{-2}$

3.2.2 Optical data modeling results.

For non-interacting spheres, Mie's theory explains the absorption and scattering of essentially spherical particles or core–shell. If one takes only the dipole approximation into account, the classical plasmon frequency is proportional to $(Ne^2/\varepsilon m\varepsilon_o)^{1/2}$, where N is the free electron density, e is the electronic charge, m is the electron mass, ε is the dielectric constant, and ε_o is the permitivity of free space [113, 114]. Optical proper-

ties of bulk media were used to calculate the absorption and scattering of the core-shell nanoparticles using the quasi-static approximation.



(a) 30 *nm Ag NPs*

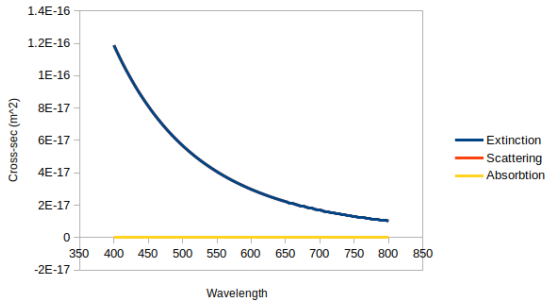
(b) 30 *nm Au NPs*

Figure 3.2: The absorption and scattering cross-section of 30 *nm* spherical *Ag And Au NPs*

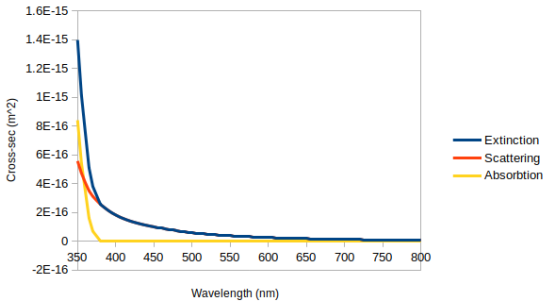
Figure 3.2 shows the absorption, scattering and extinction cross-sections of a 30 *nm* spherical *Ag and Au NPs*. The spherical 30 *nm Ag NP* in Figure 3.2a shows the plasmon resonance at 410 *nm* where absorption is dominating than scattering and is accompanied by sharp peaks. For the spherical 30 *nm Au NP* in Figure 3.2b, the plasmon resonance is observed at 540 *nm* with a high absorption of light and very low scattering of light accompanied by broader peaks. *Au NPs* absorbs light better than *Ag NPs*, whilst *Ag NPs* scatters light more than *Au NPs*.

Figure 3.3 shows the absorption, scattering and extinction cross-sections of a 50*nm* spherical SiO_2 and TiO_2 *NP*. Both SiO_2 and TiO_2 *NPs* scatters light rather than absorb light. Hence they are chosen as shells in our studies. Furthermore, the noble metallic *NPs* (*Au/Ag*) encapsulated by oxides (SiO_2/TiO_2) *NPs* are studied, where the size of the metal core *(Ag/Au NPs)* was fixed at 30 *nm*, while varying the size of the (TiO_2/SiO_2) shell thickness from *5,10,15,25,30,40 to 50 nm*.

On silica encapsulation, there are blue shifts observed as the shell thickness is increased from 5 *nm* up to 50 *nm*, Figure 3.4 shows the absorption and scattering cross-section of $Ag/Au@SiO_2$ core-shells *NPs* having different shell thickness with the same core size of 30 *nm*. A plasmon resonance is observed at around 410 *nm* up to 430 *nm*,

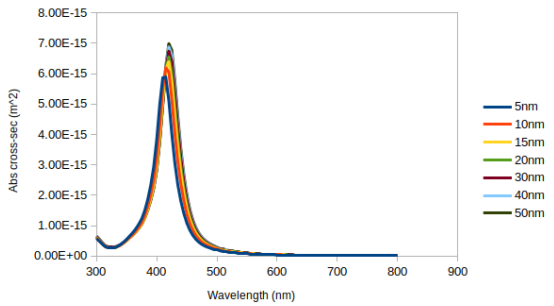


(a) 50 *nm* SiO_2 *NP*

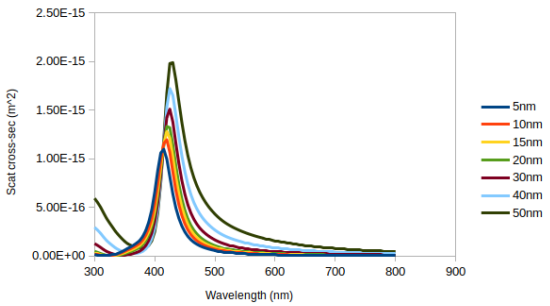


(b) 50 *nm* TiO_2 *NP*

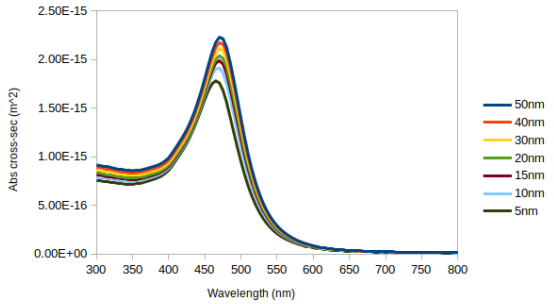
Figure 3.3: The absorption and scattering cross-section of 30 *nm* spherical *Ag and Au NPs*



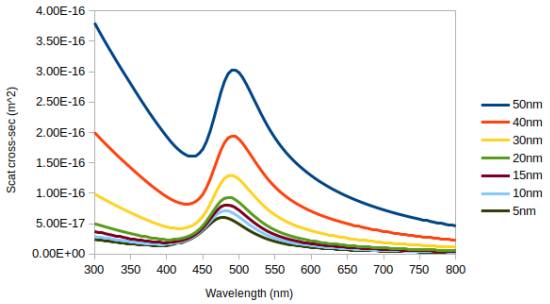
(a) $Ag@SiO_2$ core-shell *NPs* absorption cross-section



(b) $Ag@SiO_2$ core-shell *NPs* scattering cross-section



(c) $Au@SiO_2$ core-shell *NPs* absorption cross-section



(d) $Ag@SiO_2$ core-shell *NPs* scattering cross-section

Figure 3.4: The absorption and scattering cross-section of $Ag/Au@SiO_2$ core-shells *NPs* having different shell thickness with the same core size of 30 *nm*.

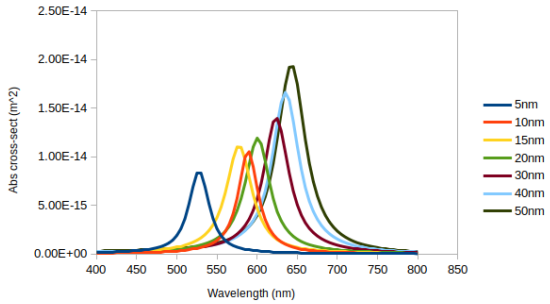
with an increase in the absorption intensity and exhibiting sharp peaks. The sharp peaks are accounting from the *Ag NP* (Figure 3.2a shows a sharp peak of *Ag NP*). Figure 3.4b shows their scattering cross-sections, the $Ag@SiO_2$ core-shell *NPs* absorbs light than scatters light when compared and a blue shift is also noted as shell-thickness increases.

The increase in absorption intensity is due to strong scattering field and the asymmetry of the peaks is due to the Fano resonance between the core and the dielectric shell. Where Fano resonances are seen in light scattering (see Figure 3.4c) from the spherical $Ag@SiO_2$ core-shell *NPs*, the damping factor of metals may be too great to see them clearly from absorption. The interference between a spectrally overlapping large resonance or continuum and a narrow discrete resonance are shown in Figure 3.4c, it is evident that there are Fano resonance [115].

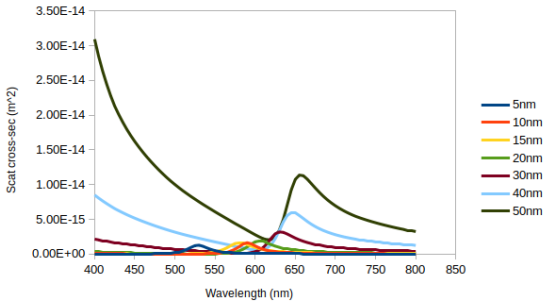
Then again the absorption and scattering cross-section of $Au@SiO_2$ core-shell *NPs* (see Figure 3.4c and Figure 3.4d, respectively) were studied. As the shell size increases, a red shift is observed with broad peak, the broad peaks are attributed to *Au NPs* (as seen in Figure 3.2b). Figure 4.17 illustrates that the absorption intensity increases with an increasing shell thickness and showing a plasmon resonance between 530 *nm* and 550 *nm* accompanied by red shift due to the increase in the electron density with increasing *NPs* diameter, also with an increase in the absorption strength. The electron mean free path determines the frequency of collision of the free electrons with the neighbouring surfaces, thus one would expect the imaginary component of the dielectric function to increase. Additionally, the surface scattering (see Figure 3.4d) does not change the position of the resonance but it increases the coupling with the resonance modes, electric field and this leads to broadening and increase in the intensity of the resonance [116].

Thus, the increase in the peak width is due to the confinement of the free electrons within the metal core (surface scattering). However, this is true only in the case of smaller particles, where the particle dimension is much smaller than the wavelength of electrons (below *25 nm*, for gold particles) [117].

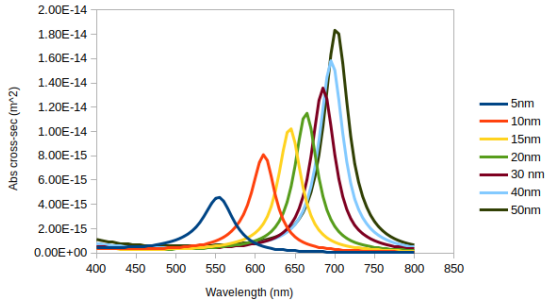
Regarding titania core-shell *NPs*, Figure 3.5 shows the absorption and scattering cross-section of $Ag/Au@TiO_2$ core-shells *NPs* having different shell thickness with the



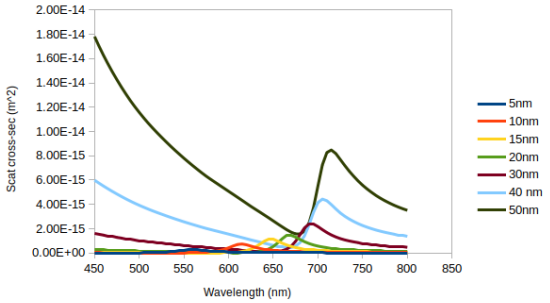
(a) $Ag@TiO_2$ core-shell *NPs* absorption cross-section



(b) $Ag@TiO_2$ core-shell *NPs* scattering cross-section



(c) $Au@TiO_2$ core-shell *NPs* absorption cross-section



(d) $Au@TiO_2$ core-shell *NPs* scattering cross-section

Figure 3.5: The absorption and scattering cross-section of $Ag/Au@TiO_2$ core-shells *NPs* having different shell thickness with the same core size of 30 *nm*.

same core size of 30 *nm*. Figure 3.5a shows the absorption cross-section of $Ag@TiO_2$ core-shell *NPs* where there's a huge red shift on plasmon resonance as the shell increase from 5 *nm* to 50 *nm*. The a huge plasmon resonance shifts is noted from the small thickness of 5 *nm* having a resonance peak at 520 *nm* to highest shell thickness of 50 *nm* with a plasmonic resonance of 650 *nm*. The huge red shift are attributed due to an effective medium where the dielectric properties of the shell dominates. Titania has a higher dielectric constant, where the lowest is 18.5 and it can go up to 90. It is also noted that as the titania shell thickness increases there is an increase in absorption strength. Figure 3.5b shows that the $Ag@TiO_2$ core-shell *NPs* has strong scattered fields, where the scattering cross-section is half the absorption cross-section for each core-shell *NPs*. Again the position of the scattering peak are in the same position with the absorption

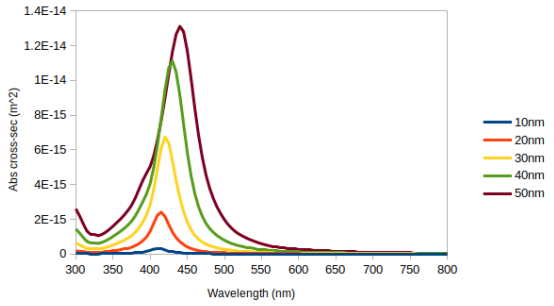
peak for each core-shell *NPs*.

The same trend seen in $Ag@TiO_2$ core-shell *NPs* is also observed in $Au@TiO_2$ core-shell *NPs* (seen Figure 3.5c), a 5 *nm* shell thickness gives as plasmon resonance at 550 *nm* which more likely positioned the same with the plasmon resonance of *Au NPs* and the big shell thickness (50 *nm*) gives a plasmon resonance at 730 *nm*, then again a huge skip red shift is also noted as the shell thickness increases. From these results, it is seen that the absorption cross-sections intensity increase with an increase of the shell thickness. The huge red shift may be attributed to an effective medium where the dielectric properties of the core being dominated by shell's dielectric properties [116]. The same trend that is observed in the scattering cross-section of $Au@TiO_2$ core-shell *NPs* (see Figure 3.5d), scattering intensity is half the absorption strength as the shell thickness increases.

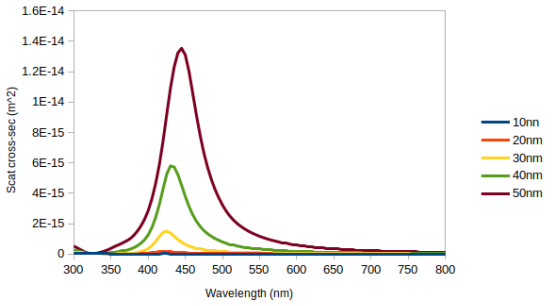
A further study on core-shell *NPs* was carried out, where the shell thickness was kept constant at 30 *nm* and the core sizes were varied (from 10, 20, 30, 40 to 50 *nm).*

Figure 3.6 shows the absorption and scattering cross-section of $Ag/Au@SiO_2$ core-shells *NPs* having different core sizes, with the same shell thickness of 30 *nm*. Figure 3.6a illustrates the absorption cross-section of $Ag@SiO_2$ core-shell *NPs* with varied core size from 10, 20, 30, 40, 50 *nm*. A plasmon resonance is observed at around 410 *nm* up to 450 *nm*, with an increase in the absorption intensity. The absorption intensity increase with an increase of the core size. A notable difference in increase in absorption strength and peak positions between increasing the shell thickness and core sizes. When comparing the two, it is evident that increasing the core size while keeping the shell thickness constant has a high impact on the absorption strength/intensity. In this case the peaks are no longer sharp, but rather fine as the size of the core increases. A blue shift is noted, as a result of the increase of the core sizes.

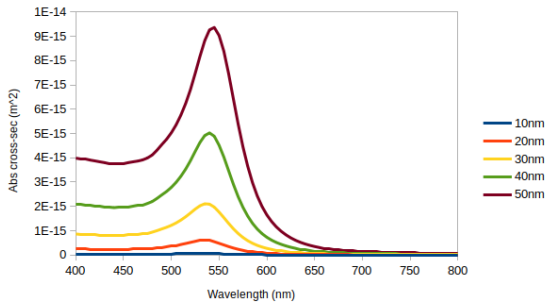
The increase in absorption intensity is it due to a strong scattering field (see Figure 3.6b) and the asymmetry of the peaks is this due to the Fano resonance between the core and the dielectric shell. Where in this case, Fano resonances are seen in light absorption of $Ag@SiO_2$ core-shell *NPs* (see Figure 3.6a). The scattering cross-section of $Ag@SiO_2$



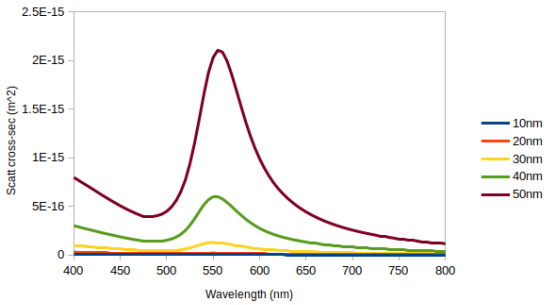
(a) $Ag@SiO_2$ core-shell *NPs* absorption cross-section



(b) $Ag@SiO_2$ core-shell *NPs* scattering cross-section



(c) $Au@SiO_2$ core-shell *NPs* absorption cross-section

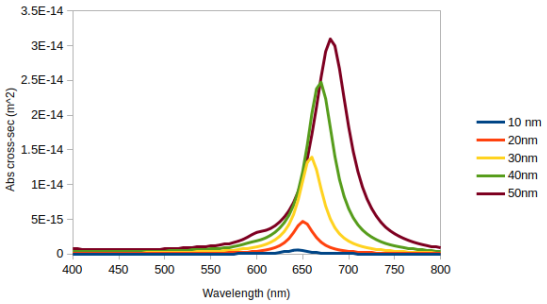


(d) $Au@SiO_2$ core-shell *NPs* scattering cross-section

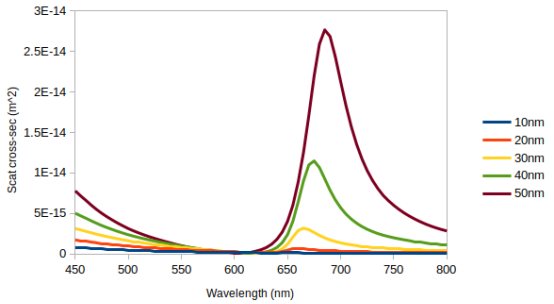
Figure 3.6: The absorption and scattering cross-section of $Ag/Au@SiO_2$ core-shells having different core sizes with the same shell thickness of 30 *nm*.

core-shell *NPs* is shown in Figure 3.6b, where the scattering strength is $3/4$ of the absorption strength as the shell thickness increases.

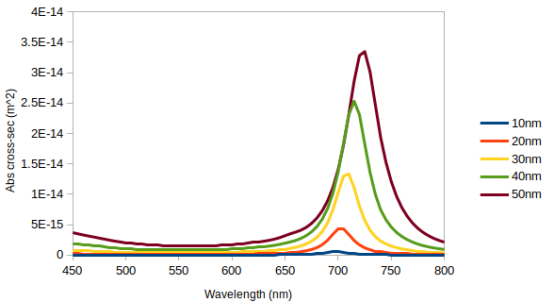
Then again the absorption and scattering cross-section of $Au@SiO_2$ core-shell *NPs* (see Figure 3.6c and Figure 3.6d, respectively) is also studied. As the core size increases, minimal peak/resonance shifts are observed but broader peak are seen. The broadening of peaks is attributed to the increase in size of the *Au NPs*. Figure 3.6c illustrates that the absorption intensity increases with an increasing core size and shows a plasmon resonance at 550 *nm*. The scattering cross-section of $Au@SiO_2$ core-shell *NPs* is shown in Figure 3.6d, where the scattering strength is $3/4$ the absorption strength as the shell thickness increases.



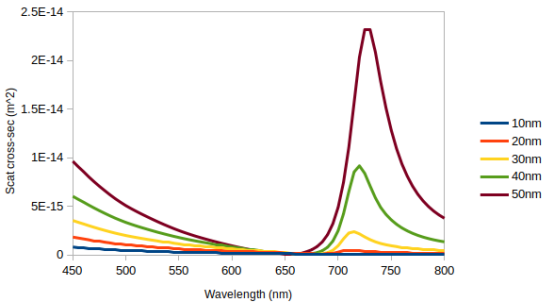
(a) $Ag@TiO_2$ core-shell *NPs* absorption cross-section



(b) $Ag@TiO_2$ core-shell *NPs* scattering cross-section



(c) $Au@TiO_2$ core-shell *NPs* absorption cross-section



(d) $Au@TiO_2$ core-shell *NPs* scattering cross-section

Figure 3.7: The absorption and scattering cross-section of $Ag/Au@TiO_2$ core-shell *NPs* having different core sizes with the same shell thickness of 30 *nm*.

Figure 3.7 shows the absorption and scattering cross-section of $Ag/Au@TiO_2$ core-shells *NPs* having different core sizes with the same shell thickness of 30 *nm*. Figure 3.7a shows the absorption cross-section of $Ag@TiO_2$ core-shell *NPs* where there's a slight red shift on plasmon resonance as the core sizes increases from 10 *nm* up to 50 *nm*. There is a red plasmon resonance shift from 650 *nm* to 660 *nm* and it is accompanied by high absorption strength. The red shift is attributed to an effective medium where the dielectric properties of the core dominates, regardless of the fact that titania has a higher dielectric constant. As the core gets bigger the dielectric of the core becomes dominant.

Figure 3.7b shows that the $Ag@TiO_2$ core-shell *NPs* have strong scattered intensity, where the scattering cross-section is $3/4$ the absorption cross-section for each core-shell *NPs* and the position of the scattering peak are in the same position with the absorption

peak for each core-shell *NPs*.

Furthermore, the absorption and scattering cross-section of $Au@TiO_2$ core-shell *NPs* are shown in Figure 3.7c and Figure 3.7d, respectively. As the core size increases, a slight red shift is observed. Figure 3.7c illustrates that the absorption intensity increases with an increasing core size and shows a plasmon resonance at 700 *nm* and it is accompanied by high absorption intensity. Varying the core sizes resulted in high absorption intensity than varying the shell thickness. These results suggest that the dielectric of the particles increases as the size of the particles increases. The scattering cross-section of $Au@TiO_2$ core-shell *NPs* is shown in Figure 3.6d, where the scattering intensity is almost the same as the absorption strength of the shell thickness increases.

3.3 The *J–V* characteristics simulations of the solar cells

Absorption profile depends on the intrinsic and extrinsic properties of materials. The intrinsic properties of materials include the absorption coefficient and it is dependent on the electronic band structure parameters such as the density of states and the oscillator strength specific to the material. On the other hand the extrinsic factors such as the geometry/thickness of the material are process properties that determine the profile of optical absorption. In this section a detail treatment of the current-voltage characteristics of a solar cell device will be presented.

3.3.1 *J–V* Simulation Methods

Device simulations are a crucial part of the development of more efficient types of solar cells because they allow us to test an idea or device before or reduce the potential cost and numerous time consuming steps in device characterization and optimization. The necessary simulation parameters are usually taken from experiment.

Consider Maxwell's equations [118],

$$\vec{\nabla} \times \vec{E} = \frac{\partial \vec{B}}{\partial t} \tag{3.16}$$

$$\vec{\nabla} \cdot \vec{B} = 0 \tag{3.17}$$

$$\vec{\nabla} \times \vec{H} = \vec{J} + \frac{\partial \vec{D}}{\partial t} \tag{3.18}$$

$$\vec{\nabla} \cdot \vec{D} = \rho \tag{3.19}$$

where $\vec{E}$ is the electric field, $\vec{H}$ the magnetic field, $\vec{D}$ the displacement vector, and $\vec{B}$ the magnetic flux density vector. $\vec{J}$ denotes the conduction current density, ρ is the electric charge density, and $\partial/\partial t$ is the partial derivative with respect to time

Equation 3.16 depicts the generation of an electric field due to a changing magnetic field (Faraday's law of induction), equation 3.17 predicts the absence of magnetic monopoles (magnetic sources or sinks), equation 3.27 depicts how an electric current and a change in the electric field produce a magnetic field (Ampere-Maxwell law), and equation 3.19 correlates the creation of an electric field due to the presence of electric charges (Gauss' law)

Poisson's equation correlates the electrostatic potential Φ to a given charge distribution ρ. It can be derived from equation 3.19 using the relation between the electric displacement vector and the electric field vector,

$$\vec{D} = \hat{\varepsilon} \cdot \vec{E} \tag{3.20}$$

where $\hat{\varepsilon}$ is the permittivity tensor. As $\vec{\nabla} \times \vec{E} = 0$ for the stationary case $\vec{E}$ can be expressed as a gradient field of a scalar potential field

$$\vec{E} = -\vec{\nabla}\Phi \tag{3.21}$$

Substituting 3.20 and 3.21 in 3.19 we get

$$\vec{\nabla} \cdot \hat{\varepsilon} \cdot \vec{\nabla}\Phi = -\rho \tag{3.22}$$

The permittivity is considered as a scalar, which is constant in homogeneous materials. The Poisson's equation is obtained as

$$\vec{\nabla} \cdot \vec{\nabla}\Phi = -\frac{\rho}{\varepsilon} \tag{3.23}$$

The space charge density ρ

$$\rho = q(p - n + C) \tag{3.24}$$

where q is the elementary charge, p and n are the hole and electron concentrations, respectively, and C is the concentration of additional, typically fixed, charges. These fixed charges can originate from charged impurities of donor (N_{D}) and acceptor (N_{A}) type and from trapped holes (ρ_p) and electrons (ρ_n),

$$C = N_D - N_A + \rho_p - \rho_n \tag{3.25}$$

From equation 3.23 and 3.24 the Poisson's equation for semiconductor device simulation is given as

$$\vec{\nabla} \cdot \vec{\nabla}\Phi = \frac{\rho}{\varepsilon}(N_D - N_A + \rho_p - \rho_n) \tag{3.26}$$

Applying the divergence operator $\vec{\nabla}\cdot$, to the continuity equations (equation 3.27), and considering that the divergence of the curl of any vector field equals zero

$$\vec{\nabla} \cdot \vec{\nabla} \times \vec{H} = \vec{\nabla} \cdot \vec{J} + \vec{\nabla} \cdot \frac{\partial \vec{D}}{\partial t} = 0 \tag{3.27}$$

The total current density $\vec{J}$ into hole and electron current densities, $\vec{J} = \vec{J}_p + \vec{J}_n$ are given as

$$\vec{J}_n = q\mu_n n \vec{\nabla}\vec{E} + qD_n n \vec{\nabla} n \tag{3.28}$$

$$\vec{J}_p = q\mu_p p \vec{\nabla}\vec{E} + qD_n n \vec{\nabla} p \tag{3.29}$$

where $J_{n(p)}$ is the charge current density of electrons (holes). $\mu_{n(p)}$ is the electron/hole mobility, and D is electron diffusion coefficient. The first term in each equation is for drift and the second term is for diffusion.

The simulations are obtained with python, with the help of *sesame, numpy and scipy* libraries (see [119] for documentation on how the libraries work) for the *PVs* devices.

Sesame describes the steady state behavior of a system, that is governed by drift-diffusion equations and the Poisson equations introduce the equations below [120, 119] :

$$\vec{\nabla} \cdot \vec{J}_n = -q(G-R) \tag{3.30}$$

$$\vec{\nabla} \cdot \vec{J}_p = (G-R) \tag{3.31}$$

The Poisson equation is given as

$$\vec{\nabla} \cdot (\varepsilon \vec{\nabla} \Phi) = -\rho/\varepsilon \tag{3.32}$$

Where $G_{n(p)}$ is the electron/hole pair generation rate density and R is the recombination rate density.

The short-circuit current density J_{sc} is calculated for different values of the absorption coefficient. The python program is implemented using the variables in table 3.2 [119, 120].

In calculating the current density J in solar cells, the most critical parameter are the diffusion length, surface passivisation and absorption coefficient. For a solar cell with perfectly passivated surface and uniform generation, the equation for the short-circuit current can be approximated as [119]:

$$J_{(sc)} = q\phi(1 - \frac{e^{-\alpha d}}{1+\alpha L}) \tag{3.33}$$

where α is the absorption coefficient, d is the width of the depletion layer and L is the electron diffusion length given by

$$L = \sqrt{D\tau} \tag{3.34}$$

τ is the lifetime parameter (for holes and electrons) and D is the electron diffusion

coefficient in cm^2/s^{-1} given by

$$D = kT\mu/q, \tag{3.35}$$

where μ is the mobility of the charge carriers, k is the Boltzmann constant in $m^2kgs^{-2}k^{-1}$, q is the electron charge and T is the temperature.

Note that diffusion length and the electron diffusion coefficient are calculated on the code (see documentation [119])

Introducing photonic crystals or core-shell *NPs* such as SiO_2, TiO_2, $Ag@SiO_2$ *and* $Ag@TiO_2$ on the *c-Si* solar cell, is expected to enhance the photon absorption of the *PV* device. Adding these materials would give a different absorption coefficient according the type of material (this method is explained well in [121]). Here are the absorption coefficient for the reference solar cell and the ones embedded with *Ag NPs,* SiO_2*NPs,* TiO_2 *NPs,* $Ag@SiO_2$ *core-shell NPs and* $Ag@TiO_2$ *core-shell NPs* are as follows 2.32×10^4, 3.685×10^5, 2.681×10^5, 6.909×10^4, 3.316×10^5 5.759×10^5 (cm^{-1}) , respectively and were taken from [122, 121]

We studied *c-Si:H PVs* just as proof of concept that as we introduce core-shell *NPs* that there would be an improvement on optical absorption and *PCE*.

3.3.2 *J–V* Simulation Results

Figure 3.8 shows the *J-V* characteristic of a *p-n* junction, the *c-Si* solar cell coated with different layers containing particles (such as *Ag NPs,* SiO_2 *NPs,* TiO_2 *NPs,* $Ag@SiO_2$ core-shell *NPs* and $Ag@TiO_2$ core-shell *NPs* each having a diameter of *50 nm* and it is assumed that they are uniformly distributed on the solar cell.

Figure 3.8 shows an increase in current density upon incorporation of *Ag NPs*, $Ag@SiO_2/TiO_2$ core-shell *NPs* and SiO_2/TiO_2 nanospheres on the surface the solar cell and are homogeneously distributed. The reference *c-Si* solar device has the lowest short circuit current density (J_{sc}). The open circuit voltage (V_{OC}) is nearly constant for

Table 3.2: The parameters used in simulating the *J-V* characteristics for a single crystalline silicon solar cell

Symbol	Description	Standard values
ϕ	photon flux $cm^{-2}s^{-1}$.	3×10^{17}
n_A	Acceptor concentration cm^{-3}.	1×10^{15}
n_D	Donor concentration cm^{-3}.	1×10^{17}
N_v	Densities of states of the valence bands cm^{-3}.	4×10^{20}
N_c	Densities of states of the conduction band cm^{-3}.	4×10^{20}
μ_e	electron mobility cm^2/Vs	5×10^5
μ_h	hole mobility cm^2/Vs	4.5×10^5
α	Light absorption coefficient cm^{-1}	2.32×10^4
q	Charge of electrons C.	1.60218×10^{-19}
τ_h	Lifetime of holes in the valence band in s.	604×10^{-6}
τ_e	Lifetime of electrons in the conduction band in s.	604×10^{-6}
T	Temperature in K.	300 K
k	Boltzmann constant in $m^2kgs^{-2}k^{-1}$.	$1.38064852 \times 10^{-23}$
d	Thickness of thin film (m)	250×10^{-6}
V	Photovoltage in V.	0 – 0.95
ε	Material's dielectric constant	11.7
E_g	Energy band gap of the material (eV)	1.21

all devices, suggesting that the incorporation of the nanostructures does not significantly affect the band alignment in the active layer.

The absorption and scattering cross-section simulations of the core-shell *NPs* revealed that the absorption dominates scattering of light, on the plasmonic resonance. This suggest that *LSPR* of *Ag NPs* may produce more photo-generated charge carriers due to higher active layer absorption, resulting in a larger electromagnetic field enhancement near the metallic *NPs* [123].

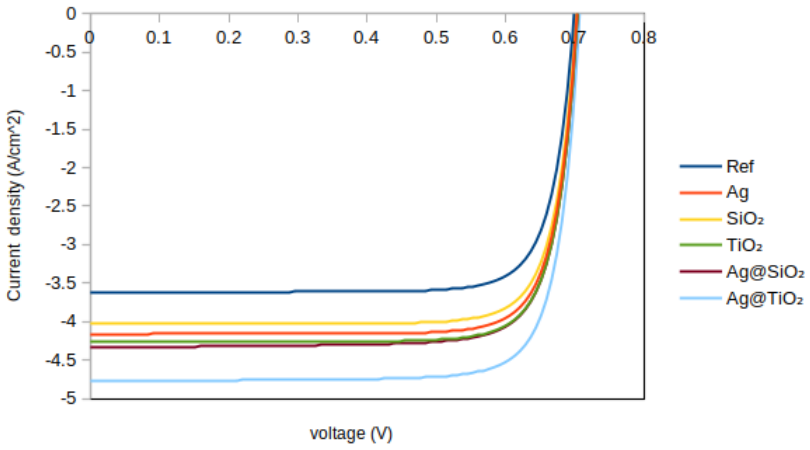


Figure 3.8: *J-V* curve of *c-Si* solar cell incorporated with *Ag NPs, SiO_2 NPs, TiO_2 NPs, $Ag@SiO_2$* core-shell *NPs* and *$Ag@TiO_2$* core-shell *NPs*.

Table 3.3 shows that the current density (J_{sc}), fill factor (*FF*), open circuit voltage (v_{oc}) and photo-conversion efficiency (*PCE*) of the simulated *c-Si* solar cells with and without metallic *NPs* an core-shell *NPs*. Incorporating the *c-Si* solar with *Ag NPs, SiO_2 NPs, TiO_2 NPs, $Ag@SiO_2$* core-shell *NPs* and *$Ag@TiO_2$* core-shell *NPs* has improved the *PCE* significantly due to the plasmon resonance originating from *Ag NPs*. The advantage of using silica or titania as shells will reduce thermalization and agglomeration of *Ag NPs* at the surface or in the vicinity of the device and ensures that the *Ag NPs* take full advantage of *LSPR* and light absorption/scattering.

Accordingly, the *PV* performance of the solar cell with *Ag NPs* and a SiO_2 nanospheres improved substantially as shown in the *J-V* curve in Figure 3.8.

In the summary of table 3.3, the reference *c-Si* solar cell has a J_{sc} of 3.61 A/cm^2 which is the lowest of them all. The V_{OC} for all samples remains the same at 0.70V except for the reference device is at 0.68V. There's a notable increase in J_{sc}, *FF* and *PCE* upon incorporation of metallic *NPs* and core-shell *NPs*. The current density improved from 3.61 A/cm^2 with the reference *c-Si* solar cell up to 4.77 A/cm^2 with a device incorporated with *$Ag@TiO_2$* core-shell *NPs*. The result demonstrates that the incorporation of different core-shell *NPs* brings an improvement in fill factor which improved from 0.78 up to 0.87, resulting from a device incorporated with *$Ag@TiO_2$* core-shell *NPs* due

to far field effects. The *PCE* improved very well, and this accounts from the enhanced light absorption coming from the *LSPR* due to the *Ag NPs* in the device, which also contributes to the improvement of electron transport. The results or rather the calculations shows that the *c-Si* solar cell incorporated with $Ag@TiO_2$ core-shell *NPs* has the most improved *PCE* of 28.05%.

We also observed that current density (J_{sc}) *c-Si* solar cell with $Ag@TiO_2$ core-shell *NPs* having highest (J_{sc}) of 4.77 A/cm^2 and the lowest of 4.03 A/cm^2 was recorded from the device with SiO_2 *NPs*. The results shows that the surrounding dielectric medium and interactions with the conduction electrons of the metal core lead to polarization that affect the resonance of the localized plasmonic modes which then leads to good improvement in the *PCE* [124]. These findings show that due to increased active layer absorption, *LSPR* of *Ag NPs* may have produced more photo-generated charge carriers, resulting in a bigger electromagnetic field enhancement near the metallic *NPs* [123].

The reference *c-Si* solar cells exhibited a *PCE* of 21%, but after incorporating with core-shell *NPs* there was an increase in *PCE* to 28.05% with $Ag@TiO_2$ core–shell on the device.

The increase in *PCE* and J_{sc} is also attributed to the increased photon flux, the enhanced electromagnetic field of *Ag NPs*, and the enhanced visible-light absorption owing to the large-size *Ag NPs*. Consolidation of plasmonic core-shell *NPs* has improved the light collecting ability of the photoanode and subsequently essentially improved the exhibition [125, 126].

Devices incorporated with core-shell *NPs* and *Ag NPs* had closely related V_{oc} values, which are higher from the reference. The incorporation of noble mental leads to the down-shifted quasi-Fermi level, while V_{oc} is proportional to the difference between the quasi-Fermi level [127].

With $Ag@SiO_2$ core–shell *NPs*, *PCE* improved to 26.43%, while the *PCE* of the simulated *c-Si* solar cells with *Ag NPs* improved to 24.46%. But the *PCE* of device with SiO_2 increased to 22% from 21% of the reference device, which gave the lowest improvement in *PCE* and the one with TiO_2 *NPs* improved to 26.24%. Clearly the

increase in *PCE* on the devices is attributed to the preferential light scattering into the device by the *LSPR* effect of the *Ag NPs*.

Table 3.3: The summary of *J-V* characteristics for a single crystalline silicon solar cell

c-Si solar cell	V_{OC} (v)	J_{SC} (**A**/cm^2)	**FF %**	**PCE**
Ref	0.68	3.61	0.83	21.00
c-Si:Ag *NPs*	0.70	4.16	0.84	24.46
c-Si:SiO_2	0.70	4.03	0.78	22.00
c-Si:TiO_2	0.70	4.26	0.88	26.24
c-Si:Ag@SiO_2	0.70	4.37	0.87	26.43
c-Si:Ag@TiO_2	0.70	4.77	0.84	28.05

3.4 Conclusion

In this chapter, the utilization of complete use of *LSPR* for the enhancement of solar cell is described and achieved. Having non-interacting spheres, the quasi-static approximation was used to elaborate the absorption and scattering of spherical nanoparticles or core–shell nanoparticles. The absorption and scattering cross-section of *Ag* and *Au NPs* was studied in under 2 distinct dielectric. The simulations have shown strong dependence of plasmon resonance with varying *NPs* sizes. The $Ag@SiO_2$ core-shell *NPs* absorption cross-sections showed an increase in the magnitude of the absorption as the shell size/thickness was increased (the core size was kept the same through out) and a blue shift in the plasmon resonance is observed. From this study, it was also observed that the 50 *nm* $Ag@SiO_2$ core-shell *NPs* had higher absorption resonance at 450 *nm*. On the other hand the simulation of $Ag@TiO_2$ core–shell *NPs* revealed a huge red shift in plasmon resonance as the shell thickness of titania increased. The red shift was observed from 530 *nm* up to 680 *nm*, which indicates that titania dielectric medium is better than silica in absorbing photons and it was also observed that 50 *nm* $Ag@TiO_2$ core-shell

NPs and had a good absorption efficiency (see Figure 3.5). The same effect was observed for $Au@SiO_2$ and $Au@TiO_2$ core-shell *NPs*. Furthermore, the size of the core were varied (from 10, 20, 30, 40 and 50*nm*) and the shell thickness was kept at 30 *nm*, the pick shift were minimal for both $Ag/Au@SiO_2$ and $Ag/Au@TiO_2$ core-shell *NPs* or rather maintained the position of the shell thickness. The absorption and scattering intensity for both core-shell *NPs* were nearly the same.

The *J-V* calculation were performed, for a crystalline silicon (*c-Si*) solar cell with and without 50 *nm* core-shell *NPs* incorporated. The simulation showed an increase on current density as the core-shell *NPs* are introduced on the device (Figure 3.8). From table 3.3, the reference *c-Si* solar cell had a J_{sc} of 3.61 A/cm^2 and was increased/improved to 4.37 A/cm^2 with $Ag@SiO_2$ core-shell *NPs*, which further went up to 4.77 A/cm^2 with $Ag@TiO_2$ core-shell *NPs* and this provide the largest *PCE* of 28.05%. The V_{OC} for all devices remains the same at 0.70 V. There is an improvement in *PCE* and in J_{sc} for a *c-Si* solar cell with $Ag@TiO_2$ core-shell *NPs*, the reference cell had *PCE* of 21% and J_{sc} of 3.61 A/cm^2. With $Ag@SiO_2$ core-shell *NPs* there was *PCE* improvement of 25.86%. From the *J-V* simulation of $Ag@TiO_2$ core-shell *NPs*, can be conclude that titania is a better shell than silica in reducing thermalization and also has greater impact in enhancing the efficiency of solar cell by promoting scattering and absorption of light at the same time.

Chapter 4

PV devices incorporated with metallic and core-shell *NPs*

In this Chapter, fabrication of metallic *NPs* together with silica *NPs* is together with the fabrication of core-shell *NPs* embedded with metallic *NPs* as cores is presented. An optical study was then carried out by measuring the absorption and transmittance spectra. The metallic *NPs* and core-shell *NPs* were later incorporated in a commercial *a-Si* solar cell to illustrate performance enhancement effects. All the results obtained from the various experiments performed are presented in separate sub-sections.

4.1 Introduction

The sol-gel process is a wet chemical technique predominantly used in material research applications. This method is regarded as the most suitable approach for metal oxide nanoparticles synthesis and it involves a combination of two steps, a) hydrolysis and b) polycondensation of suitable molecular precursors (usually metal- alkoxides or -chlorides), which leads to the gradual formation of a solid-phase network.

In the preparation of silica (SiO_2) nanoparticles, the Stöber method was used, which is a controlled chemical process [128] that produces a uniform size nanoparticles [129] for applications in materials science. The pioneering work was done by Werner Stöber [130] and his team in 1968, and to this day it remains the most widely used wet chemistry synthetic approach to produce silica nanoparticles [130]. During a sol-gel process,

a molecular precursor (such as tetraethylorthosilicate) reacts with water in an alcohol and the resulting molecules links u together to larger structures (see Figure 4.1). The reaction produces silica nanoparticles with diameters ranging from 20 to 2000 *nm*, depending on the experimental conditions such as reaction time, temperature and concentration of the materials in use for the synthesis [131]. The process has been extensively researched since it was first discovered, including efforts to understand its kinetics and polymerization mechanisms. A particle aggregation model was found to be suitable in explaining the experimental data [131, 132].

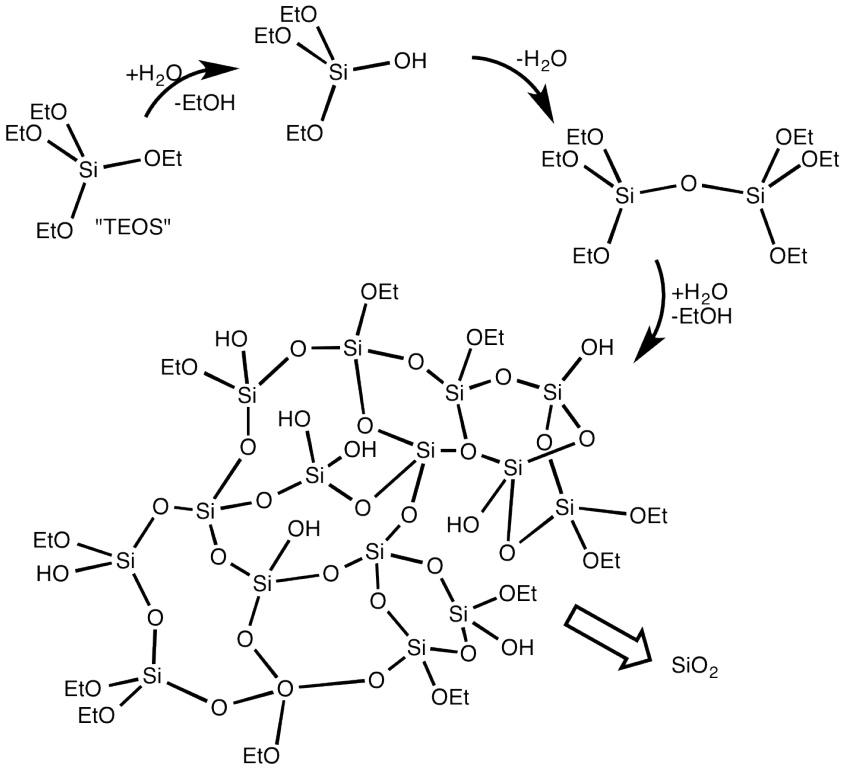


Figure 4.1: Hydrolysis and condensation of *TEOS* in the Stöber process [133].

In the preparation of silica nanoparticles, precursor tetraethylorthosilicate $(Si(OEt)_4$ or $TEOS)$ is hydrolyzed in alcohol (typically methanol or ethanol or iso-propanol) in the presence of ammonia as a catalyst. The general reactions are well known [134]:

$$
\begin{aligned}
& R'_x - Si(OR)_{4-x} + (4-x)H_2O \\
& \xrightarrow{\text{hydrolysis}} R'_x - Si(OH)_{4-x} + (4-x)ROH \\
& \xrightarrow{condensation} R'_x - Si(OH)_{(4-x)/2} + \frac{(4-x)}{2} H_2O
\end{aligned}
\tag{4.1}
$$

where R is an alkyl and R' is any organic group. x is an integer between 0 and 3, and polymerization is a composite reaction, and the order of the reactions has nothing to do with their molecularity [131]. The number of hydrolyzed groups *(4-x)* determines the reaction's molecularity.

The polymerization reaction steps of alkoxysilanes and organo-alkoxysilanes are shown below:

1. Hydrolysis and re-esterification:

$$\equiv Si - O - R + H_2O \longrightarrow \equiv Si - OH \longrightarrow \equiv +HO - R \tag{4.2}$$

$$\equiv Si - O - R' + H_2O \longrightarrow \equiv Si - OR' \equiv +H_2O \tag{4.3}$$

2. Condensation by producing water:

$$\equiv Si - OH + HO - Si \longrightarrow \equiv Si - O - Si \longrightarrow \equiv +H_2O \tag{4.4}$$

3. Condensation by producing alcohol:

$$\equiv Si - OH + HO - Si \longrightarrow \equiv Si - O - Si \longrightarrow \equiv +HO - R \tag{4.5}$$

Various groups in research have used a range of wet-chemistry methods to modify or coat colloids with *NPs* of noble metals [135]. The synthesis of silica spheres on *Ag/Au NPs* was carried out by adding *NPs* into the silica solution [136]. The hydrolysis and condensation of tetraethylorthosilicate (*TEOS*) in an alkaline alcohol/water mixture are important in controlling the homogeneity of the shell thickness. The silica spheres are a very promising choice as hard spherical substrates for the following reasons [137]:

1. Narrow size distribution can be achieved over a wider range,
2. Their surface silanol composition and the extent of hydrogen bonding can be modified by thermal treatment to change their reactivity,
3. Silanol groups can form coverlet links,

4. The isotropic interactions in an aqueous or organic suspension help to form ordered arrays on substrates,
5. The silica shells would protect the *Au/Ag NPs* surface to ensure stability against corrosion or environment driven degradation.

In the case of seeded growth $Au/Ag@SiO_2$ core-shell *NPs*, the renowned model, developed by *Ye et al. [138]* on gold or silver colloids and based on the aggregation model, may explain the discontinuous and a rough SiO_2 coating observed in Figure 4.2. Note that the nucleation is continuous and also that the primary nuclei are unstable. Nucleation and aggregation will proceed simultaneously to promote the growth of the SiO_2 shells [139]. Figure 4.2 shows a schematic growth mechanism of SiO_2 nano-shells/sphere. In Figure 4.2.a), the nucleated SiO_2 particles are in solution, and they start the process of slowly aggregating on the *Ag NPs* surfaces as shown in Figure 4.2.b). Thus the formation of core shell structures is characterized by a discontinuous SiO_2 coating (Figure 4.2.c)) and these particles, continuously filled with fresh nuclei, progressively decreases with increasing the reaction time (Figure 4.2.d)). As the nuclei agglomerates, the SiO_2 coating additionally grows by monomers, as the hydrolyzed monomers are in equilibrium with metallic particles [140, 141]. Finally, depending on how quickly the monomers are hydrolyzed, the settling nuclei may still undergo intraparticle densification before the *TEOS* hydrolysis is complete [142, 139]. Therefore, monomers addition creates a smoother coating. The SiO_2 shell growth on *Ag NPs* is a function of reaction time, temperature and material concentration [139].

Silica coating on gold/silver nanoparticles is achieved by the classic Stöber methodology involving tetraethyl orthosilicate (*TEOS*) to create an extremely branched and mesoporous chemical compound on the surface of gold/silver nanoparticles. The thickness of the silicon oxide layer on the gold/silver surface is controlled or tailored with reaction time and chemical agent concentrations with their PH [143]. The ensuing chemical compound compound on the silica surface has *-OH* group which act as chemical anchors for additional functionalization. Also, heterobifunctional silane linkers can promptly react with silica oxide, providing a way to connect a spread of ligands (like

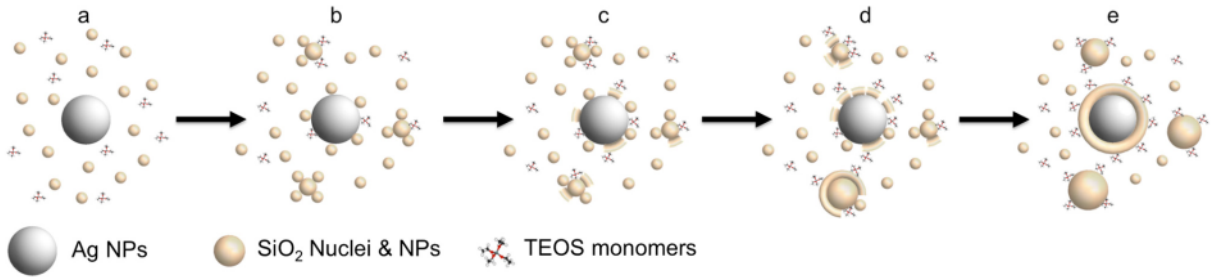


Figure 4.2: The SiO_2 shell development mechanism on the Ag core is depicted schematically. (a) SiO_2 primary nuclei arise in the initial stage and (b) slowly aggregate among themselves as well as onto $Ag\ NP$ surfaces and (c) to form ravined structures. These ravines are gradually filled with fresh SiO_2 nuclei (d) until the $Ag\ NPs$ are completely wrapped (e). $TEOS$ monomers are also introduced to NPs at the same time and contribute to the surface smoothing [139].

poly ethylene glycol) to the silica surface (see Figure 4.2). Ammonia acts as a catalyst that activates the SiO_2 surface to produce reactive silanol groups after nucleation of SiO_2 on the surface of the Au/Ag nanoparticle. The poly-condensation process itself depends on the pH value, temperature, composition of the reaction medium, stirring conditions [144].

There improved plasmonic devices that used $Ag@SiO_2\ NPs$ with a 5 nm shell thickness and have the maximum short-circuit current density of 13.44 mA/cm^2, which is up by 12% over the reference device [145]. The localized surface plasmon resonance and the light scattering effect caused by $Ag\ NPs$ and $Ag@SiO_2\ NPs$ were primarily responsible for those improvements.

The features of core–shell silica-based nanoparticles make them ideal for generating next-generation therapies. Because of their mesoporous nature, have a larger surface area, which allows for more surface modification [146]. The role of core–shell silica-based nanoparticle based injectable nanotherapeutics in drug delivery, biomedical imaging, light-triggered phototherapy, Plasmonic enhancers, gene delivery, magnetic hyperthermia, immunotherapy, and their potential as next-generation theragnostic [147].

4.2 Materials

Ethanol, isopropanol and ammonium hydroxide aqueous solution (28%) were purchased from Sigma-Aldrich. Ethylene glycol (EG, 99+%) was obtained from Acros Organics. Sodium citrate, trisodium citrate and polyvinylpyrrolidone (*PVP*) from Sigma Aldrich. Silver nitrate, titanium(IV) isopropoxide (*TTIP*), hydrocloric acid (*HCl*) and tetraethyl orthosilicate (*TEOS*) (98%) were also obtained from Sigma-Aldrich. Deionized (*DI*) water was used throughout all the experiments. All chemicals were used as received without further purification.

4.3 Sample Preparation

The *Ag/Au NPs*were prepared through wet chemistry, while SiO_2/TiO_2 nanoparticles were prepared using the sol-gel methods, that included the Stöber method, sintering, sedimentation, a standard cleaning of the nanoparticles, and self assembly. This process began with a modified Stöber method, used to generate monodispersed spheres deposition rate. The annealing temperature and the concentration of the starting solutions were optimised. Homogeneous films were deposited on clean microscopic glass slide by dip-coating at an optimized speed.

4.3.1 Synthesis of *Ag* nanoparticles

Ag NPs were synthsized by reducing 0.001 M of $AgNO_3$ in dionized water and 1% sodium citrate was used as a stabilizer and catalyst, the solution was stirred at 60 $^{\circ}C$ until the solution became pale yellow and it was allowed to cool at room temperature and it was centrifugated at 6000 rmp for 5 minutes and it was washed in distilled water, the process was repeated 4 times.

Note the actual measurements are:

1. O.0425 g of $AgNO_3$ was dissolved in 50 ml deionized water, where 25 ml of solution diluted in 100 ml of deionized water to make 0.001M $AgNO_3$.
2. 0.5 g sodium citrate was dissolved in 50 ml deionized water to make 1% of sodium citrate.

4.3.2 Synthesis of *Au* nanoparticles

1. 1 mM $HAuCl_4$ was reduced in 1% trisodium citrate ($Na_3C_6H_5O_7$) aqueous solution with sodium chloride ($NaCl$) as stabilizer under vigorous stirring at 80 $^{\circ}C$.
2. After refluxing for 15 min, the product was cooled to room temperature.

4.3.3 Synthesis of SiO_2 nanospheres

Through a modified Stöber method, SiO_2 nanospheres were synthesized using the following procedure: A 40 ml of ethanolic solution was placed in beaker, at room temperature. Under vigorous stirring, ammonia (2 mL, 28–30 %) and *TEOS* were subsequently added until a homogeneous solution was formed. After stirring for 3 h. The product was centrifugated at 6000 rmp for 6 min and repeatedly washed in dionized water, untill SiO_2 nanoparticles were obtained. The obtained spherical nanoparticles were sintered at 70 $^{\circ}C$ for 24 h. The thickness of SiO_2 *NPs* was controlled by adjusting the concentration of *TEOS*. Silica *NPs* of sizes varying from 20 nm to 80 nm were obtained.

4.3.4 Synthesis of $Ag@SiO_2$ core-shell *NPs*

10 ml of the freshly prepared *Ag NPs* was added to ethanolic solution (40 mL). Under vigorous stirring, ammonia (2 mL, 28–30%) and *TEOS* were subsequently added until a homogeneous solution was formed. After stirring for 3 h at room temperature, the solution was allowed to stay for a week, the product was washed with deionized water

after centrifugation at 6000 rmp for 6 min, and $Ag@SiO_2$ core–shells were obtained. The core-shells were placed in an oven at 70 $^{\circ}C$ over night to remove the residuals.

4.3.5 Synthesis of $Au@SiO_2$ core-shell *NPs*

Again the Stöber method was considered, $Au@SiO_2$ nanoparticles were prepared by adding the freshly prepared gold colloid solution (10 *mL*) into 40 *ml* ethanolic solution. Under vigorous stirring, drops ammonia (2 *mL*, 28–30%) and *TEOS* were subsequently added until a homogeneous solution was formed, After stirring for 3 h, the solution was allowed to stay for a week. The product was washed with water by centrifugation at 6000 rmp for 6 min, and $Au@SiO_2$ core-shell *NPs* were obtained. The core-shell were placed in an oven at 70 $^{\circ}C$ over night.

4.3.6 Synthesis of TiO_2 *NPs*

5 *ml* titanium tetraisopropoxide (*TTIP*) was added to an ethanolic solution (25 *ml*). Under vigorous stirring, after 30 min of stirring 2 *ml* of dionized water was to promote hydration added until a homogeneous solution was formed. After stirring for 3 h at room temperature, the solution was allowed was allowed to stay for a night, the product was washed with deionized water after centrifugation at 6000 rmp for 6 min, and TiO_2 nanospheres were obtained. The core-shells were placed in an oven at 70 $^{\circ}C$ over night to remove the residuals

4.3.7 Synthesis of $Ag@TiO_2$ core-shell *NPs*

10 *ml* of the *Ag NPs* was added to ethanolic solution (25 *ml*). Under vigorous stirring, 5 *ml* of titanium tetraisopropoxide (*TTIP*) was subsequently added until a homogeneous solution was formed. After stirring for 3 h at room temperature, the solution was allowed

was allowed to stay for a night, the product was washed with deionized water after centrifugation at 6000 rmp for 6 min, and $Ag@TiO_2$ core–shell *NPs* were obtained. The core-shell *NPs* were placed in an oven at 70 $^{\circ}C$ over night to remove the residuals.

4.4 Morphology analysis:

The morphological characterization were carried out using a High resolution Scanning Electron Microscope (SEM) operated in the scanning mode and using transmission electron microscope (TEM).

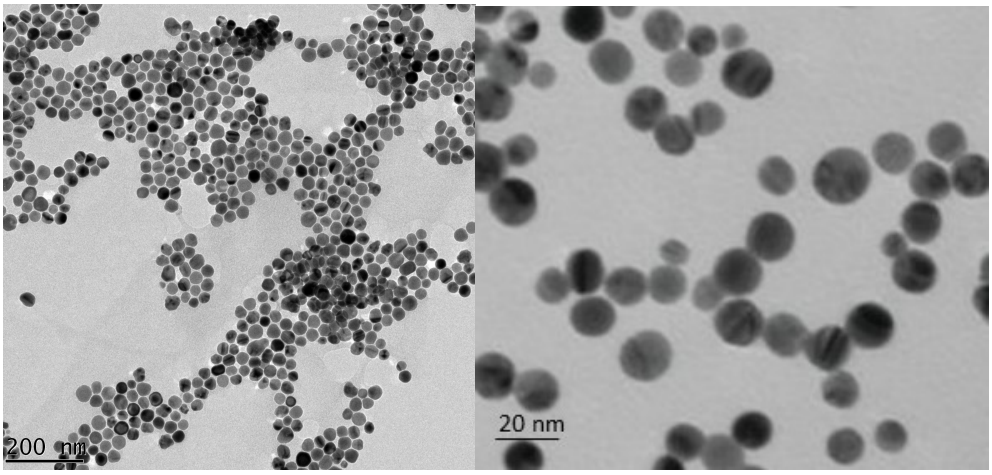
The TESCAN VEGA SEM uses variable pressure mode can be used to investigate non-conductive samples, and the EDS detector can be used to characterize elements in a sample. The TESCAN VEGA SEM uses a voltage range of 200 eV to 30 keV and 1pA to 2A beam current.

FEI Tecnai T12 Transmission Electron Microscope (TEM) having a 20 to 120 kV operating voltage range. Magnifications of thin samples (200 nm) up to 700,000 times, an energy-dispersive X-ray spectroscopy (EDS) system, a Gatan MSC794 CCD camera for digital image acquisition, and a video camera for video-rate recording at moderate magnifications are all included in the capabilities.

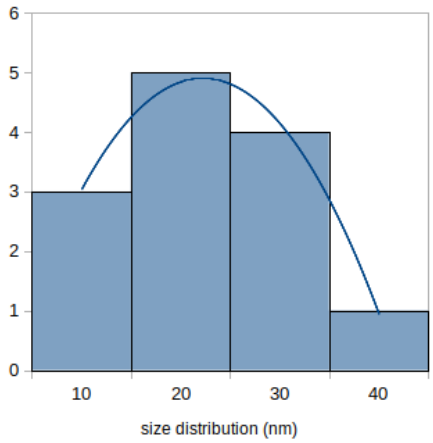
Thus, the geometrical aspects of the *NPs* such as size, shape, and sample chemical composition (through an energy dispersive X-ray spectroscopy (EDX) in the SEM) could be determined. Both TEM and SEM, enables one to study the texture of the sample including the size and shapes of the particles, as well their dispersity. To minimize space charge effects due to the insulating *NPS* the samples were coated with gold-palladium at room temperature and the *NPs* were sintered in air at different temperatures (from 60 $^{\circ}C$ up to 200 $^{\circ}C$). The size of the *Au NPs, Ag NPs*, SiO_2 nanospheres and $Ag@SiO_2$ core-shell *NPs* are were determined using an open source software called ImageJ [148].

4.4.1 TEM Morphology analysis of *Ag NPs*

TEM (transmission electron microscope) images of *Ag NPs* were captured. For this analysis *Ag NPs* were deposited on a TEM copper (*Cu*) grid coated with carbon by drop casting. Figure 4.3 shows the randomly distributed spherical like *Ag NPs* on the *Cu* grid at a magnification of 200× they have an average diameter of 20±2 *nm* are displayed in the histogram in Figure 4.3c.



(a) Ag *NPs* (b) Magnified Ag *NPs*

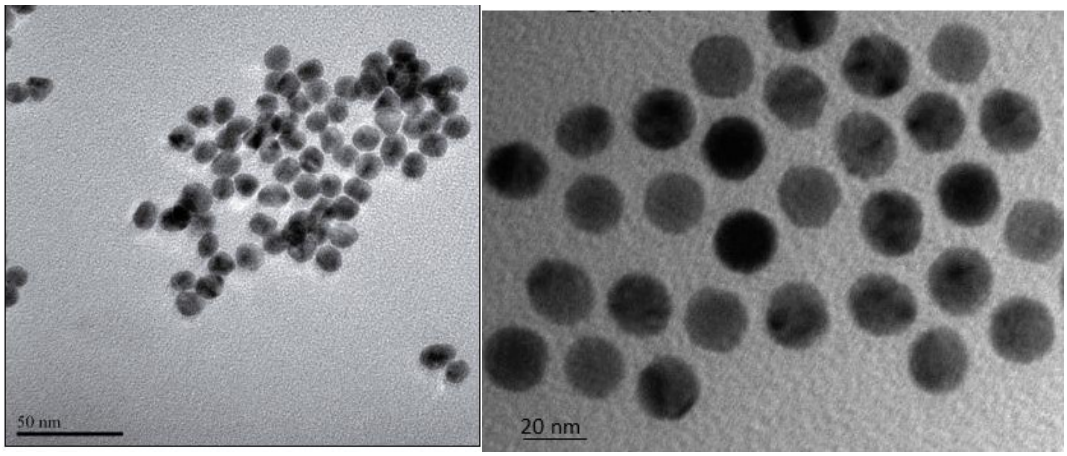


(c) Average size

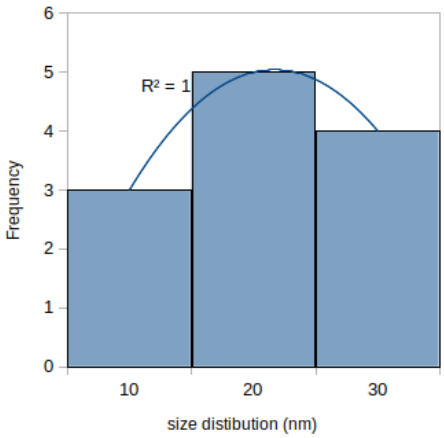
Figure 4.3: TEM image (a) of *Ag NPs* distributed on the *Cu* grid surface at magnification of 200× and image (b) shows zoomed in image of *Ag NPs* with 20 *nm* diameter shown in image (c) from the histogram showing of the average size of *Ag NPs*.

4.4.2 TEM Morphology analysis of *Au NPs*

The *Au NPs* were dispersed in distilled water. TEM images displayed spherically shaped *NPs* and with an average size of 20 ± 2 *nm* as shown in Figure 4.4.



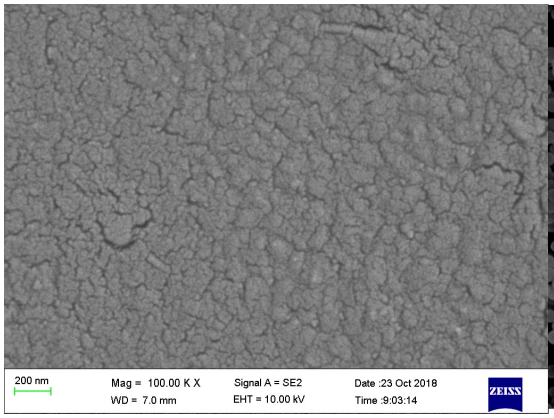
(a) Au *NPs* (b) Au *NPs*



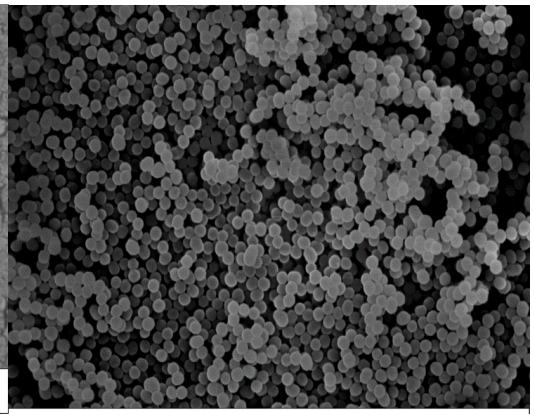
(c) Average size

Figure 4.4: TEM image (a) of *Au NPs* distributed on the *Cu* grid surface at magnification of 50× and image (b) shows zoomed in image of *Au NPs* with 20 *nm* diameter shown in the histogram of image (c)

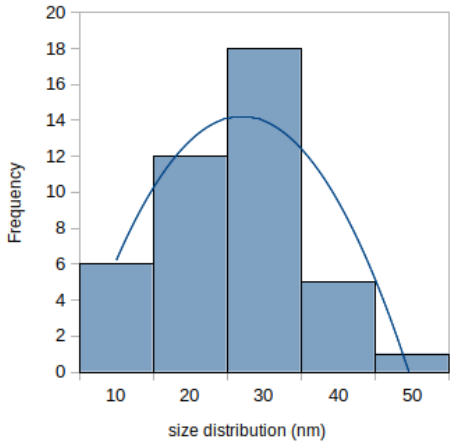
4.4.3 SEM Morphology analysis of SiO_2 nanospheres



(a) 35 *nm* SiO_2 nanospheres



(b) 35 *nm* SiO_2 nanospheres



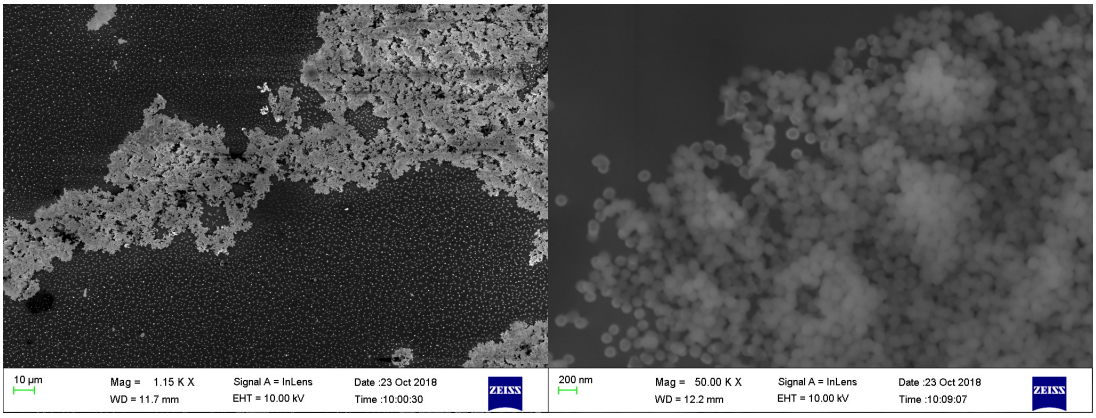
(c) Average size

Figure 4.5: The SEM image (a) shows the resulting film comprising of SiO_2 nanospheres (thermally treated at 70 $^{\circ}C$), image (b) shows the uniformly distributed *NPs* on the surface and image (c) shows histogram of the average size of SiO_2 nanospheres with a diameter of 35 *nm*.

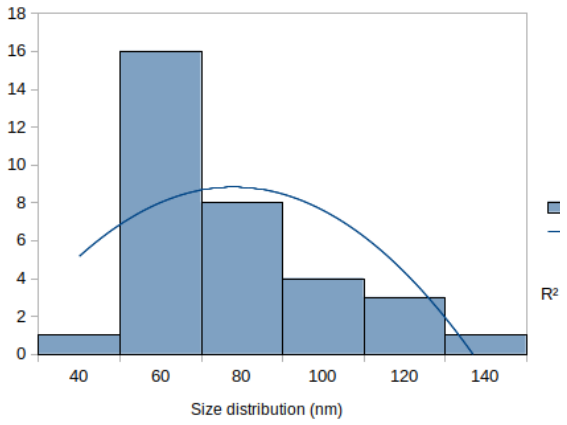
Figure 4.5, shows the SiO_2 nanospheres, which were thermally treated at 70 $^{\circ}C$. We obtained an average 35 ± 2 *nm* spherical nanoparticles in diameter and were uniformly distributed on the surface of a microscopic glass slide. There were some cracks observed in Figure 4.5a, probably because these *NPs* were exposed to air when sintering. The

distribution of these particles on the substrate surface has great impact on the absorption of light, together with their size and shape (see section 4.5).

When interstitial spaces of the core-shell *NPs* or nano-spheres are filled with a high-index material at high temperatures [149], shrinkage of the core-shell *NPs* at high temperatures might course cracks, resulting in poor optical properties. Low defect-density core-shell *NPs* can be achieved by first sintering them, the thermal expansion coefficient of SiO_2 which is $0.55 \times 10^{-6}/K$ make it easier to estimate the maximum temperature to work with.



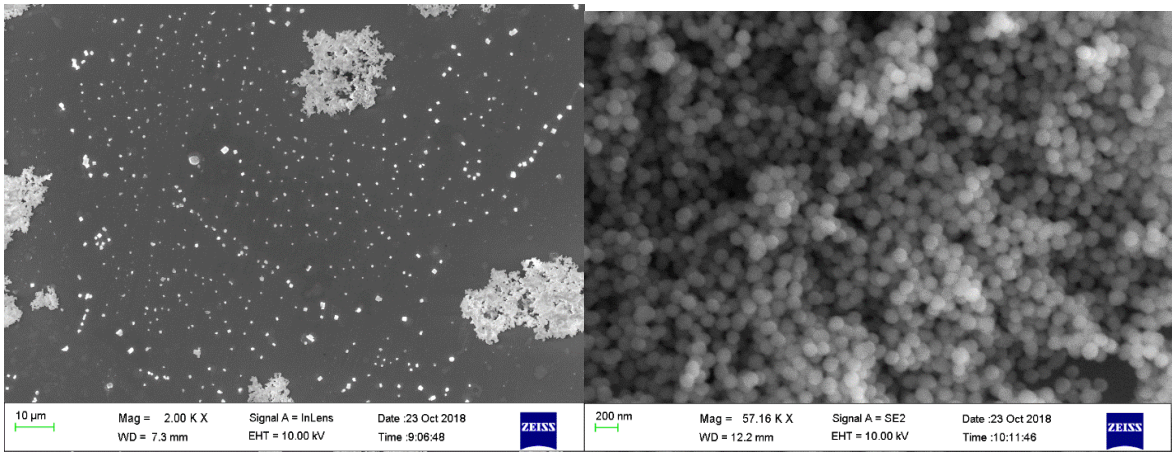
(a) 65.8 *nm* SiO_2 nanospheres (b) 65.8 *nm* SiO_2 nanospheres



(c) Average size

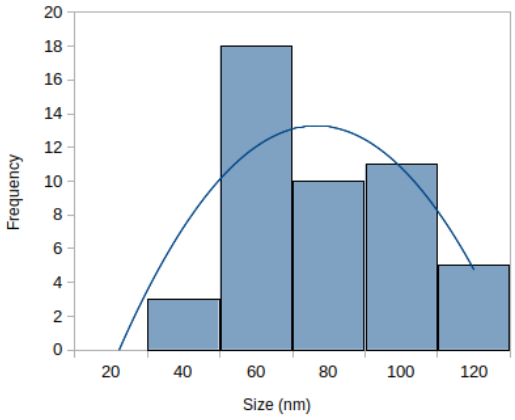
Figure 4.6: Image (a) shows the SiO_2 (thermally treated at 100 $^{\circ}C$) spheres, image (b) shows uniformly shaped spheres magnified. Image (c) shows the histogram of the average size of SiO_2 *NPs* with a diameter of 65.8 *nm*

Figure 4.6 shows the SiO_2 nanopspheres/*NPs* which were thermally treated at 100 $^{\circ}C$ which resulted in spherical *NPs* with a diameter of 65.8$\pm$2 *nm* (from the histogram in Figure 4.6b). Looking at the entire surface it is noted that some of the silica spheres are not uniformly distributed but rather clustered together and this could have attributed due to the depositing speed of the SiO_2 nanospheres on glass substrates and substrates surface kinematics.



(a) 72.28 *nm* SiO_2 nanospheres

(b) 72.28 *nm* SiO_2 nanospheres

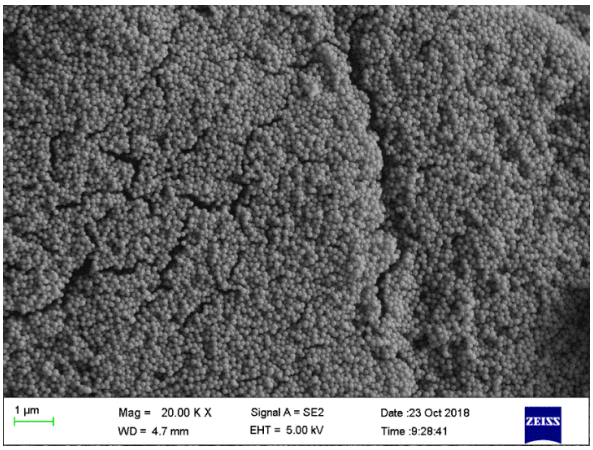


(c) Average size

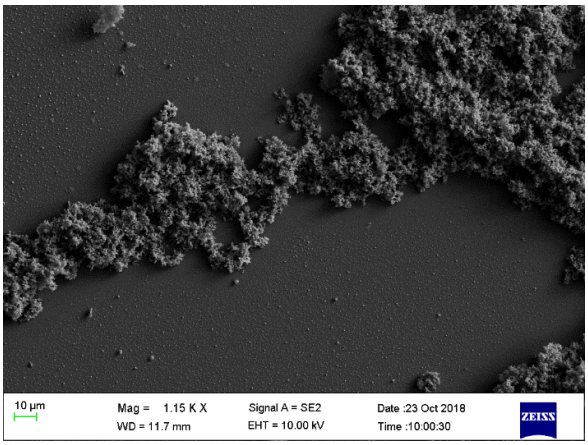
Figure 4.7: SEM image (a) shows the SiO_2 nanospheres (which were thermally treated at 150 $^{\circ}C$), image (b) shows how the spheres are distributed on the surface and image (c) shows the histogram of the average size of SiO_2 *NPs* with a diameter of 72.28 *nm*.

Figure 4.7 shows SEM images of 72.28$\pm$1.34 *nm* diameter SiO_2 nanospheres formed after annealing at 150 $^{\circ}C$, which resulted in spherical *NPs*. We observe a similar non-

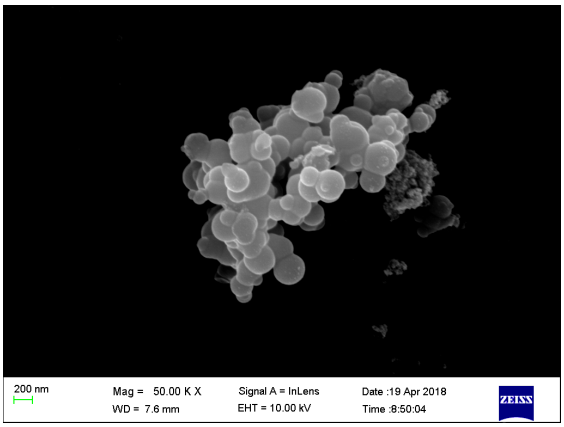
uniform distribution of the *NPs* thermally treated at 100 $^{\circ}C$ (see Figure 4.6). The increment in particles confirms that the particle size is dependent on the annealing temperature.



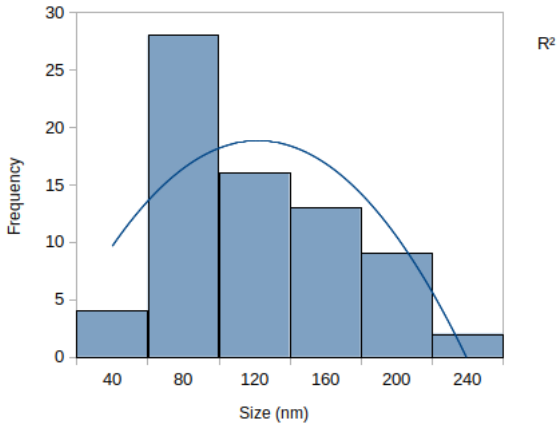
(a) 85.51 *nm* SiO_2 nanospheres



(b) 85.51 *nm* SiO_2 nanospheres



(c) SiO_2 nanospheres



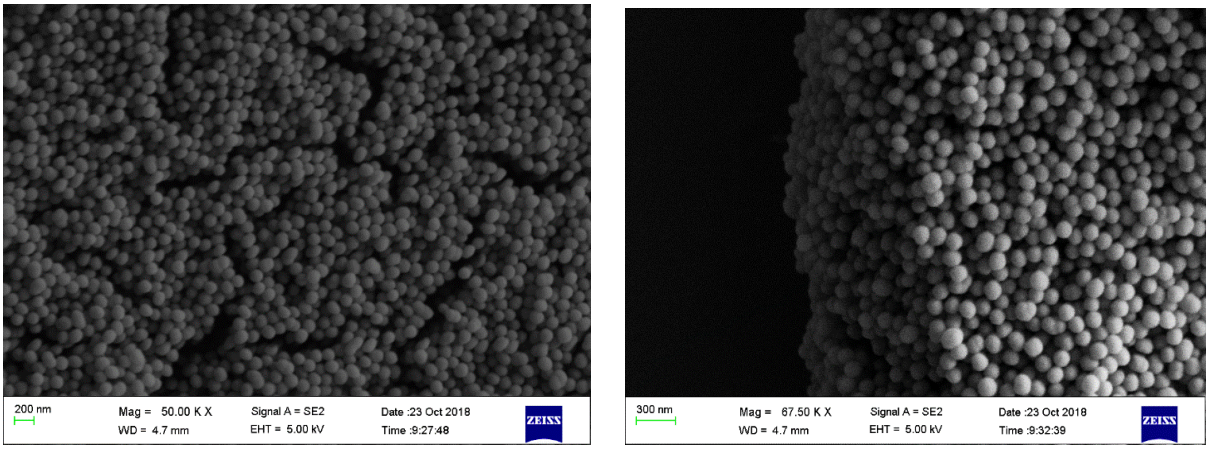
(d) Average size

Figure 4.8: SEM image (a) shows the SiO_2 nanospheres (thermally treated at 200 $^{\circ}C$) uniformly distributed, image (b) and (c) shows the magnified nanosphere uniformly distributed and ahaped *NPs*. Image (d) show the histogram of the average size of SiO_2 *NPs* with a diameter of 85.51 *nm*.

Figure 4.8 shows the SiO_2 nanospheres that were thermally treated at 200 $^{\circ}C$, that have resulted in spherical *NPs* having diameter of 85.51 $\pm$ 2 *nm*, we noted that the particles are very clustered together. From the zoomed in or magnified images in Figure

4.8c, the *NPs* are uniformly sized and spherically shaped as seen from the edge of the samples.

Figure 4.9 further shows the SiO_2 spheres which were thermally treated at 200 $^{\circ}C$, a many layered structures observed. The effect of the size of the nanoparticles was studied by employing optical absorption spectroscopy in section 4.5

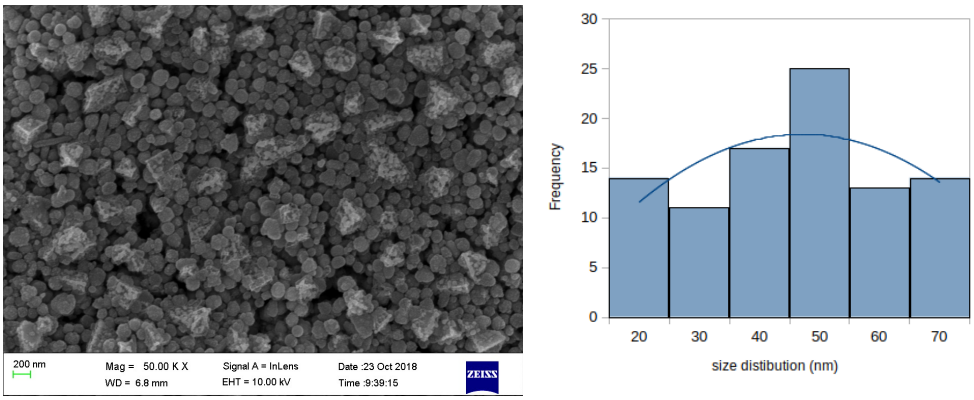


(a) (b)

Figure 4.9: The left image shows the top view of SiO_2 spheres and the one on the right shows how the edge of the sample magnified at 200μm and 300μm.

4.4.4 SEM Morphology analysis of $Ag@SiO_2$ core-shell *NPs*

Figure 4.10 shows the $Ag@SiO_2$ core-shell *NPs* that were thermally treated at 100 $^{\circ}C$, that have resulted in spherical *NPs* having diameter of 60 $\pm$ 2 *nm*, we noted that the particles are very clustered together and many layered structures were observed.



(a) $Ag@SiO_2$ core-shell *NPs* (b) Average size

Figure 4.10: TEM images (a) showing the $Ag@SiO_2$ (thermally treated at 100 $^{\circ}C$) spheres non-uniformly distributed and shaped. Image (b) shows the histogram of the average size of the core-shell *NPs* with a diameter of 60 *nm*

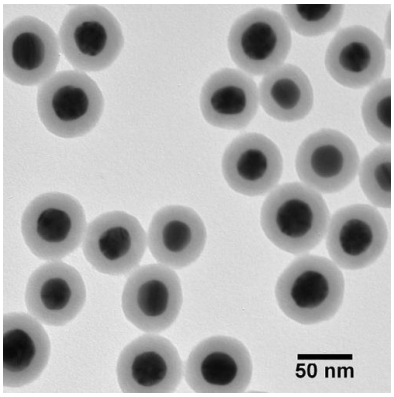
.

4.4.5 TEM Morphology analysis of $Au@SiO_2$ core-shell *NPs*

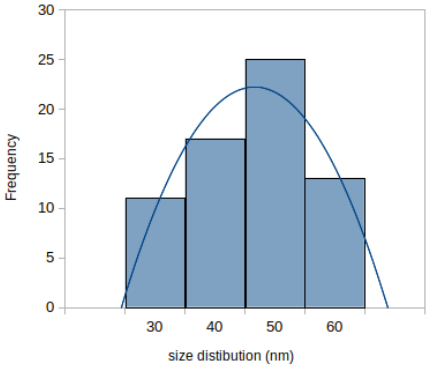
Based on a series of experiments, the optimized conditions for synthesizing core-shell $Au@SiO_2$ core-shell *NPs* were determined: where the *TEOS* hydrolysis was discovered to be very effective/reactive at room temperature and a sintering temperature of 100 $^{\circ}C$.

Figure 4.11 shows TEM images of uniformly spherically shaped $Au@SiO_2$ core-shells *NPs* and also displays a histogram of the average size of the $Au@SiO_2$ core-shell *NPs*. The overall size distribution of $Au@SiO_2$ core-shell *NPs* is about 58 ± 2 *nm* as shown if Figure 4.11b. The thickness of the silica shell can be controlled from 5 to 20 *nm* to optimize the plasmonic enhancement of core *(Au) NPs*. From TEM observation, $Au@SiO_2$ core-shell *NPs* samples are composed mainly of single particles, with only a few aggregates of two or more *Au* cores.

Table 4.1 below shows the optimal sintering temperature of *Ag/Au NPs*, $Au/Ag@SiO_2$ core-shell *NPs* and SiO_2 nanospheres when they were prepared, as well their shapes and sizes. The Standard deviation on Table 4.1 shows the dominating sizes of *NPs*. From



(a) $Au@SiO_2$ core shells



(b) Average size

Figure 4.11: TEM images (a) showing the $Au@SiO_2$ core-shell *NPs* (thermally treated at 100 $^{\circ}C$). Image (b) is the histogram showing the average size of the core-shell *NPs* having a diameter of 57.86 *nm*.

the table, it is noted that the shape of the *NPs* does not change but the size of the *NPs* is more dependent on the sintering/synthesizing/annealing temperature. The shape of *NPs* remains the same because the synthesizing or rather the fabrication methods remains the same through and the low temperature that are being explored cannot affect the shape or deform the shape of *NPs*. It should be noted that the *NPs* were activated to reduce surface energies and remove wet residuals. And having core-shell *NPs* reduces agglomeration of metallic *NPs* and as well thermalization.

In summary, a method to achieve a versatile, fast, simple, cheap synthesis of $Au/Ag@SiO_2$ core-shell nanoparticles were prepared. We observed a silver/gold seeded SiO_2 growth from an non-uniform to a continuous coating. The temperature dependence of SiO_2 *NPs* growth is well reproduced by a general first-order kinetics method [143].

Table 4.1: Temperature dependence on the diameter and shape of single and core-shell nanoparticles

Sample Name	**Sintering temperature** ($°C$)	**Size** (nm)	**Standard deviation**	**Shape**
SiO_2	70	35±1	6.28	spherical
SiO_2	100	65±2	4.92	spherical
SiO_2	150	72±2	3.15	spherical
SiO_2	200	85±2	7.44	spherical
$Ag@SiO_2$	100	60 ± 2	7.53	spherical
$Au@SiO_2$	100	58 ± 2	8.32	spherical
Ag	80	20 ± 1	9.26	seeds
Au	80	20 ± 1	8.92	seeds

4.5 Optical Properties Analysis

This section presents the optical properties of the synthesized nanostructures, related to their morphology. The absorption and transmission spectra have been recorded using established by UV-Vis operating in the range between 200 *nm* and 900 *nm*. Before

performing any analysis such as absorption or transmission a baseline correction was done allows the conservation of energy to be followed or held. A Zero/Baseline Correction is applied before analyzing any samples, where a 100%T baseline correction (100%TBaseline) and a zero-line correction (0%TBaseline) to the sample scan is performed with the raw transmission data %T. A clean microscopic glass slide used in a single beam incident.

A study concerning how the type of depositing technique has an effect on the absorption of core-shell *NPs* was carried out, using dip coating and spin coating methods. In both cases a single layer was deposited as a thin layer on a glass slab. The synthesis condition for the $Ag@SiO_2$ core-shell *NPs* were the same for both techniques.

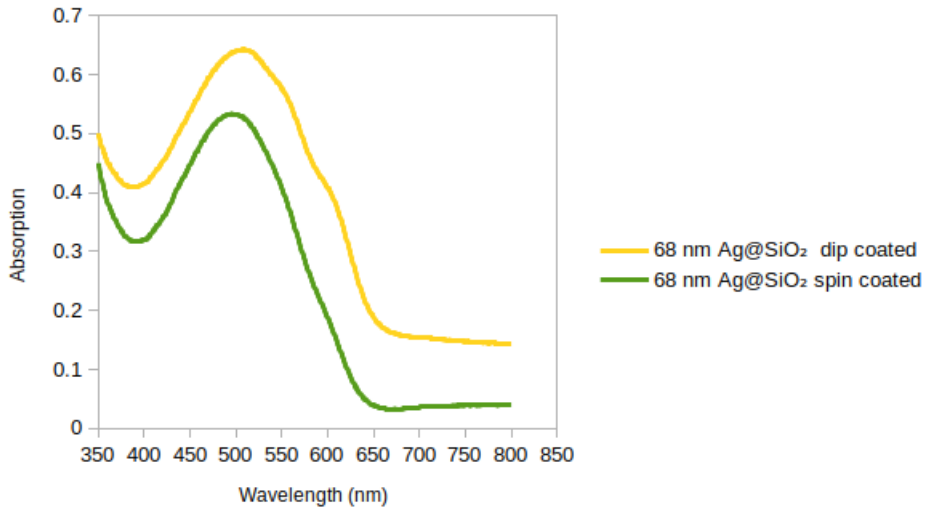


Figure 4.12: Absorption spectra of $Ag@SiO_2$ core-shell *NPs* deposited with two different methods (dip and spin coating).

Figure 4.12 shows a plasma resonance at around 520 *nm* for the $Ag@SiO2$ core-shell *NPs* deposited as a thin layer on a microscopic glass slide using the two contrasting methods. It should be noted that for each sample, a single layer was deposited and then after at 100 $^{\circ}C$ for 24 hours. The absorption intensity was higher for the $Ag@SiO_2$ core-shell *NPs* that were dip coated than the ones that were spin coated, but we see the same plasmon resonance at 520 *nm*. This indicates that dip coating gives a more uniform layer than spin coating [150].

After determining that dip coating is the best method of depositing the *NPs*. Further studies of the absorbance of silica, titania *NPs* coating noble metallic *NPs* such as gold and silver were carried out. Note that all the core-shell *NPs* under study were activated in an oven for 4 hours at 300 $^{\circ}C$ before performing any analysis.

Figure 4.13 shows the absorption spectra of SiO_2 spherical *NPs* that were synthesized at different temperature as from 70, 100, 150 and 200 $^{\circ}C$, which resulted in different particle sizes from 35, 65, 72 and 85 *nm* respectively. Figure 4.13 shows an increase in the absorption intensity as the size of the SiO_2 nanospheres increases. The monodispersed SiO_2 materials approach the quality of nanospheres and exhibit a resonance at 550 *nm* with an increase of the size of SiO_2 nanosphere. However an increase in the absorption intensity is accompanied by a peak width reduction. The peak becomes sharper with increasing diameter of the SiO_2 nanosphere. It is then noted that the 85 *nm* SiO_2 *NPs* sintered at 200$^{\circ}C$ have a lower absorption intensity as compared to the 65 *nm* spherical SiO_2 *NPs* synthesized at 100$^{\circ}C$. This now indicates that the 65 *nm* spherical silica nanoparticles have the best optical absorption compared to all the nanospheres/nanoparticles on this study. Note that if the synthesizing temperature was drastically increased there would be deformation of the shape of the nanospheres resulting in very low optical absorption [151]. The low optical absorption observed is due to the low softening temperatures of the SiO_2 *NPs*.

For the nanoparticles prepared in this study, we noted a sharpening of the peaks as the size of the SiO_2 *NPs* increases resulting from the synthesizing temperature. The sharpening, may be due to the non-homogeneous polarization of the particles in the electromagnetic field and also related to retardation and multiple excitation effects. This is referred to as the extrinsic size effect [152, 114] (see Figure 4.13). It was also noted that for small particles such as 35 *nm* SiO_2 *NPs* they have broader resonance which may have resulted to the particles in-homogeneity. From Figure 4.13, a 65 *nm* SiO_2 nanosphere had better absorption, thus the $Ag@SiO_2$ core-shell *NPs* were synthesized at 100 $^{\circ}C$.

Figure 4.14 shows the effect of introducing *Au NPs* into SiO_2 nanospheres to pro-

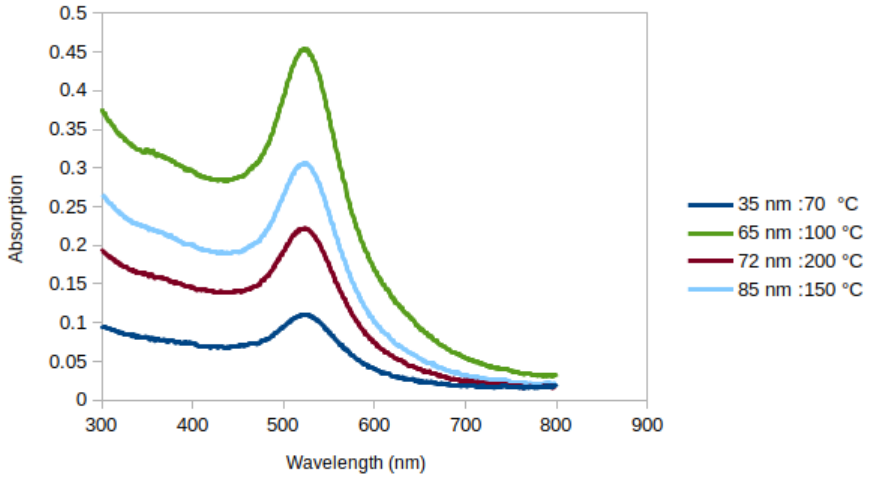


Figure 4.13: The absorption spectra of spherical like SiO_2 *NPs* synthesized at 70, 100, 150 and 200 $^{\circ}C$ respectively

duce $Au@SiO_2$ core-shell *NPs*. The absorption spectra from Figure 4.14, shows the absorbance of a 20 *nm* spherical *Au NPs* dispersed in deionized water, having a broad plasmon resonance at the 550 *nm*, characterised by local surface plasmon resonance (*LSPR*). Broadening of the peaks is usually an indication of the polydispersity of the *NPs* as seen in figure 4.11. It is also observed that $Au@SiO_2$ core-shell *NPs* have a plasmon resonance at 550 *nm*, is similar to that of *Au NPs*. Accompanied by an increase in absorption intensity. The shell thickness was varied from 15 *nm* (for a 50 *nm* diameter $Au@SiO_2$ core-shell *NPs*) to 25 *nm* (for a 70 *nm* diameter $Au@SiO_2$ core-shell *NPs*). The shell thickness was calculated using the following equation

$$shell\ thickness = \frac{(diameter\ of\ nanoparticle) - (diameter\ of\ core)}{2} \tag{4.6}$$

LSPR peak position is greatly influenced by the silica shell thickness or rather the dielectric environment/properties [152]. There was a blue shift plasmon resonance noted in Figure 4.14, the shift attributed to the encapsulation of *Au NPs* and increasing particle dimension. From Figure 4.14, due to the shell thickness size change as the concentration of *TEOS* increases. The variation in position and intensity of the plasmon resonance upon encapsulation is attributed to the change of the dielectric medium of the metal (*Au NPs*) plus the surrounding matrix or oxides (SiO_2) upon encapsulation [153]. This adds

to the intrinsic bulk like ones, such as electron-electron and electron-phonon scattering, an additional electron-scattering. The *LSPR* of particles smaller than the intrinsic electron mean free path is dramatically broadened (typically 20-30 *nm* in noble metals). This is in good agreement with particle ensemble observations, however there are many variation in the reported estimates of the surface scattering contribution [154].

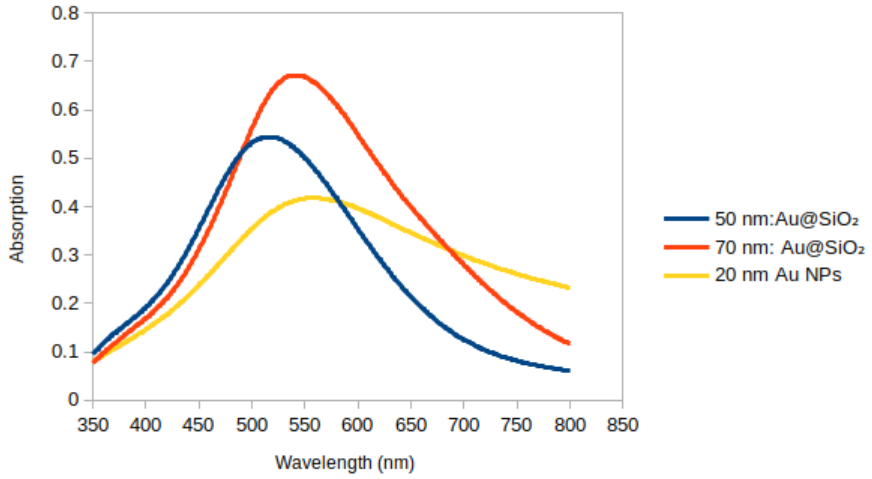


Figure 4.14: The absorption of *Au NPs* and $Au@SiO_2$ core-shell *NPs* having different *Au NPs* concentrations.

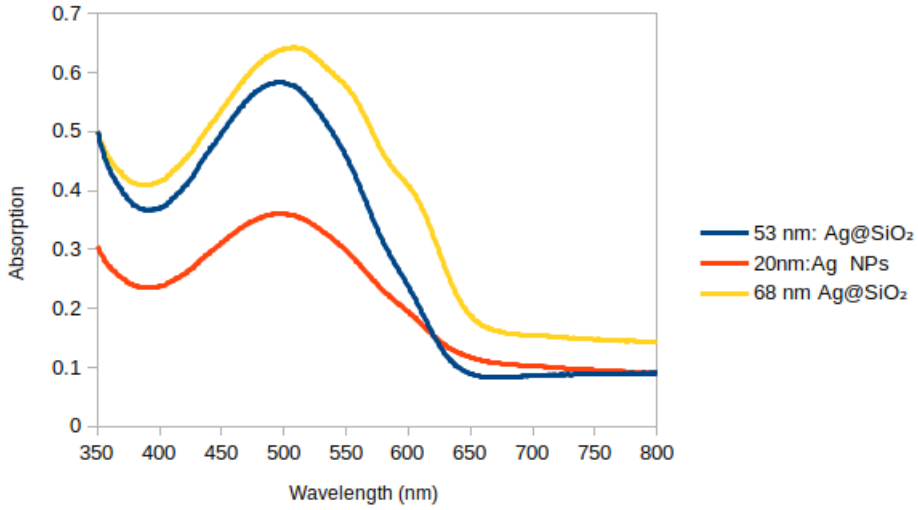


Figure 4.15: Absorption spectra of SiO_2 nanospheres, *Ag NPs* and $Ag@SiO_2$ core-shell *NPs*.

From Figure 4.15, the plasmon resonance of a 20 *nm* spherical *Ag NPs* at around

500 *nm*, which is very unlikely common for small silver nanoparticles, it may suggest that there impurities on the samples or the substrate. $Ag@SiO_2$ core-shell *NPs* shows a plasmon resonance at 525 *nm*, we observed a red shift as the shell thickness increases, which was the trend also noted in a paper by Zhi-Yuan [143]. The shell thickness was then increased from 16.5 *nm* (for a 53 *nm* diameter $Ag@SiO_2$ core-shell *NPs*) to 24 *nm* (for a 68 *nm* diameter $Ag@SiO_2$ core-shell *NPs*). On the other hand we observe an increase on absorption as the size of $Ag@SiO_2$ core-shell *NPs* increases, maintaining a plasmon resonance at 520 *nm* for both 53 *nm* and 68 *nm* $Ag@SiO_2$ core-shell *NPs*. Then from these results it can be concluded that $Au@SiO_2$ and $Ag@SiO_2$ core-shell *NPs* can be used to improve photon absorption through surface plasmon resonance and can be used in commercial *a-Si* solar cells. The Local Surface Plasmon Resonance (*LSPR*) of *Ag/Au NPs* appeared to be greatly dependent on the dielectric environment, thus the introduction of silica nanospheres exerted a great influence in the absorption of the samples. The plasmon resonance of *Ag/Au NPs* varies with the refractive index of the SiO_2 dielectric layers.

Another study consisting of titania nanospheres, was carried out, as to see which oxides act as a better shell.

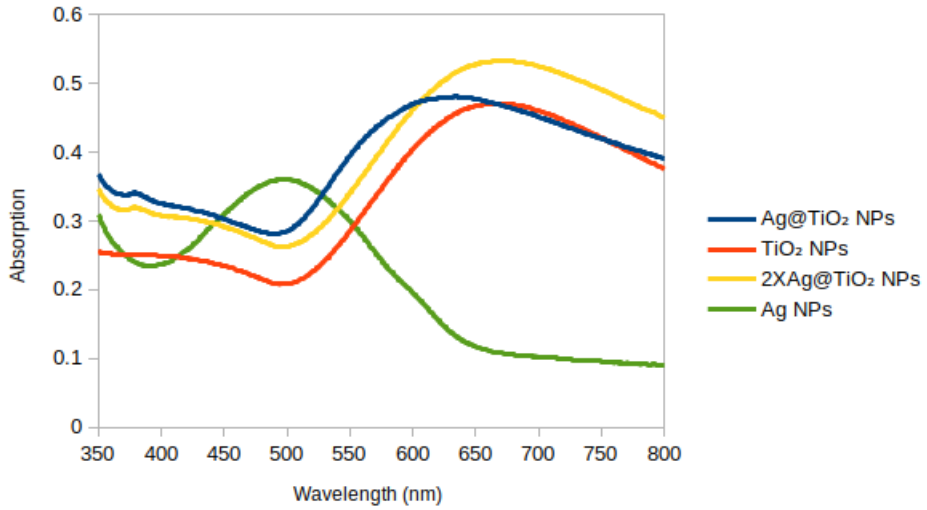


Figure 4.16: Absorption spectra of *Ag NPs*, TiO_2 *NPs* and $Ag@TiO_2$ core shells *NPs*.

The absorption spectra of *Ag NPs*, TiO_2 *NPs* and $Ag@TiO_2$ core-shell nanoparti-

cles is displayed in Figure 4.16. The absorption plasmon resonance of a 20 *nm* spherical *Ag NPs* is observed at 500 *nm*, while that of TiO_2 *NPs* appeared at 650 *nm*. *Ag NPs* had a strong absorption in the visible light region owing to the surface plasmon resonance.

After capping *Ag NPs* with TiO_2 shells, a plasmon resonance was was observed at 650 *nm*, where the absorption band blue shifted by 50 *nm* to 600 *nm* (as when compared to resonance of TiO_2 *NPs*) when a single layer was deposited on a glass slab. After a double layer were deposited, the peak shifted to 640 *nm* with an increase in the absorption intensity, as a result the surface plasma has improved (now light passes through symmetric two metallic *NPs* at a space covered by the shell thickness of the core-shell *NPs*) and might also be due to the high dielectric properties of TiO_2 shells (at 640*nm*, the refractive index titania is $n_{(TiO_2)}$= 2.5796 [155]).

In addition, $Ag@TiO_2$ nanoparticles showed very strong absorption between 600 and 650 *nm*. As compared to *Ag NPs*, the lower absorbance could be attributed to the lower *Ag* content. The -50 *nm* shift might also be due to asymmetrical silver nanoparticles sizes.

The increase in absorption intensity is attributed to the increase in the shell thickness. The nanoparticles size variations should lead to variations in the resonance peak. The TiO_2 *NPs* size is dependent on the synthesizing temperature as well as in the concentration of titanium isopropoxide (*TTIP*).

The transmission spectra of silica core-shell NPs

Figure 4.17 displays the transmittance of SiO_2 *NPs* and $Ag@SiO_2$ core-shell *NPs* spin coated with a single and double layers of *Ag* nanoparticles. The transmittance of SiO_2 *NPs* and double layer $Ag@SiO_2$ (given as $2xAg@SiO_2$ on Figure 4.17) core-shells *NPs* is 58% at 270*nm* which is 8% higher compared to that of single layer coating of $Ag@SiO_2$ core–shell *NPs* which is about 50% at 370 *nm* as shown in Figure 4.17. The transmittance shift might have occurred due to non-uniform layers from spin coating and the *NPs* size variation.

The measured transmittance (T) can be used to calculate the absorption coefficient

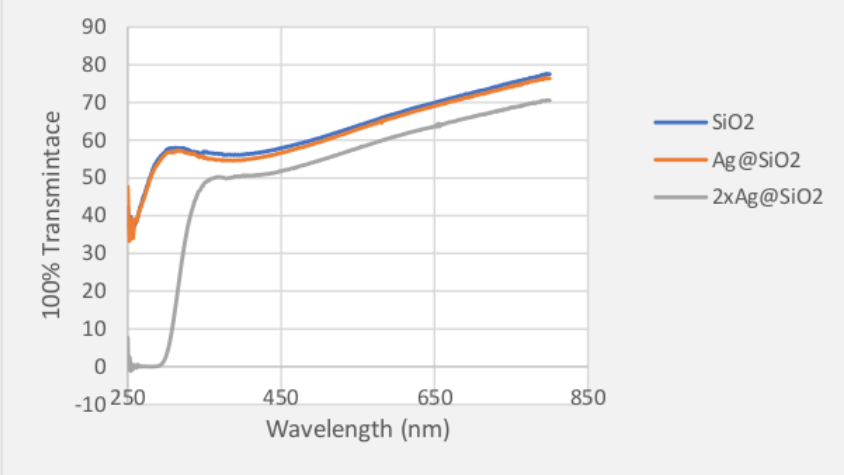


Figure 4.17: The transmittance of spherical *Ag NPs, SiO_2 NPs* and *$Ag@SiO_2$* core-shell *NPs* deposited on a microscopic glass slide.

(α) using the following formula [156]

$$\alpha = \frac{2.303 log(1/T)}{t} \tag{4.7}$$

where t is the thickness of the sample. Note that

$$T = \frac{(1-R^2)e^{-(\alpha t)}}{1-Re^{-\alpha t}} \tag{4.8}$$

where R is the reflectance. We may solve for R to obtain

$$R = \frac{e^{-\alpha t} + \sqrt{Te^{-\alpha t} - Te^{-3\alpha t} + T^2 e^{2\alpha t}}}{e^{-\alpha t} + Te^{-2\alpha t}} \tag{4.9}$$

Therefor the refractive index is

$$n = \frac{(R+1) + 2\sqrt{R}}{R-1} \tag{4.10}$$

Applying the above equation to a *$Ag@SiO_2$* core-shell nanoparticle with diameter a 70 *nm*, we obtain refractive index of 1.49 for a single layer and for double layer is 1.80.

4.6 The *J–V* characteristics

4.6.1 Introduction

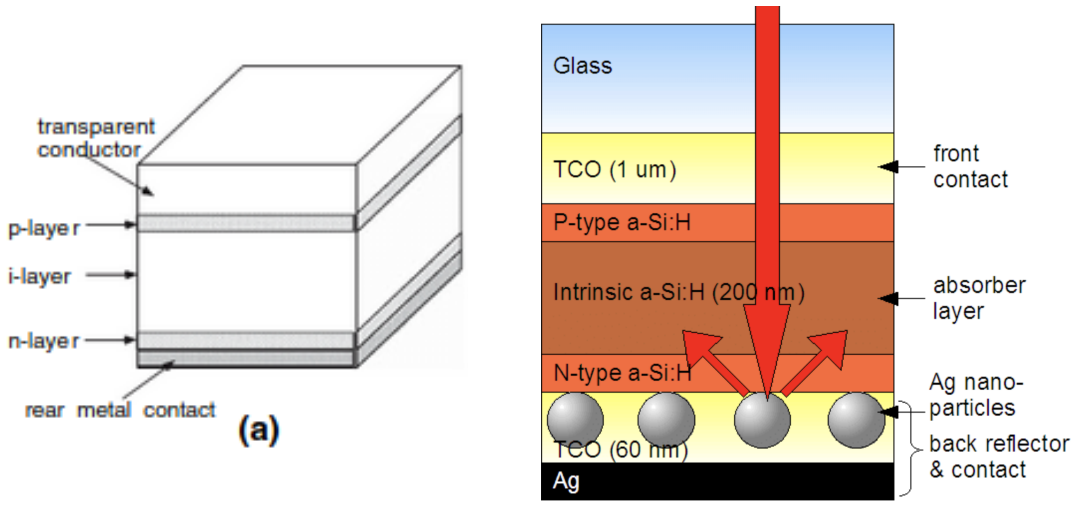
Commercial amorphous silicon (*a-Si*) solar cells were studied, which were modified be depositing a photonic crystal and metallic *NPs*. Standard amorphous silicon (*a-Si*) solar cells have been used in consumer products such as calculators and digital watches since the early 1980s. The *a-Si* is fabricated at low temperature, so that it can allow about 10% (atomic) hydrogen to be incorporated [157]. Incorporation of hydrogen forms dangling bonds in *Si* and improves the absorption coefficient as hydrogenated *Si* to a direct band-gap semiconductor. The device *(a-Si solar cells)* consists of three layers that were either deposited as *p-i-n* or *n-i-p* [158]. The *p* and *n* layers are usually doped with any material forming a 20 *nm* layer in a *a-Si* thin film. The *i*-layer is an intrinsic layer expanding the active layer which is responsible for generating photocurrent (electron-hole) in the cell, where excitons are split to form free charge carriers. The *i*-layer is a significant layer in *a-Si* solar cells [159].

The *p-i-n* sequence implies that the *p*-layer is deposited first, then the *i*-layer is the second layer deposited and the *n*-layer is the last one to be deposited on the substrate [158, 159].

In this section the layers of *Ag NPs*, SiO_2 *NPs*, $Ag@SiO_2$ core-shell *NPs*, TiO_2 *NPs* and $Ag@TiO_2$ core–shell *NPs* were deposited on the top surface of the commercial *a-Si* solar cell to enhance light trapping.

4.6.2 The *J–V* characterization for *Ag NPs* SiO_2 and $Ag@SiO_2$ core-shell *NPs* on *a-Si* solar cell

Figure 4.19 shows the *J–V* curve of a commercialized *a-Si* solar incorporated with *Ag NPs*, SiO_2 *NPs* and $Ag@SiO_2$ core-shell *NPs*. Under AM1.5 illumination, the area



(a) (b)

Figure 4.18: (a) Single-junction amorphous silicon solar cell and (b) Individual cells deposited onto a glass sheet are laterally connected in series by the approach shown [157]

illuminated is about 2.2 cm^2. It is noted that there is a significant increase in current density upon incorporation of $Ag\ NPs$, SiO_2 nanospheres and $Ag@SiO_2$ core-shell NPs layers. The extracted parameters from Figure 4.19 are current density (J_{sc}), fill factor (FF), open circuit voltage (V_{oc}), series resistance (R_s), shunt resistance (R_{sh}) and photo-conversion efficiency (PCE) of the solar cells are tabulated in Table 4.2.

Table 4.2 shows that J_{sc}, FF and PCE of the commercialized a-Si solar cells incorporated with $SiO_2\ NPs$, $Ag\ NPs$ and $Ag@SiO_2$ core-shell NPs increased respectively, this is due to the plasmon resonance of effect from $Ag\ NPs$. While the V_{OC} remained partially constant. The free electrons give rise to a surface plasmon absorption band on the surface of metal particles, which depends on both the particle size and dielectric medium/surroundings, which in this case is that of SiO_2 nanospheres. We observed that the short circuit current density increases with the incorporation of plasmonic layers and this is a primal optical effect attributed to the localized surface plasmon resonance. SiO_2 NPs/nanospheres could help avoid agglomeration of metallic NPs in the vicinity of the device as the FF improves from 0.50 up to 0.55 upon incorporation of $Ag@SiO_2$, and

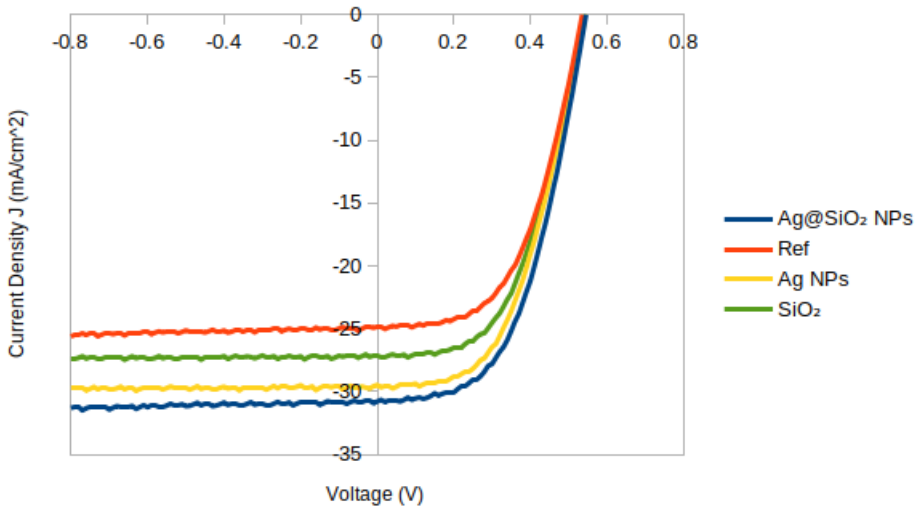


Figure 4.19: The *J-V* curve of a commercial *a-Si* solar cell incorporated with *Ag NPs*, SiO_2 and $Ag@SiO_2$ core-shell *NPs*.

ensured the *Ag NPs* takes full advantage of *LSPR* and light scattering. Accordingly, the device's *PCE* performance improved significantly with the incorporation of SiO_2 *NPs*, *Ag NPs* and $Ag@SiO_2$ core–shell *NPs* in the *a-Si* solar cell respectively, this is attributed to the change in the dielectric layer. This is shown by the *J-V* curve in Figure 4.19.

The reference *a-Si* solar cell initially had a short circuit current density, J_{sc} of 24.74 mA/cm^2 (from Table 4.2). Figure 4.19 and table 4.2 shows that the J_{sc}, *FF* and *PCE* of the solar cells increases as we introduce external plasmonic layers in the commercial *a-Si* solar cell. Meanwhile, the cell with $Ag@SiO_2$ core-shell *NPs* have the most improved J_{sc}, which increased to 32.47 mA/cm^2, giving a *PCE* improvement of approximately 8.34%. The enhancement in photo-conversion efficiency is indicative of increased optical absorption in the *a-Si* active layer through a plasmonic near field effect. Along with the increase in J_{sc}, the V_{oc} and *FF* each improved as well. The reference *a-Si* solar cell exhibited a *PCE* of 6.73%, then increased to 7.24 % after adding external layer of SiO_2 *NPs* on the top surface of the commercial *a-Si* solar cells. The introduction of external layer consisting of *Ag NPs* on the top surface of a commercial *a-Si* solar cells, gives a *PCE* improvement of up to 8.23% due to surface plasmon resonance. Coating the metallic *NPs* reduces transmission losses as well reflection losses on the device giving more

photons to be absorbed. The increase in *PCE* is also attributed to the preferential light scattering into the active layer of the substrate by the *LSPR* effect of the *Ag NPs*.

The series resistance and the shunt resistance are two parasitic resistances that have negative impact on the performance of a solar cell. By dissipating power through parasitic resistances, the series resistance lowers the *PCE* of solar cells. The inverse slope near V_{OC} and J_{SC} is used to calculate the shunt and series resistances.

The resistance values of an *a-Si* solar cell with decoupled series and shunt resistances are shown in Table 4.2. Because the series resistance is determined by the conductivity of the donor and acceptor layers and mobility has an impact on the series resistance. Furthermore, the addition of *Ag NPs*, SiO_2 *NPs* and $Ag@SiO_2$ core-shell *NPs* has no discernible effect on the series resistance, implying that *Ag NPs*, SiO_2 *NPs* and $Ag@SiO_2$ core-shell *NPs* did not generate space charges. Shunt resistance, on the other hand, is affected by charge carrier recombination at the donor/acceptor contact.

Shunt resistance is one order of magnitude more than series resistance. The $(1 + R_S/R_{SH})$ ratio can be used to calculate the losses for different R_S values. The shunt resistance rises as the concentration of *Ag NPs* droplets rises, while the open circuit voltage remains constant. As a result, the plasmonic effect may be solely responsible for the improvement in photogenerated current.

Higher shunt resistance values could be due to recombination losses. The V_{OC} level remains relatively constant, showing that the presence of *Ag NPs*, TiO_2 *NPs* and $Ag@SiO_2$ core-shell *NPs* has minor effect on the electrical structure of the bulk heteroactive junctions.

Table 4.2: Parameters calculated from *J-V* curve a commercial *a-Si* solar cells

Devices	$\mathbf{V}_{oc}$ **(V)**	$\mathbf{J}_{sc}$ (mA/cm^2)	**FF**	**PCE**	$\mathbf{R}_s$ (Ωcm^2)	$\mathbf{R}_{sh}$ (Ωcm^2)
Reference	0.54±0.02	24.74±2.3	0.51±0.01	6.73±0.51	7.13±0.51	250±4.8
Ag NPs	0.54± 0.02	29.47 ± 2.0	0.53±0.01	8.23± 0.51	7.13±0.40	172.41±5.2
SiO_2 *NPs*	0.54±0.02	27.35±2.4	0.49 ±0.02	7.24±0.52	7.67±0.51	424.78±5.4
$Ag@SiO_2$ *NPs*	0.55± 0.02	32.4 ± 2.0	0.50 ± 0.02	8.34 ± 0.51	7.13 ± 0.49	436.97 ± 5.2

4.6.3 The *J–V* characteristics *Ag NPs*, TiO_2 *NPs* and $Ag@TiO_2$ core-shell *NPs* on *a-Si* solar cell

Figure 4.20 shows the *J-V* curve of *Ag NPs*, TiO_2 *NPs* and $Ag@TiO_2$ core–shell *NPs* incorporated on the top surface of the *a-Si* solar cell. It is observed from Figure 4.20 that as the *Ag NPs*, TiO_2 and $Ag@TiO_2$ core-shells *NPs* as are added on the device there's a notable improvement on the current density.

Table 4.3 shows the short circuit current density, fill factor, open circuit voltage and photo-conversion efficiency (*PCE*) of the commercial *a-Si* solar cells incorporated with *Ag NPs*, TiO_2 nanospheres and $Ag@TiO_2$ core-shell *NPs* as extracted from Figure 4.20. The TiO_2 *NPs* layer promotes scattering of light on the device, and using TiO_2 *NPs* as shells, would reduce agglomeration at the surface or in the vicinity of *Ag NPs* and also ensures that the *Ag NPs* take full advantage of *LSPR* through light forward scattering. Accordingly, the *PV* performance of the *a-Si* solar cell incorporated with *Ag NPs* and TiO_2 *NPs* dielectric layer improved substantially as shown by the *J-V* curve in Figure 4.20.

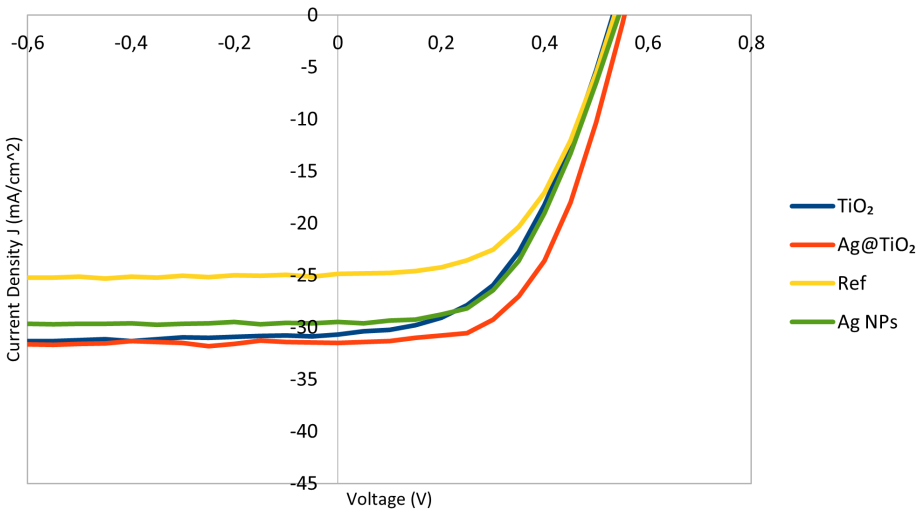


Figure 4.20: The *J-V* curve of a commercial *a-Si* solar incorporated with *Ag NPs*, $Ag@TiO_2$ and TiO_2 core-shell *NPs*

The J_{sc}, *FF* and *PCE* of the *a-Si* solar cell improved significantly upon incorporation of the plasmonic *NPs*. Also in this case, the *a-Si* solar cell incorporated with $Ag@TiO_2$ core-shell *NPs* has the highest J_{sc} of 32.85 mA/cm^2. Giving the most improved *PCE* of 9.86%, thus indicating enhanced incident light absorption in the *a-Si* layer when incorporated with $Ag@TiO_2$ core-shell *NPs*. *FF* of each devices improved very well. The reference *a-Si* solar cells exhibited a *PCE* of 6.73%, which increased the *PCE* to 8.43% after adding layers of TiO_2 *NPs* to the top front of the *a-Si* solar cell. After adding a layer of *Ag NPs* on the commercial *a-Si* solar cell there was *PCE* improvement of 8.23%. The increase in *PCE* was again attributed to the preferential light scattering into the device through *LSPR* effect of the *Ag NPs*.

The addition of *Ag NPs*, TiO_2 *NPs* and $Ag@SiO_2$ core-shell *NPs* also has no discernible effect on the series resistance, implying that there are minor space charges generation as the R_s values are relatively low. The shunt resistance, on the other hand, is affected by charge carrier recombination at the donor/acceptor contact. Then again the shunt resistance is one order of magnitude more than series resistance as seen in Table 4.3. Recombination losses could account for the higher shunt resistance values. The V_{OC} level remains rather constant, indicating that the electrical structure of the bulk heteroactive junction's is unaffected by the inclusion of *Ag NPs*, TiO_2 *NPs* and $Ag@SiO_2$ core-shell *NPs*.

Table 4.3: Parameters calculated from *J-V* curve from the enhanced commercial *a-Si* solar cells.

Devices	$\mathbf{V}_{oc}$ **(V)**	$\mathbf{J}_{sc}$ (mA/cm^2)	**FF**	**PCE**	$\mathbf{R}_s$ (Ωcm^2)	$\mathbf{R}_{sh}$ (Ωcm^2)
Reference	0.54±0.02	24.74±2.3	0.51±0.01	6.73±0.51	7.13±0.51	250±4.8
Ag NPs	0.54±0.02	29.47±2.0	0.53±0.01	8.23±0.51	7.13±0.40	172.41±5.2
TiO_2 *NPs*	0.54±0.02	30.68±2.0	0.5±0.01	8.43 ± 0.50	6.06 ± 0.50	154.44 ± 5.0
$Ag@TiO_2$ *NPs*	0.55±0.02	32.85±2.1	0.55±0.01	9.86±0.51	5.84±0.48	310.08±5.1

4.6.4 Dark current *I–V* characteristics

Under dark conditions, the current–voltage characteristics of a *p-n* junction solar cell with parasitic resistances at forward bias are given by

$$I = I_o[e^{\frac{q}{nkT}(V+IR_s)} - 1] + \frac{V - IR_s}{R_{sh}} \tag{4.11}$$

Where R_s is the series resistance responsible for ohmic losses because of the bulk resistance on the semiconductor material and the metallic contacts. Current leakages across the *p-n* junction are represented by the shunt resistance R_{sh}. The ideality factor n gives information about the quality of the junction, and saturation current I_o is associated with the properties of the semiconductor material given by the following expression

$$I_o = qAn_i^2\{\frac{D_nF_p}{L_nN_A} + \frac{D_pF_n}{L_pN_D}\} \tag{4.12}$$

where D_n and D_p are the diffusion coefficients of electrons and holes, respectively, which are dependent on charge carriers mobility through the semiconductor material. N_A and N_D are the acceptors and donors densities, q is the electron charge, A is the area of the cell and n_i is the intrinsic carrier concentration. The finite recombination velocity of electrons F_n and of holes F_p, which are for the front and back surfaces of the solar cell depending on the physical and chemical states of the surfaces. It is highly affected by the influence of heavy doping and on injection carriers [160]. The diffusion lengths L_n and L_p affect the saturation current of the *p-n* junction such that they should be long enough to guarantee that the generated carriers reach the contact areas of the solar cell before they recombine [161, 48].

The performance of the cell improves if the minority carrier diffusion length in the base region of the cell is greater than the thickness of the base [48]. R_s is typically taken to be the inverse slope of the dark current around J (0 mW/cm^2, 1.5 V) and R_{sh} is the inverse slope around J(0 mW/cm^2, 0 V)

4.6.4.1 Results and Discussions

For this study the *I-V*, the same samples used in previous section were also used in this study but measurement were under no illumination of light. Figure 4.21 shows the Semi-Log dark current of a commercial *a-Si* solar incorporated with *Ag NPs*, SiO_2 *NPs* and $Ag@SiO_2$ core-shell *NPs*.

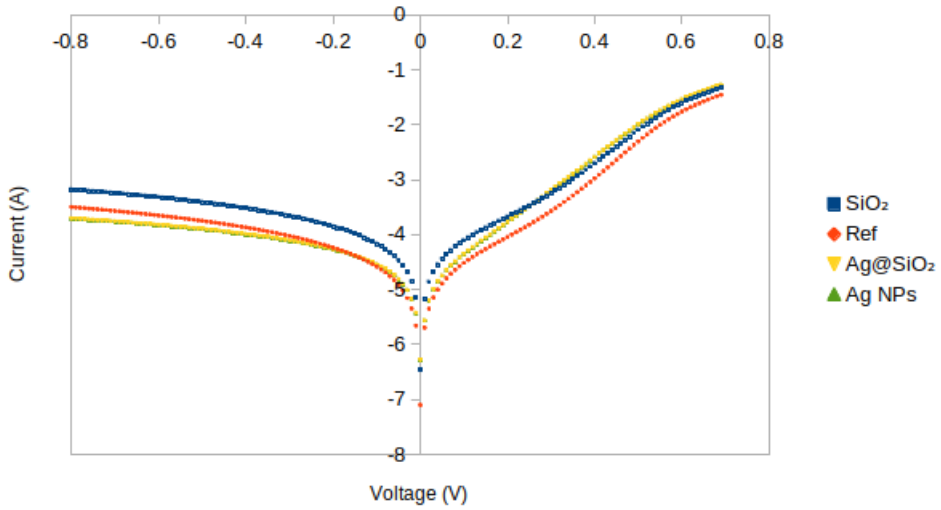


Figure 4.21: Semi-Log dark current of a commercial *a-Si* solar incorporated with *Ag NPs*, SiO_2 *NPs* and $Ag@SiO_2$ core-shell *NPs*.

From Figure 4.21, it is evident that the reference solar cell has the highest leakage current followed by the solar cell incorporated by SiO_2 *NPs*, *Ag NPs* and $Ag@SiO_2$ core-shell *NPs* respectively. The same trend is also observed with R_{sh}, where the device incorporated with $Ag@SiO_2$ core-shell *NPs* has the highest R_{sh} followed by SiO_2 *NPs*, $Ag@SiO_2$ core-shell *NPs* and *Ag NPs* respectively.

It also evident that the solar cell incorporated with with $Ag@TiO_2$ core-shell has the least current leakage as shown in Figure 4.22 and the highest R_{sh}, followed by TiO_2 *NPs*, *Ag NPs* respectively as shown in Table 4.4. There is large variation in the leakage current observed, which may dependent on the film thickness, electrode inter-layers, and film deposition techniques [162, 163].

For the system incorporated with *Ag NPs*, SiO_2 *NPs*, TiO_2 *NPs*, $Ag@SiO_2$, and

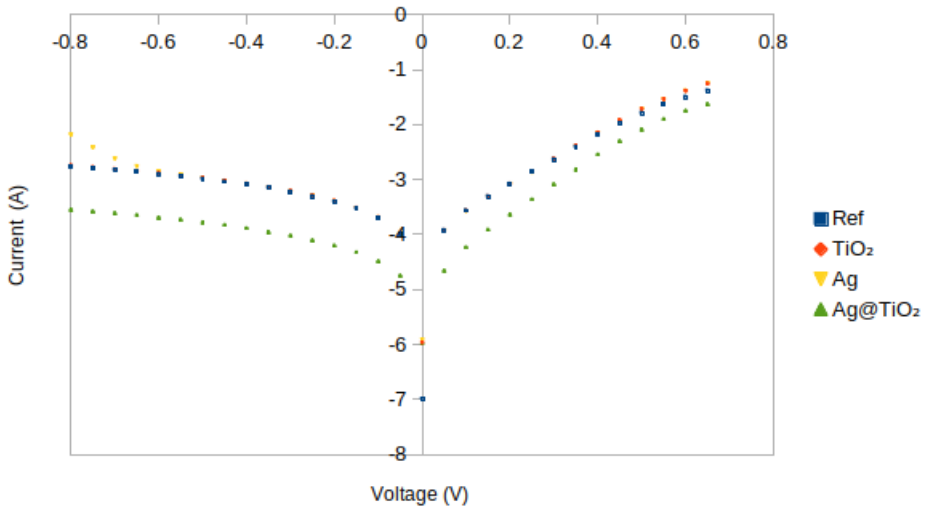


Figure 4.22: Semi-Log dark current flowing in a commercial *a-Si* solar incorporated with Ag *NPs*, TiO_2 *NPs* and $Ag@TiO_2$ core-shell *NPs*.

$Ag@TiO_2$ core-shell *NPs*, there are relatively low R_s values observed (see Table 4.4). The Ag *NPs*, SiO_2 *NPs*, TiO_2 *NPs*, $Ag@SiO_2$, and $Ag@TiO_2$ core-shell *NPs* incorporated in *a-Si* solar cell have low shunt resistance respectively, indicating high leakage of current. The key contributor to the dark current is a strong leakage current through the junction. Note that the slope of the logarithmic dependence of the V_{oc} on light intensity is especially sensitive to the effect of leakage currents, varying from 4 kT/q to 6 kT/q depending on the shunt resistance for solar cells with different core-shell *NPs*.

Table 4.4: Parameters calculated from Semi-Log dark current of the enhanced commercial *a-Si* solar cells.

***a-Si* solar cell**	J_o (Acm^{-2})	$\mathbf{V}_{oc}$ **slope (kT/q)**	$\mathbf{R}_s$ (Ωcm^2)	$\mathbf{R}_{sh}$ (Ωcm^2)
Reference	1.03E-07	4.4 ± 0.02	7.13 ± 0.51	250 ± 4.8
SiO_2 *NPs*	7.96E-08	5.3 ± 0.02	7.67 ± 0.051	424.78 ± 5.4
TiO_2 *NPs*	1.09E-06	5.5 ± 0.02	6.06 ± 0.50	154.44 ± 5.0
Ag NPs	1.19E-06	5.5 ± 0.02	7.13 ± 0.40	172.41 ± 5.2
$Ag@SiO_2$ *NPs*	5.24E-07	5.18 ± 0.02	7.13 ± 0.49	436.97 ± 5.2
$Ag@TiO_2$ *NPs*	1.08E-06	5.84 ± 0.02	5.84 ± 0.48	310.08 ± 5.1

4.7 Conclusion

This chapter presented a systematic study of metallic nanoparticles such *Au/Ag NPs*. Silica and Titania core-shell *NPs* were successfully synthesized through sol-gel methods which includes the Stöber method. The silica/titania core-shell*NPs* on its own had a resonance at 530 and 650 *nm* respectively. Even when the size of the core-shell *NPs* was increased, the plasmonic resonance remained the same, with an increased absorption intensity. Silica/Titania core-shell *NPs* with *Au/Ag NPs* were studied and they showed an improvement in absorption intensity. The plasmon resonance of the $Ag@SiO_2$ and $Au@SiO_2$ core–shells were blue shifted, respectively. The morphological studies revealed the a spherical shape with varying sizes from 35 *nm* up to 85 *nm NPs*.

A systematic study of multi-functional layers of *Ag NPs*, SiO_2 *NPs*, TiO_2 *NPs*, $Ag@SiO_2$ core-shell *NPs* and $Ag@TiO_2$ core-shell *NPs* in a commercial *a-Si* solar cell was carried out and the *PV* properties of the cells were improved. The results indicated that the light absorption of the *a-Si* solar cell, and the *PCE* of all devices improved significantly because of the plasmonic effects. As a result, *a-Si* solar cell with $Ag@TiO_2$ core-shell *NPs* had a higher efficiency (9.86%) compared to the ones incorporated with other *NPs*. The other improved *PCE* are as follows: $Ag@SiO_2$ core-shell *NPs*: 8.83%, TiO_2 *NPs*: 8.43%, SiO_2 *NPs*: 7.24%, *Ag NPs*: 8.23% and pristine *a-Si* solar cell:6.73%. This represents potential access for improving the *PCE* of *a-Si* solar cell or any kind of a solar cell. The enhancement of J_{SC} and *PCE* is attributed to a combination of three factors: improved electron transport properties through *Ag NPs*, improved light absorption caused by *LSPR*, and intensified light-scattering or absorption of *Ag NPs*.

The relatively low R_s values (seen in Table 4.4) obtained for *Ag NPs*, SiO_2, TiO_2, $Ag@SiO_2$ and $Ag@TiO_2$ core-shell *NPs* suggested that the current losses are there, hence producing steeper slope in natural log graph of current. The solar cell samples have relatively high shunt resistance, indicating high leakage current across the junction, which is the main contributor to the dark current. The slope of the logarithmic

dependence of the V_{oc} on light intensity is particularly sensitive to the effect of leakage currents with slopes ranging from 4 kT/q to 6 kT/q for the solar cell with different core-shell *NPs* depending on the shunt resistance.

Chapter 5

PV Devices with Silica Titania Waveguides

5.1 Introduction

The Resonant Waveguide Grating (*RWG*) is a waveguide grating structure which enhances the resonant field and elongates the propagation path for light within the solar cell material. The grating layer, as a phase matching element, brings the incoming light into multiple resonances in the device, eventually increasing the probability of light absorption due to enhancement in propagation length. The *RWG* consists of a single high refractive index dielectric layer on a periodically corrugated transparent substrate to couple light and to enhance light absorption. Therefore *RWG* structures have attracted much attention in the past two decades [164, 165]. The periodic binary grating structures which allow incoming light to couple to various modes in the waveguide layer and ultimately confine light in the active region of the cell [166]. The coloration that is emerging is a type of structural coloration is through periodic binary grating structures. The wave (light) incident angle to the diffraction grating, the spacing or distance between consecutive diffracting elements (e.g., parallel slits for a transmission grating), and the wavelength of the incident light all influence the orientations or diffraction angles of these beams [167, 168].

Since resonant light coupling in waveguide is only possible in small spectral regions compared to the broad solar spectrum, an engineered light-trapping design to address the

whole spectrum efficiently is necessary. Various periodic light trapping textures have demonstrated strong enhancement of the external quantum efficiency (*EQE*) of solar cells in a spectrally sharp resonances [169, 170]. In contrast, solar cells with random textures show a spectrally broad improvement of *EQE* [170, 97].

This chapter demonstrates the improvement of the photovoltaic performance of a thin film solar cell with a thickness far below the optical absorption length α^{-1} when operated in-conjunction with an optical waveguide [171].

5.2 Resonant Waveguide Gratings *(RWGs)*

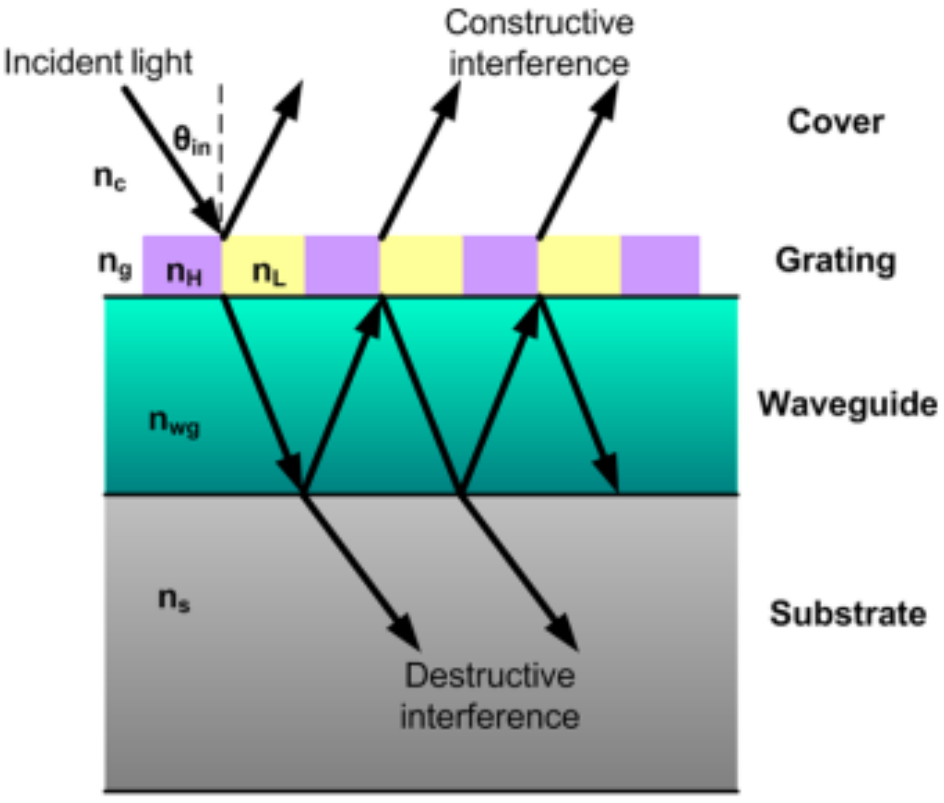


Figure 5.1: Schematic *RWG* coupling at resonance from the model provided by Rosenblatt et al [172]

Building suitable photonic nanostructures like a waveguide film, light from the sun may be readily trapped within the solar cell, reducing the losses of reflection and

scattering of light on the solar cell's surface [173].

The incident wave couples through a grating into the resonant waveguide-grating structure. Where resonance is likely to occur when one of the diffracted waves phase matches a leaky waveguide mode accepted by the waveguide structure, as schematically shown in Figure 5.1.

Thus *RWG* grating structure is basically a phase matching element which permits the incident light to undergo more than one resonances to enhance the opportunity of mild confinement of light in the material [174, 175]. The resonance wavelength is dependent on the phase matching element of the grating layer [172]. The effective mode propagation constant ϕ for the disappearing diffracted wave at the phase matching is given by [176, 172].

$$\phi_i = k_o(n_c sin\theta_i - i\frac{\lambda}{d}) \tag{5.1}$$

where $k_o = 2\pi/\lambda$ is the wave vector of a free space, λ is the wavelength of light in vacuum, n_c is the refractive index of air, θ_1 is the incident angle and d is the grating period. At resonance, the transmitted and reflected waves appears to have two coherent components called the Fresnel transmission/reflection [177]. The resonance wavelength is dependent on the grating parameters such as grating period, grating height, structural line-width and the refractive indices of materials and surroundings [175, 178]. Resonant Waveguide Gratings (*RWG*) are known to be sensitive to polarization state of incident light [179].

To increase the photon density in the absorber, optical approaches have received a lot of attention. In *Si* solar cells, surface texturing has been employed to produce light trapping, but in dye-sensitized solar cells, light scattering on micro- or nano-particle clusters has been used to improve the optical pathway across the active portion of the cell [171, 180]. Increased photon densities have been seen in polymer solar cells due to interference [181], and thin dielectric coatings have been proposed to improve the optical field intensity distribution around the charge separation interface[182] In thin silicon on

insulator *(SOI)* waveguides covered with a layer of metal islands with widths in the tens of nanometers, strong absorption enhancement has been recorded [182, 183]. The coupling between metal island resonances and waveguide modes supported by the *(SOI)* structure was shown to be the cause of the absorption amplification [184]. Metal island-covered thin film and wafer-based silicon solar cells [185], as well as a hydrogenated amorphous silicon waveguide slab sandwiched between a periodic array of *Au* nanowires and an *Au* substrate, have been reported to have surface plasmon enhanced absorption [186]. Novel cell designs have also been developed for thin film solar cells to enable effective light trapping [187].

For this research work, the aim is to study the increase in light absorption of a commercial *a-Si* solar cell using *RWG* concepts. A simple solar cell is a planar structure where most of the light is reflected and scattered from the surface of solar cell, which is subsequently a loss within the efficiency of cell [66]. The *RWG* structure are able to reduce scattering and reflecting losses through light confinement by *RWG* structures [188]. This leads to efficiency enhancement by increasing the optical absorption of the device [166].

5.3 Sample Preparation

SiO_2, TiO_2 and $SiO_2 : TiO_2$ waveguides were synthesized through a modified Stober method detailed bellow.

5.3.1 Synthesis of SiO_2 waveguides

The modified Stöber method was again useful in the synthesis of waveguides, SiO_2 waveguides were synthesized via sol-gel technique by introducing *HCl* as a catalyst. 30 *ml* of *TEOS* was mixed with 60 *ml* of dionized water and 60 *ml* of ethanol while stirring and 5 drops of *HCl* was added. The solution was allowed to stir for an hour at 70 $^{\circ}C$.

It was allowed to cool at room temperature whilst further stirring for 24 hours. Then it was deposited on a clean glass and amorphous silicon (*a-Si*) commercial solar cell with different layers by dip coating. After coating, the samples were sintered at 200 $^{\circ}C$ for 2 hours.

1. The solution was allowed to cool at room temperature then dip coated under the following condition for every iteration:
   (a) V_{up} = 25 mm/min
   (b) V_{dowm} = 25 mm/ min
   (c) Dip time = 6 sec
   (d) Distance = 150 mm

5.3.2 Synthesis of TiO_2 waveguides

In a separate container, Titanium tetraisopropoxide was mixed with water and ethanol using the measurement as in section 5.3.1 and it was allowed to react for 90 min. TiO_2 waveguide were synthesized by introducing a *HCl* as acid. This was achieved under the same condition in section 5.3.1.

5.3.3 Synthesis of SiO_2:TiO_2 waveguides

Silica-titania waveguides were prepared by the sol–gel technique. Titanium tetraisopropoxide (*TTIT*) and tetraethylorthosilicate (*TEOS*) were used as precursors of titania and silica, respectively as mentioned above. The ratio of total precursor (*TTIT* + *TEOS*) to water, *HCl* and ethanol, ([*TEOT* + *TEOS*]: H_2O: *HCl: Et–OH* = 1: 4: 0.2: 1), respectively.Note that the hydrolysis rate of Tetraethyl orthotitanate is slower than that of *TEOS*. Therefore, *TEOS* was hydrolyzed in the first step with the pre-mixed water solution, which contains hydrochloric acid and ethanol. After the two precursors were added in the pre-mixed solution, it was mixed for 24 hours to obtain silica–titania sol at room temperature and heated at 80 $^{\circ}C$ for 5 h then dip coated under the condition mentioned

above section 4.4. The solution was dried in the oven at 100 $^{\circ}C$ for 24 h and sintered at 500 $^{\circ}C$ for 1 hour on a hot plate (open space).

5.4 Optical Properties Analysis

Thin films of TiO_2, SiO_2 and $SiO_2 : TiO_2$ composite were prepared by the sol-gel method, using tetraethylorthosilicate (TEOS) and titanium tetraisopropoxide (TTIP) as precursors. Optical properties of the films were characterized by the ultraviolet-visible spectrophotometry. The refractive index of the waveguide films was calculated from the film thickness.

5.4.1 Transmittance of the *WG*

Figure 5.2 shows that the transmittance of silica waveguides that were dip coated at speed of 25 *mm/min* and sintered and activated at 500 $^{\circ}C$ and 200 $^{\circ}C$ for 1 minute and 2 hours, respectively. All the silica waveguides have a transmittance wavelength at about 450 *nm*, which then gives a calculated refractive index of 1.4731. It should be noted that the time and speed at which the waveguides were prepared and deposited have a great impact on the quality of the waveguides.

As shown in Figure 5.2, the transmittance of SiO_2 dielectric layer or waveguides that were thermal treated after all layers were deposited, showing a 55% transmittance at 458 *nm* for a single layer waveguide and 45% transmittance obseverd at 450 *nm* for the waveguide with 4 layers. Then it was noted for a 2 layered waveguide the transmittance was at about 38% at 460 *nm*. This finding suggests that the single layer of SiO_2 dielectric is more transmitting than absorbing of incident light and this might be due to the inhomogeneity in the film thickness.

Figure 5.3 displays the transmittance of silica:titania waveguides dip coated then sintered in air at 500 $^{\circ}C$ after depositing layers and were marked as follows:

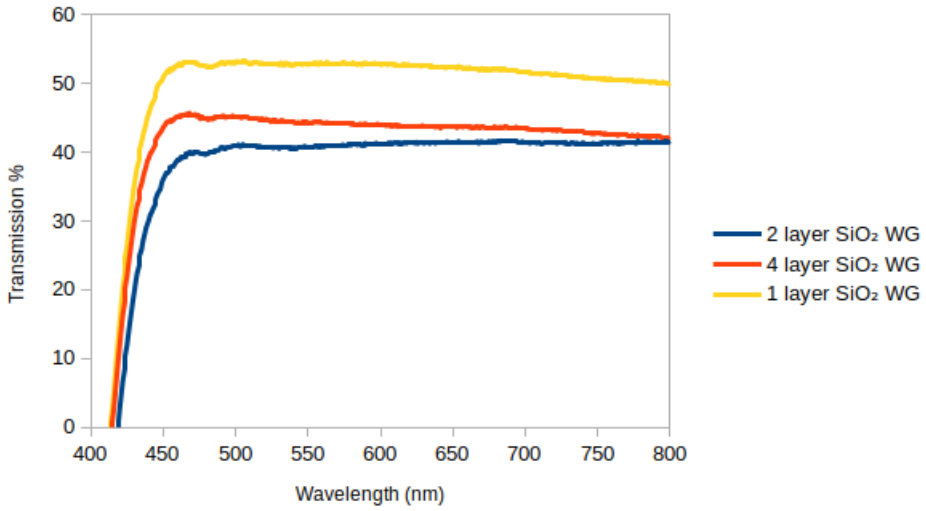
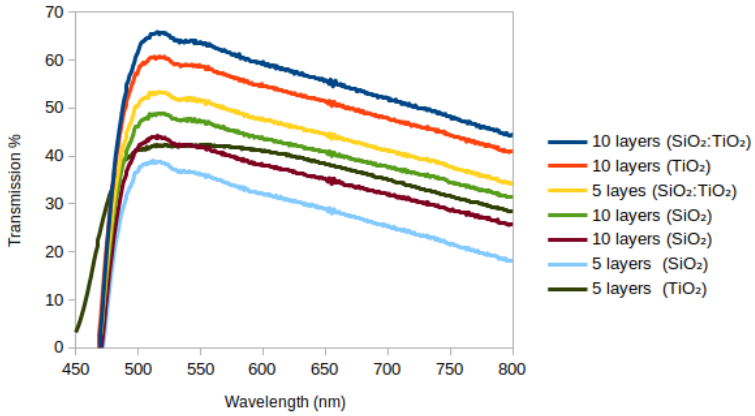


Figure 5.2: Transmission spectra of silica waveguides with different number of layers dip coated on a microscope glass slab, that were thermal treated after a layer or all layers were deposited.

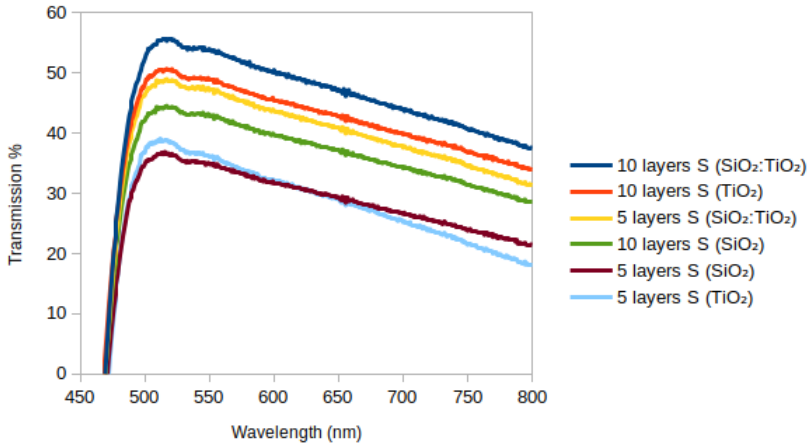
1. After dip coating a given number of layers (e.g 5 layers), the sample was then sintered at 500 $^{\circ}C$: labelled by the number of layers then the sample name: e.g 5 layers $SiO_2 : TiO_2$,
2. After dip coating every single layer, the sample was sintered at 500 $^{\circ}C$: labelled by the number of layers, then marked by the letter S and then the sample name: e.g 5 S layers $SiO_2 : TiO_2$.

Figure 5.3 shows the transmittance of titania (TiO_2), silica (SiO_2) and silica:titania ($SiO_2 : TiO_2$) waveguides. Figure 5.3a shows the transmittance of SiO_2, TiO_2 and $SiO_2 : TiO_2$ waveguides, where all the given layers were dip coated first then sintered at 500 $^{\circ}C$, transmittance improves as the number of layers were added and it is also observed that the titania waveguides transmit light better than the silica waveguides. It is also noted that the $SiO_2 : TiO_2$ waveguides have transmittance of about 57%, making them the best waveguide in our study. The TiO_2-coated silica waveguides have spectra that are qualitatively similar in both cases.

From Figure 5.3b the transmittance of SiO_2 waveguides which were sintered after the deposition of every or single layer is much lesser when compared with the ones from



(a) Sintering after depositing all the layers



(b) Sintering after depositing each layer

Figure 5.3: The transmission spectra of SiO_2, TiO_2 and $SiO_2 : TiO_2$ waveguides.

Figure 5.3a this may be attributed to the exposure of air when sintering could have lead to cracks on the film. Note that SiO_2, TiO_2 and $SiO_2 : TiO_2$ waveguides display a similar transmittance wavelength at 510 nm.

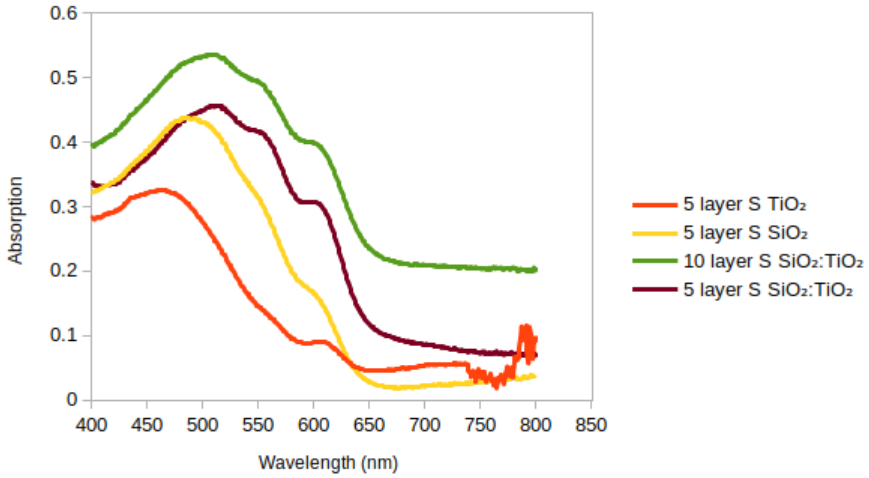
However, SiO_2-rich films possess higher ultraviolet$-$visible transmittance than the TiO_2-rich films. The modification of microstructure and chemical bonding configuration in the $SiO_2\check{}TiO_2$ films by the composition and its influence on the optical properties are discussed.

5.4.2 Absorption of the *WG*

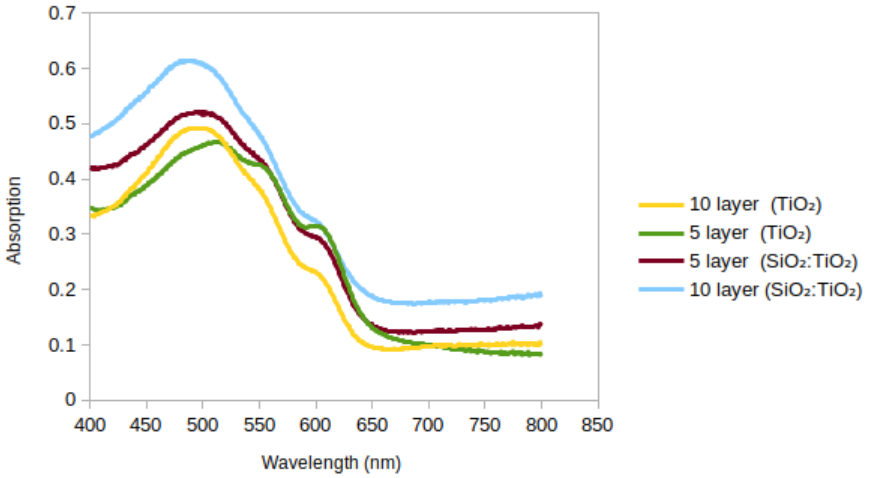
Figure 5.4 shows the absorption spectra of TiO_2, SiO_2 and $SiO_2 : TiO_2$ waveguides, where multi-absorption peaks are observed, with the main absorption peak at around 470 *nm*. The similarity of absorption profiles leads us to believe that ethylene adsorbed on TiO_2, SiO_2 and $SiO_2 : TiO_2$ waveguides has a spatial orientation [189]. Figure 5.4a shows the waveguides that were sintered after depositing each layer, a blue shift is noted as the number of layers are added for all the waveguides under study. Figure 5.4a consist of a dominant higher energy peak at 470 *nm* going up 530 *nm* as the film thickness increases and it also consist of a weaker lower energy peak or shoulder, at 600 to 620 *nm*. This could be attributed to the chemical composition and film structure of the waveguides.

Figure 5.4b shows the absorption spectra of TiO_2, SiO_2 and $SiO_2 : TiO_2$ waveguides that were sintered after depositing layers (e.g. 5 or 10 layers). It is also noted that the absorption intensity increases as layers are added. A blue is shift is noted as well, resulting from the increased film thickness of the waveguides. It can be concluded that the waveguides that were sintered after depositing all the given number of layers had a better absorption intensity than the ones that were sintered after depositing every single layer.

We showed a multilayer attenuated waveguide with a periodic stack of two dielectric materials. In the periodic stack of two dielectric materials, numerous absorption peaks coming from multiple *WG* are formed. By carefully selecting the structural characteristics, the number of absorption peaks corresponds to the stacked two dielectric materials. Due to the interaction of *WG*, perfect absorption can be accomplished by increasing the stacked period number of two dielectric materials [190].



(a) Sintering after depositing every layer



(b) Sintering after depositing all the layers

Figure 5.4: The absorption spectra of SiO_2, TiO_2 and $SiO_2 : TiO_2$ waveguides.

5.4.3 The refractive index

From the measured transmittance (T) the absorption coefficient (α), reflectance (R) and refractive index (n) were calculated using the following formulas [156]:

$$\alpha = \frac{2.303 log(1/T)}{t} \tag{5.2}$$

where t is the thickness of the sample. Note that

$$T = \frac{(1-R^2)e^{-(\alpha t)}}{1-Re^{-\alpha t}} \tag{5.3}$$

solving for R to obtain

$$R = \frac{e^{-\alpha t} + \sqrt{Te^{-\alpha t} - Te^{-3\alpha t} + T^2 e^{2\alpha t}}}{e^{-\alpha t} + Te^{-2\alpha t}} \tag{5.4}$$

and therefor the refractive index is

$$n = \frac{(R+1)+2\sqrt{R}}{R-1} \tag{5.5}$$

5.4.3.1 Thin film thickness (t) is measured through profilometer

A diamond stylus is moved vertically and laterally in contact with the sample for a defined distance in a contact profilometer. It measures minor variations in stylus displacement as a function of position with extreme precision. This method is a true direct measurement of the sample's surface height or thickness. The macroscopic glass slab thickness was measured to 1.1400×10^6 *nm*. A single layer wavaguide measured 1.14003×10^6 *nm*, a 5 layers wavaguides measured 1.14015×10^6 *nm* and a 10 layers wavaguides measured 1.14030×10^6 *nm*. Resulting in film thickness of 30 *nm* for a single layer, 150 *nm* for 5 layer waveguides and 300 *nm* for a 10 layer waveguides.

The calculated refractive index are given in Table 5.1. From Table 5.1, the absorption coefficient and refractive index were calculated. It is noted that the absorption coefficient and the refractive index for each waveguides differed due to the chemical composition during synthesis. The 150 *nm* thick waveguides with 5 layers have high refractive index as compared to the 300 *nm* thick waveguides with 10 layers for most of the samples. From this study, it is evident that as the films gets thicker, the refractive index decreases/reduces. The refractive index dispersion plays an important role in optical materials research.

Because the deposition temperature and pressure were kept constant in our work, the effective diffusivity of all the waveguides is most likely constant. Furthermore, the refractive index is found to be different for each wavguide, showing that the thickness of

the films fluctuates [191]. In comparison, deposition rate have a considerable impact on the optical characteristics of waveguide films, owing to a change in stoichiometry. Silca-titania waveguide films showed that the deposition techniques, compressively improved the absorption coefficient, which attributes to the densification of the films, with the significant change in the refractive index [192, 193].

Many figures of merit of optical components such as reflectors, filters, and resonators are determined by the refractive index, a fundamental quantity in optics and optoelectronics. A novel family of optical thin-film materials with a very low refractive index is were studied and presented a high-quality thin films with refractive indices as low as 1.65.

Table 5.1: The calculated refractive index

Waveguides	**Thickness** (nm)	**Transmission**	**Absorption Coefficient**	**Refractive index**
5 layer S SiO_2	150	0.36	$6.81 \times 10^6 \pm 0.03$	$2{,}5594 \pm 0.2$
10 layer S SiO_2	300	0.43	$2.81 \times 10^6 \pm 0.03$	$2{,}9105 \pm 0.2$
5 layer S TiO_2	150	0.38	$6.45 \times 10^6 \pm 0.03$	$2{,}6529 \pm 0.2$
10 layer S TiO_2	300	0.49	$4.75 \times 10^6 \pm 0.03$	$1{,}6507 \pm 0.2$
5 layer S $SiO_2 : TiO_2$	150	0.48	$4.89 \times 10^6 \pm 0.03$	$2{,}8202 \pm 0.2$
10 layer S $SiO_2 : TiO_2$	300	0.55	$3.99 \times 10^6 \pm 0.03$	$1{,}8709 \pm 0.2$

5.5 The *J–V* characterization for silica waveguides on *a-Si* solar cell

For this study only single layer silica waveguides were chosen, from Figure 5.2, the transmittance of a single SiO_2 dielectric layer or waveguides was the best and is at 55% at 458 *nm* compared to the other systems that were studied. It should be noted at the time of the study only SiO_2 dielectric layer were availability.

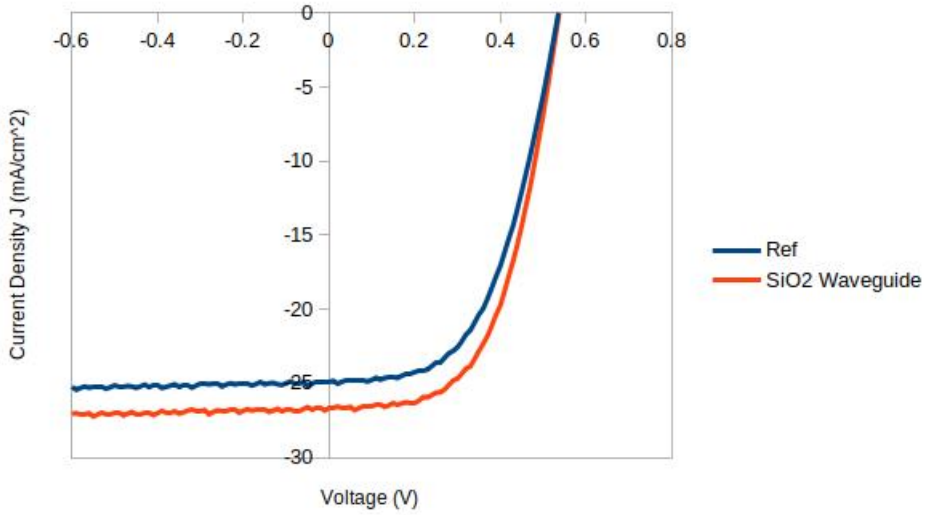


Figure 5.5: The *J-V* characteristics of commercial a-Si solar with silica waveguide

Figure 5.5 shows the *J-V* characteristics of *a-Si* solar cell illuminated under AM 1.5 with and without the silica waveguide deposited on the commercial *a-Si* solar cell. There is a notable increase in current density as waveguides are incorporated in *a-Si* solar cell, which improved from 24.74 mA/cm^2 up flow 27.10 mA/cm^2. It is also observed that the V_{OC} is 0.54 V for both devices is the same. In Table 4.3 there are parameters calculated from the *J-V* curves in Figure 5.5.

Table 5.2 illustrates that the *a-Si* solar cell in the presence of a waveguide has have an influence on the *PV* performance giving an improved photocurrent efficiency (*PCE*) of 7.63%, which is only a slight increase compared to the reference *a-Si* solar cell with the *PCE* of 6.73 %. We suspect this is due to the carrier recombination resulting in high

series resistance of 8.3 (Ωcm^2), after the SiO_2 waveguide was incorporated on the device and the *a-Si* solar cell contacts have came into ohmic contact. The SiO_2 dielectric layer influenced on short circuit current density going up to 27 mA/cm^2 (see table 5.2).

5.6 Conclusion

The SiO_2, TiO_2 and $SiO_2 : TiO_2$ waveguides were synthesized/prepared by using sol gel method and were deposited on microscopic glass slide through dip coating techniques. Transmission analysis was performed, where the transmission fluctuated as the number of the waveguides layers were added, having the lowest transmittance of 30% for a 5 layer SiO_2 waveguide up to the highest 55% for a 10 layer $SiO_2 : TiO_2$ waveguide. The waveguides showed transmission between 450 *nm* and 530 *nm*. The absorption of SiO_2, TiO_2 and $SiO_2 : TiO_2$ waveguides significantly improved respectively as the number of layers were added. Multi- absorption peaks were observed accompanied by red shift, due to the film thickness increment. Furthermore the absorption coefficient and refractive index were calculated.

Improvement in the optical absorption of silicon solar cells through waveguides were achieved by designing a hybrid structure of *a-Si* solar cell. The device was analyzed for the enhancement in optical absorption leading to an improvement of about 7,63% in solar spectrum range of 450-510 *nm* in comparison with the reference *a-Si* solar cell. Thus enhancement in optical absorption increases the conversion efficiency of light into electrical energy in solar cells.

It was illustrated that the SiO_2 waveguide's dielectric layer had a marginal influence on *PV* performance giving a photo current efficiency (*PCE*) of 7.63%, which has increased by 11.73% compared to the reference *a-Si* solar cell having a *PCE* of 6.73%. However, the SiO_2 dielectric layer influenced on *PV* short circuit current density up to 27.1 mA/cm^2 from 24.74 mA/cm^2 (table4.3).

The spectral response could be improved by systematically changing the design-

ing parameters and thus improving the performance of *PV* devices. As the V_{oc} did not change, the device structure and energy levels of each layer in the device did not change after incorporating waveguides layers. Additionally the leakage current remains fairly the same. Thus we observed a purely optical effect.

Table 5.2: Parameters calculated from *J-V* curve from the doped commercial *a-Si* solar cells.

***a-Si* solar cell**	$\mathbf{V}_{oc}$ **(v)**	$\mathbf{J}_{sc}$ (mA/cm^2)	**FF**	**PCE**	$\mathbf{R}_s$ (Ωcm^2)	$\mathbf{R}_{sh}$ (Ωcm^2)
Reference	0.54±0.02	24.74±2.3	0.51±0.01	6.73±0.51	7.13±0.51	250±4.8
SiO_2 WG	0.54±0.02	27.1±2.1	0.49±0.02	7.63±0.52	8.30±0.50	145±3.2

Chapter 6

Summary and Outlook

In this thesis, the utilization of plasmonic nanoparticles to enhance the efficiency of the photon absorption of solar cell or photovoltaic devices was described. We found that a solar cell's energy conversion efficiency is highly dependent on the light absorption coefficient within the material [194]. With the use of effective light-trapping techniques to boost the efficiency of a solar cell [195], the absorption coefficient can be largely increased. The incoming light from the sun can be easily confined inside the cell by correctly designing photonic nanostructures which reduces the losses of reflection and scattering of light on the surface of the cell [173, 178].

The *LSPR* effect had a great impact in enhancing the *PCE* of commercial *a-Si* solar cell, through plasmonic nanoparticles such as *Au and Ag*. The quasi-static approximation was used to elaborate the absorption and scattering of spherical nanoparticles and core–shell nanoparticles. The absorption and scattering cross-section of *Ag/Au NPs* was studied in under 2 distinct dielectric environmental. The simulations have shown strong dependence of plasmon resonance with varied sizes *NPs*. The $Ag/Au@SiO_2$ and $Ag/Au@TiO_2$ core-shell *NPs* absorption cross-sections showed an increase in the magnitude of the absorption as the shell size was increased (the core size was kept the same through out), where a red shifts was observed at different plasmon resonance. It was also found that absorption of light was dominating than scattering of light with the core-shell *NPs*. On the other hand the simulation of $Ag@TiO_2$ core–shells *NPs* revealed a huge red shift in plasmon resonance as the shell thickness of titania increased, which indicated that the dielectric medium of titania core-shell *NPs* is largely affected by the shell thickness. When the size of the cores were varied while the shell thickness was kept the

same, the red shifts were minimal for both $Ag/Au@SiO_2$ and $Ag/Au@TiO_2$ core-shell *NPs* and the absorption and scattering intensity for both core-shell *NPs* were nearly the same.

A systematic study of synthesizing metallic nanoparticles such as *Au/Ag NPs* was conducted through wet chemistry. Silica and Titania core-shell *NPs* were successfully synthesized through sol-gel methods which includes the Stöber method. Under UV-viz spectrum silica/titania core-shel *NPs* showed a resonance at around 530 and 650 *nm* respectively. As the size of the core-shell *NPs* increased, the plasmonic resonance remained at the same position, accompanied by an increased absorption intensity. Silica/Titania core-shell *NPs* with *Au/Ag NPs* were studied and they showed an improvement in absorption intensity. Blues shifts were also observed for the $Ag@SiO_2$ and $Au@SiO_2$ core–shells *NPs*.

Numerical and experimental methods, were both primarily based on the direct embedding of metal *NPs*, core-shells *NPs*, on the top front of the solar cell to increase photon collection in the solar cell. The photon absorption of the solar cell was increased by introducing *Ag/Au NPs*, SiO_2 *NPs*, TiO_2 *NPs*, $Ag@SiO_2$ core-shell *NPs* and $Ag@TiO_2$ core-shell *NPs* layers in the device. Each of these layers have its own unique absorption coefficient which then allowed us to do simulation solar cells and we were able to improve the photocurrent efficiency of a *c-Si* solar cell. It was obvious that due to the presence of the metallic *NPs*/core-shell *NPs* on the solar cell, more light is absorbed on the device, which attributes to creation of additional electron–hole pairs within the active layer of solar cells and therefore improved the current density [196]. The results predict the highest increase in *PCE* of 28.05% in a *c-Si* solar cell with $Ag@TiO_2$ core-shell *NPs*. Also there was an enhancement in *PCE* for *c-Si* solar cells incorporated with: ($Ag@SiO_2$ core-shell: 26.43%, TiO_2 nanospheres: 26.24%, SiO_2 nanospheres: 22.00%, *Ag NPs*: 24.46%).

Multi-functional layers of *Ag NPs*, SiO_2 *NPs*, TiO_2 *NPs*, $Ag@SiO_2$ core-shell *NPs* and $Ag@TiO_2$ core-shell *NPs* were deposited on a commercial *a-Si* solar cell and the *PV* properties of the cells were improved. The results indicated that the light absorption

range of the *a-Si* solar cell, and the *PCE* of all devices increased significantly because of the plasmonic effects. As a result, *a-Si* solar cell with $Ag@TiO_2$ core-shell *NPs* had a higher efficiency (9.86%) compared to $Ag@SiO_2$ core-shell *NPs*:with 8.84%, TiO_2 *NPs*: 8.43%, SiO_2 *NPs*: 7.24%, *Ag NPs*:with 8.23% and pristine *a-Si* solar cell:with 6.74%, which represents potential access for improving the *PCE* of *a-Si* solar cell or any kind of a solar cell. The enhancement of J_{SC} and *PCE* is attributed to a combination of three factors: improved electron transport properties of *Ag NPs*, improved light absorption caused by *LSPR*, and intensified light-scattering or absorption of *Ag NPs*. The solar cell samples also had relatively low shunt resistance, indicating high leakage current across the junction, which is the main contributor to the dark current [197].

Another improvement in the optical absorption of silicon solar cells through waveguides which were synthesized through sol-gel method. Absorption and transmission spectra were studied. The absorption spectra of TiO_2, SiO_2 and $SiO_2 : TiO_2$ waveguides showed that the wavegiudes that were sintered after deposing all the given number of layers, had a better absorption intensity than the ones that were sintered after depositing each individual layer. The absorption intensity increased as layers were added, a blue shift was noted as well. From the transmission spectra the same trend was observed and the transmittance was used to calculated the refractive index which varied according to the thickness of the waveguide.

As a result, increased light absorption through waveguides has a significant impact on various types of solar cells. It was illustrated that the SiO_2 waveguides increased the photocurrent efficiency (*PCE*) to 7.51% from 6.74%, which increased by 11.42% when compared to the reference a-Si solar cell.

Scope for future research

Several innovative concepts for improving the effective conversion of solar energy to electricity have been offered during the course of this study. These ideas range from introducing metallic *NPs*, core-shell *NPs* and waveguides directly deposited on the solar

cell to modify the solar cell's *PCE*. The following may be explored for future work:

- The study of other metallic *NPs* such as *Al*, *Fe* and *Cu* corresponding to the scattering and absorption mechanisms,
- Deposition of core-shell *NPs* in the active layer to see if it has an influence on *PCE*,
- Implementing the waveguides doped with rare earth ions into the active layer of the solar cell to facilitate quantum cutting up conversion processes,
- Study the core-shell *NPs* doped with rare-earth ions.

References

[1] R. Tsekov, P. Georgiev, S. Simeonova, and K. Balashev, "Quantifying the blue shift in the light absorption of small gold nanoparticles," *arXiv preprint arXiv:1702.04513*, 2017.

[2] G. Putrus, R. Kotter, Y. Wang, R. Das, E. Bentley, X. Dai, G. O'Brien, R. Heller, R. Prateek, R. Gough, *et al.*, "Overview seev4-city playing field," 2018.

[3] wikipedia the free encyclopedia, "Growth of photovoltaics." $https://en.wikipedia.org/wiki/Growth_of_photovoltaics$, Aug 2020.

[4] T. G. Allen, J. Bullock, X. Yang, A. Javey, and S. De Wolf, "Passivating contacts for crystalline silicon solar cells," *Nature Energy*, pp. 1–15, 2019.

[5] H. A. Atwater and A. Polman, "Plasmonics for improved photovoltaic devices," in *Materials for Sustainable Energy: A Collection of Peer-Reviewed Research and Review Articles from Nature Publishing Group*, pp. 1–11, World Scientific, 2011.

[6] K. J. Savage, M. M. Hawkeye, R. Esteban, A. G. Borisov, J. Aizpurua, and J. J. Baumberg, "Revealing the quantum regime in tunnelling plasmonics," *Nature*, vol. 491, no. 7425, pp. 574–577, 2012.

[7] V. E. Ferry, M. A. Verschuuren, M. C. v. Lare, R. E. Schropp, H. A. Atwater, and A. Polman, "Optimized spatial correlations for broadband light trapping nanopatterns in high efficiency ultrathin film a-si: H solar cells," *Nano letters*, vol. 11, no. 10, pp. 4239–4245, 2011.

[8] A. Polman, "Plasmonics applied," *Science*, vol. 322, no. 5903, pp. 868–869, 2008.

[9] G. S. Kinsey, P. Hebert, K. E. Barbour, D. D. Krut, H. L. Cotal, and R. A. Sherif, "Concentrator multijunction solar cell characteristics under variable intensity and

temperature," *Progress in Photovoltaics: Research and Applications*, vol. 16, no. 6, pp. 503–508, 2008.

[10] M. Born and E. Wolf, *Principles of optics: electromagnetic theory of propagation, interference and diffraction of light*. CUP Archive, 2000.

[11] T.-S. Deng and F. Marlow, "Synthesis of monodisperse polystyrene@ vinyl-sio2 core–shell particles and hollow sio2 spheres," *Chemistry of Materials*, vol. 24, no. 3, pp. 536–542, 2012.

[12] S. Li, *Silicon-based terahertz waveguides*. PhD thesis, 2015.

[13] X.-Q. Qi and J.-M. Liu, "Photonic microwave applications of the dynamics of semiconductor lasers," *Selected Topics in Quantum Electronics, IEEE Journal of*, vol. 17, no. 5, pp. 1198–1211, 2011.

[14] L. Schmidt-Mende, A. Fechtenkötter, K. Müllen, E. Moons, R. H. Friend, and J. MacKenzie, "Self-organized discotic liquid crystals for high-efficiency organic photovoltaics," *Science*, vol. 293, no. 5532, pp. 1119–1122, 2001.

[15] P. Karasiński, "Sensor properties of planar waveguide structures with grating couplers," *Opto-Electronics Review*, vol. 15, no. 3, pp. 168–178, 2007.

[16] U. Bach, D. Lupo, P. Comte, J. Moser, F. Weissörtel, J. Salbeck, H. Spreitzer, and M. Grätzel, "Solid-state dye-sensitized mesoporous tio2 solar cells with high photon-to-electron conversion efficiencies," *Nature*, vol. 395, no. 6702, pp. 583–585, 1998.

[17] Y. H. Kim, D. K. Lee, H. G. Cha, C. W. Kim, and Y. S. Kang, "Synthesis and characterization of antibacterial ag- sio2 nanocomposite," *The Journal of Physical Chemistry C*, vol. 111, no. 9, pp. 3629–3635, 2007.

[18] Z. Yu, A. Raman, and S. Fan, "Fundamental limit of nanophotonic light trapping in solar cells," *Proceedings of the National Academy of Sciences*, vol. 107, no. 41, pp. 17491–17496, 2010.

[19] S. Fay, J. Steinhauser, N. Oliveira, E. Vallat-Sauvain, and C. Ballif, "Opto-electronic properties of rough lp-cvd zno: B for use as tco in thin-film silicon solar cells," *Thin Solid Films*, vol. 515, no. 24, pp. 8558–8561, 2007.

[20] P. Karasiński, C. Tyszkiewicz, A. Maciaga, I. Kityk, and E. Gondek, "Two-component waveguide sio 2: Tio 2 films fabricated by sol–gel technology for optoelectronic applications," *Journal of Materials Science: Materials in Electronics*, vol. 26, no. 5, pp. 2733–2736, 2015.

[21] C. Chaudhari and D. Gautam, "Analysis of sio2/tio2–sio2/sio2 coupled parallel waveguide structures using computer aided design techniques," *Optics communications*, vol. 181, no. 1-3, pp. 61–69, 2000.

[22] G. K. Singh, A. L. Low, and Y. S. Yong, "Dip-coated hnr120 photoresists thin-film optical waveguides," *Optik-International Journal for Light and Electron Optics*, vol. 116, no. 3, pp. 107–110, 2005.

[23] R. Horvath, L. R. Lindvold, and N. B. Larsen, "Reverse-symmetry waveguides: theory and fabrication," *Applied Physics B*, vol. 74, no. 4-5, pp. 383–393, 2002.

[24] B. Michel, A. Bernard, A. Bietsch, E. Delamarche, M. Geissler, D. Juncker, H. Kind, J.-P. Renault, H. Rothuizen, H. Schmid, *et al.*, "Printing meets lithography: Soft approaches to high-resolution patterning," *IBM Journal of Research and Development*, vol. 45, no. 5, pp. 697–719, 2001.

[25] C.-H. Chou, J.-K. Chuang, and F.-C. Chen, "High-performance flexible waveguiding photovoltaics," *Scientific reports*, vol. 3, p. 2244, 2013.

[26] J. H. Karp, E. J. Tremblay, and J. E. Ford, "Planar micro-optic solar concentrator," *Optics express*, vol. 18, no. 2, pp. 1122–1133, 2010.

[27] P. P. Verbunt, S. Tsoi, M. G. Debije, D. J. Boer, C. W. Bastiaansen, C.-W. Lin, and D. K. de Boer, "Increased efficiency of luminescent solar concentrators after application of organic wavelength selective mirrors," *Optics express*, vol. 20, no. 105, pp. A655–A668, 2012.

[28] Y. Li, X. Zhang, Y. Zhang, R. Dong, and C. K. Luscombe, "Review on the role of polymers in luminescent solar concentrators," *Journal of Polymer Science Part A: Polymer Chemistry*, vol. 57, no. 3, pp. 201–215, 2019.

[29] L. H. Slooff, E. E. Bende, A. R. Burgers, T. Budel, M. Pravettoni, R. P. Kenny, E. D. Dunlop, and A. Büchtemann, "A luminescent solar concentrator with 7.1% power conversion efficiency," *physica status solidi (RRL)–Rapid Research Letters*, vol. 2, no. 6, pp. 257–259, 2008.

[30] H. Hernandez-Noyola, D. H. Potterveld, R. J. Holt, and S. B. Darling, "Optimizing luminescent solar concentrator design," *Energy & Environmental Science*, vol. 5, no. 2, pp. 5798–5802, 2012.

[31] S. F. Correia, P. P. Lima, E. Pecoraro, S. J. Ribeiro, P. S. André, R. A. Ferreira, and L. D. Carlos, "Scale up the collection area of luminescent solar concentrators towards metre-length flexible waveguiding photovoltaics," *Progress in Photovoltaics: Research and Applications*, vol. 24, no. 9, pp. 1178–1193, 2016.

[32] L. Desmet, A. Ras, D. De Boer, and M. Debije, "Monocrystalline silicon photovoltaic luminescent solar concentrator with 4.2% power conversion efficiency," *Optics Letters*, vol. 37, no. 15, pp. 3087–3089, 2012.

[33] A. R. Frias, M. A. Cardoso, A. Bastos, S. F. Correia, P. S. André, L. D. Carlos, V. de Zea Bermudez, and R. A. Ferreira, "Transparent luminescent solar concentrators using ln3+-based ionosilicas towards photovoltaic windows," *Energies*, vol. 12, no. 3, p. 451, 2019.

[34] M. J. Currie, J. K. Mapel, T. D. Heidel, S. Goffri, and M. A. Baldo, "High-efficiency organic solar concentrators for photovoltaics," *Science*, vol. 321, no. 5886, pp. 226–228, 2008.

[35] M. I Kabir, Z. Ibarahim, K. Sopian, and N. Amin, "A review on progress of amorphous and microcrystalline silicon thin-film solar cells," *Recent Patents on Elec-*

trical & Electronic Engineering (Formerly Recent Patents on Electrical Engineering), vol. 4, no. 1, pp. 50–62, 2011.

[36] K. Hara, T. Sato, R. Katoh, A. Furube, Y. Ohga, A. Shinpo, S. Suga, K. Sayama, H. Sugihara, and H. Arakawa, "Molecular design of coumarin dyes for efficient dye-sensitized solar cells," *The Journal of Physical Chemistry B*, vol. 107, no. 2, pp. 597–606, 2003.

[37] O. A. Abdulrazzaq, V. Saini, S. Bourdo, E. Dervishi, and A. S. Biris, "Organic solar cells: a review of materials, limitations, and possibilities for improvement," *Particulate science and technology*, vol. 31, no. 5, pp. 427–442, 2013.

[38] Q. Liu, Y. Jiang, K. Jin, J. Qin, J. Xu, W. Li, J. Xiong, J. Liu, Z. Xiao, K. Sun, S. Yang, X. Zhang, and L. Ding, "18cells," *Science Bulletin*, 01 2020.

[39] H. Ritchie, "Renewable energy," *Our World in Data*, 2017. https://ourworldindata.org/renewable-energy.

[40] A. Oliva-Chatelain and A. Barron, "An introduction to solar cell technology," *Renewable Energy Data Book*, pp. 56–70, 2011.

[41] M. A. Green, Y. Hishikawa, W. Warta, E. D. Dunlop, D. H. Levi, J. Hohl-Ebinger, and A. W. Ho-Baillie, "Solar cell efficiency tables (version 50)," *Progress in Photovoltaics: Research and Applications*, vol. 25, no. 7, pp. 668–676, 2017.

[42] S. K. Rajput, "Solar energy fundamentals, economic and energy analysis," 2017.

[43] C. Strümpel, M. McCann, G. Beaucarne, V. Arkhipov, A. Slaoui, V. Švrček, C. Del Cañizo, and I. Tobias, "Modifying the solar spectrum to enhance silicon solar cell efficiency—an overview of available materials," *Solar energy materials and solar cells*, vol. 91, no. 4, pp. 238–249, 2007.

[44] Electric4U, "File:solar cell." https://www.electrical4u.com/solar-cell/ 1, February 2020.

[45] M. A. Green, "Third generation photovoltaics: Ultra-high conversion efficiency at low cost," *Progress in Photovoltaics: Research and Applications*, vol. 9, no. 2, pp. 123–135, 2001.

[46] G. Cook, *Photovoltaic fundamentals*. Solar Energy Research Institute, 1991.

[47] J. Schmidt, A. Cuevas, S. Rein, and S. W. Glunz, "Impact of light-induced recombination centres on the current–voltage characteristic of czochralski silicon solar cells," *Progress in Photovoltaics: Research and Applications*, vol. 9, no. 4, pp. 249–255, 2001.

[48] E. Q. Macabebe and E. E. Van Dyk, "Parameter extraction from dark current-voltage characteristics of solar cells," *South African Journal of Science*, vol. 104, no. 9-10, pp. 401–404, 2008.

[49] J. Phang, D. Chan, and J. Phillips, "Accurate analytical method for the extraction of solar cell model parameters," *Electronics Letters*, vol. 20, no. 10, pp. 406–408, 1984.

[50] M. Wolf, G. Noel, and R. J. Stirn, "Investigation of the double exponential in the current—voltage characteristics of silicon solar cells," *IEEE Transactions on electron Devices*, vol. 24, no. 4, pp. 419–428, 1977.

[51] L. Danos, G. Jones, R. Greef, and T. Markvart, "Ultra-thin silicon solar cell: Modelling and characterisation," *physica status solidi c*, vol. 5, no. 5, pp. 1407–1410, 2008.

[52] D. S. Chan and J. C. Phang, "Analytical methods for the extraction of solar-cell single-and double-diode model parameters from iv characteristics," *IEEE Transactions on Electron devices*, vol. 34, no. 2, pp. 286–293, 1987.

[53] S. Glunz, F. Feldmann, A. Richter, M. Bivour, C. Reichel, H. Steinkemper, J. Benick, and M. Hermle, "The irresistible charm of a simple current flow

pattern–25% with a solar cell featuring a full-area back contact," in *Proceedings of the 31st European Photovoltaic Solar Energy Conference and Exhibition*, pp. 259–263, 2015.

[54] D. Adachi, J. L. Hernández, and K. Yamamoto, "Impact of carrier recombination on fill factor for large area heterojunction crystalline silicon solar cell with 25.1% efficiency," *Applied Physics Letters*, vol. 107, no. 23, p. 233506, 2015.

[55] A. Belfar and H. Aït-kaci, "Optimization of band gap and thickness for the development of efficient n-i-p+ solar cell," *JOURNAL OF NANO-AND ELECTRONIC PHYSICS*, vol. Vol. 7 No 2, 02007(7pp) (2015), p. 02007(7pp), 06 2015.

[56] C. Honsberg and S. Bowden, "Photovoltaic education network," *PVEducation. org [accessed 7 August 2019]. http://www. pveducation. org*, 2014.

[57] F. Meillaud, A. Shah, C. Droz, E. Vallat-Sauvain, and C. Miazza, "Efficiency limits for single-junction and tandem solar cells," *Solar energy materials and solar cells*, vol. 90, no. 18-19, pp. 2952–2959, 2006.

[58] T. Markvart and L. Castañer, "Chapter ia-1-principles of solar cell operation," *Sol. Cells (*, pp. 3–25, 2013.

[59] J.-F. Guillemoles, T. Kirchartz, D. Cahen, and U. Rau, "Guide for the perplexed to the shockley–queisser model for solar cells," *Nature photonics*, vol. 13, no. 8, pp. 501–505, 2019.

[60] W. Shockley, "The shockley-queisser limit," *J. Appl. Phys*, vol. 32, pp. 510–519, 1961.

[61] S. Rühle, "Tabulated values of the shockley–queisser limit for single junction solar cells," *Solar Energy*, vol. 130, pp. 139–147, 2016.

[62] A. De Vos and H. Pauwels, "On the thermodynamic limit of photovoltaic energy conversion," *Applied physics*, vol. 25, no. 2, pp. 119–125, 1981.

[63] P. Würfel and U. Würfel, *Physics of solar cells: from basic principles to advanced concepts*. John Wiley & Sons, 2016.

[64] U. Würfel, A. Cuevas, and P. Würfel, "Charge carrier separation in solar cells," *IEEE Journal of Photovoltaics*, vol. 5, no. 1, pp. 461–469, 2014.

[65] P. Asbeck, "Self-absorption effects on the radiative lifetime in gaas-gaalas double heterostructures," *Journal of Applied Physics*, vol. 48, no. 2, pp. 820–822, 1977.

[66] L. C. Hirst and N. J. Ekins-Daukes, "Fundamental losses in solar cells," *Progress in Photovoltaics: Research and Applications*, vol. 19, no. 3, pp. 286–293, 2011.

[67] A. Kingma, "Electrical characterization of low temperature pulsed-electron-deposited cu (in, ga) se2 solar cells," 2018.

[68] A. Martı, L. Cuadra, and A. Luque, "Design constraints of the quantum-dot intermediate band solar cell," *Physica E: Low-dimensional Systems and Nanostructures*, vol. 14, no. 1-2, pp. 150–157, 2002.

[69] Y. Da and Y. Xuan, "Role of surface recombination in affecting the efficiency of nanostructured thin-film solar cells," *Optics express*, vol. 21, no. 106, pp. A1065–A1077, 2013.

[70] D. N. Congreve, J. Lee, N. J. Thompson, E. Hontz, S. R. Yost, P. D. Reusswig, M. E. Bahlke, S. Reineke, T. Van Voorhis, and M. A. Baldo, "External quantum efficiency above 100% in a singlet-exciton-fission–based organic photovoltaic cell," *Science*, vol. 340, no. 6130, pp. 334–337, 2013.

[71] R. Rothemund, "Optical modelling of the external quantum efficiency of solar cells with luminescent down-shifting layers," *Solar energy materials and solar cells*, vol. 120, pp. 616–621, 2014.

[72] J. Nelson, *The physics of solar cells*. World Scientific Publishing Company, 2003.

[73] M. A. Green, "Limits on the open-circuit voltage and efficiency of silicon solar cells imposed by intrinsic auger processes," *IEEE Transactions on electron devices*, vol. 31, no. 5, pp. 671–678, 1984.

[74] T. Tiedje, E. Yablonovitch, G. D. Cody, and B. G. Brooks, "Limiting efficiency of silicon solar cells," *IEEE Transactions on electron devices*, vol. 31, no. 5, pp. 711–716, 1984.

[75] Z. B.V., "Carrier generation and recombination." `http://ecee.colorado.edu/~bart/book/recomb.htm`, July 18 2020.

[76] A. Hangleiter and R. Häcker, "Enhancement of band-to-band auger recombination by electron-hole correlations," *Physical Review Letters*, vol. 65, no. 2, p. 215, 1990.

[77] S. Novikov, "Enhanced bimolecular recombination of charge carriers in amorphous organic semiconductors: Overcoming the langevin limit," *The Journal of Physical Chemistry C*, vol. 123, no. 31, pp. 18854–18860, 2019.

[78] L. Huldt, N. Nilsson, and K. Svantesson, "The temperature dependence of band-to-band auger recombination in silicon," *Applied Physics Letters*, vol. 35, no. 10, pp. 776–777, 1979.

[79] Z. Tang, W. Tress, and O. Inganäs, "Light trapping in thin film organic solar cells," *Materials today*, vol. 17, no. 8, pp. 389–396, 2014.

[80] M. A. Green and S. Pillai, "Harnessing plasmonics for solar cells," *Nature photonics*, vol. 6, no. 3, pp. 130–132, 2012.

[81] E. Moulin, J. Sukmanowski, M. Schulte, A. Gordijn, F. Royer, and H. Stiebig, "Thin-film silicon solar cells with integrated silver nanoparticles," *Thin solid films*, vol. 516, no. 20, pp. 6813–6817, 2008.

[82] W. Foundation, "Localized surface plasmon." https://en.wikipedia.org/wiki/Localized surface plasmon, Aug 2020.

[83] Y. Wu, X.-J. Sun, Y.-P. Jia, and D.-B. Li, "Review of improved spectral response of ultraviolet photodetectors by surface plasmon," *Chinese Physics B*, vol. 27, no. 12, p. 126101, 2018.

[84] B. Singh, M. M. Shabat, and D. M. Schaadt, "Analytical modeling of power transfer via metallic nanoparticles in a solar cell absorber," *Journal of Quantitative Spectroscopy and Radiative Transfer*, vol. 243, p. 106807, 2020.

[85] X. Chen, B. Jia, J. K. Saha, B. Cai, N. Stokes, Q. Qiao, Y. Wang, Z. Shi, and M. Gu, "Broadband enhancement in thin-film amorphous silicon solar cells enabled by nucleated silver nanoparticles," *Nano letters*, vol. 12, no. 5, pp. 2187–2192, 2012.

[86] K. Tanabe, "A review of ultrahigh efficiency iii-v semiconductor compound solar cells: multijunction tandem, lower dimensional, photonic up/down conversion and plasmonic nanometallic structures," *Energies*, vol. 2, no. 3, pp. 504–530, 2009.

[87] X. Ren, J. Cheng, S. Zhang, X. Li, T. Rao, L. Huo, J. Hou, and W. C. Choy, "High efficiency organic solar cells achieved by the simultaneous plasmon-optical and plasmon-electrical effects from plasmonic asymmetric modes of gold nanostars," *Small*, vol. 12, no. 37, pp. 5200–5207, 2016.

[88] S. D. Standridge, G. C. Schatz, and J. T. Hupp, "Toward plasmonic solar cells: protection of silver nanoparticles via atomic layer deposition of tio2," *Langmuir*, vol. 25, no. 5, pp. 2596–2600, 2009.

[89] M. K. Gangishetty, K. E. Lee, R. W. Scott, and T. L. Kelly, "Plasmonic enhancement of dye sensitized solar cells in the red-to-near-infrared region using triangular core–shell ag@ sio2 nanoparticles," *ACS applied materials & interfaces*, vol. 5, no. 21, pp. 11044–11051, 2013.

[90] W. Zhang, M. Saliba, S. D. Stranks, Y. Sun, X. Shi, U. Wiesner, and H. J. Snaith, "Enhancement of perovskite-based solar cells employing core–shell metal nanoparticles," *Nano letters*, vol. 13, no. 9, pp. 4505–4510, 2013.

[91] C. Wen, K. Ishikawa, M. Kishima, and K. Yamada, "Effects of silver particles on the photovoltaic properties of dye-sensitized tio2 thin films," *Solar Energy Materials and Solar Cells*, vol. 61, no. 4, pp. 339–351, 2000.

[92] H. Choi, W. T. Chen, and P. V. Kamat, "Know thy nano neighbor. plasmonic versus electron charging effects of metal nanoparticles in dye-sensitized solar cells," *ACS nano*, vol. 6, no. 5, pp. 4418–4427, 2012.

[93] H. Elbohy, M. R. Kim, A. Dubey, K. M. Reza, D. Ma, J. Zai, X. Qian, and Q. Qiao, "Incorporation of plasmonic au nanostars into photoanodes for high efficiency dye-sensitized solar cells," *Journal of Materials Chemistry A*, vol. 4, no. 2, pp. 545–551, 2016.

[94] X. Ma, B. Ma, T. Yu, X. Xu, L. Zhang, W. Wang, K. Cao, L. Deng, S. Chen, and W. Huang, "Indepth studies on working mechanism of plasmon-enhanced inverted perovskite solar cells incorporated with ag@ sio2 core–shell nanocubes," *ACS Applied Energy Materials*, vol. 2, no. 5, pp. 3605–3613, 2019.

[95] P. Yu, Y. Yao, J. Wu, X. Niu, A. L. Rogach, and Z. Wang, "Effects of plasmonic metal core-dielectric shell nanoparticles on the broadband light absorption enhancement in thin film solar cells," *Scientific reports*, vol. 7, no. 1, pp. 1–10, 2017.

[96] F. Farahi, "Waveguide assisted solar energy harvesting," June 11 2013. US Patent 8,463,092.

[97] K. Bittkau, A. Hoffmann, U. W. Paetzold, and R. Carius, "Broadening of light coupling to waveguide modes in solar cells by disordered grating textures," *Applied Sciences*, vol. 7, no. 7, p. 725, 2017.

[98] H. Wang, X. Liu, L. Wang, and Z. Zhang, "Anisotropic optical properties of silicon nanowire arrays based on the effective medium approximation," *International Journal of Thermal Sciences*, vol. 65, pp. 62–69, 2013.

[99] M. Born and E. Wolf, *Principles of optics: electromagnetic theory of propagation, interference and diffraction of light*. Elsevier, 2013.

[100] H. Hamouche, M. M. Shabat, and D. M. Schaadt, "Multilayer solar cell waveguide structures containing metamaterials," *Superlattices and Microstructures*, vol. 101, pp. 633–640, 2017.

[101] L. Fang, L. Danos, and T. Markvart, "Solar cell as a waveguide: quantum efficiency of ultrathin crystalline silicon solar cell," 2013.

[102] K. Okamoto, *Fundamentals of optical waveguides*. Academic press, 2006.

[103] N. a Nanotechnology Company, "$cu@sio_2$ core shell nanoparticles less price high purity fast delivery - nanoshel."

[104] M. Quinten, *Optical properties of nanoparticle systems: Mie and beyond*. John Wiley & Sons, 2010.

[105] R. Jin, Y. Cao, C. A. Mirkin, K. L. Kelly, G. C. Schatz, and J. Zheng, "Photoinduced conversion of silver nanospheres to nanoprisms," *science*, vol. 294, no. 5548, pp. 1901–1903, 2001.

[106] H. Suzuki, S. I-Yin, *et al.*, "Calculation of the mie scattering field inside and outside a coated spherical particle," *International Journal of Physical Sciences*, vol. 3, no. 1, pp. 38–41, 2008.

[107] S. Jacquier and F. Gruy, "Application of scattering theories to the characterization of precipitation processes," in *Light Scattering Reviews 5*, pp. 37–78, Springer, 2010.

[108] L. Novotny and B. Hecht, *Principles of nano-optics*. Cambridge university press, 2012.

[109] C. F. Bohren and D. R. Huffman, *Absorption and scattering of light by small particles*. John Wiley & Sons, 2008.

[110] W. He and M. Zhao, "The application of bessel function in the definite solution problem of cylindrical coordinate system," *Applied and Computational Mathematics*, vol. 8, no. 3, pp. 58–64, 2019.

[111] S. F. Shayesteh and M. Saie, "The effect of surface plasmon resonance on optical response in dielectric (core)–metal (shell) nanoparticles," *Pramana*, vol. 85, no. 6, pp. 1245–1255, 2015.

[112] N. K. Grady, N. J. Halas, and P. Nordlander, "Influence of dielectric function properties on the optical response of plasmon resonant metallic nanoparticles," *Chemical Physics Letters*, vol. 399, no. 1-3, pp. 167–171, 2004.

[113] J. R. Heath, C. M. Knobler, and D. V. Leff, "Pressure/temperature phase diagrams and superlattices of organically functionalized metal nanocrystal monolayers: the influence of particle size, size distribution, and surface passivant," *The Journal of Physical Chemistry B*, vol. 101, no. 2, pp. 189–197, 1997.

[114] S. Link and M. A. El-Sayed, "Spectral properties and relaxation dynamics of surface plasmon electronic oscillations in gold and silver nanodots and nanorods," 1999.

[115] B. Luk'yanchuk, N. I. Zheludev, S. A. Maier, N. J. Halas, P. Nordlander, H. Giessen, and C. T. Chong, "The fano resonance in plasmonic nanostructures and metamaterials," *Nature materials*, vol. 9, no. 9, pp. 707–715, 2010.

[116] R. M. Bozorth, "Ferromagnetism," *Ferromagnetism, by Richard M. Bozorth, pp. 992. ISBN 0-7803-1032-2. Wiley-VCH, August 1993.*, p. 992, 1993.

[117] S. Bedanta and W. Kleemann, "Supermagnetism," *Journal of Physics D: Applied Physics*, vol. 42, no. 1, p. 013001, 2008.

[118] J. C. Maxwell, *A dynamical theory of the electromagnetic field*. Wipf and Stock Publishers, 1996.

[119] B. H. Gaury and P. M. Haney, "Sesame (software release and documentation)," tech. rep., 2019.

[120] S. Soedergren, A. Hagfeldt, J. Olsson, and S.-E. Lindquist, "Theoretical models for the action spectrum and the current-voltage characteristics of microporous semiconductor films in photoelectrochemical cells," *The Journal of Physical Chemistry*, vol. 98, no. 21, pp. 5552–5556, 1994.

[121] A. Quandt, T. Aslan, I. Mokgosi, R. Warmbier, M. Ferrari, and G. Righini, "About the implementation of frequency conversion processes in solar cell device simulations," *Micromachines*, vol. 9, no. 9, p. 435, 2018.

[122] S. I. Data and C. O. Power, "Oriel product training,"

[123] S. Nagamani, G. Kumarasamy, M. Song, C. S. Kim, D.-H. Kim, S. Y. Ryu, J.-W. Kang, and S.-H. Jin, "Optical absorption and electrical properties of enhanced efficiency in organic solar cells as interfacial layer with au nps," *Synthetic Metals*, vol. 217, pp. 117–122, 2016.

[124] E. Petryayeva and U. J. Krull, "Localized surface plasmon resonance: Nanostructures, bioassays and biosensing—a review," *Analytica chimica acta*, vol. 706, no. 1, pp. 8–24, 2011.

[125] H. Ran, J. Fan, X. Zhang, J. Mao, and G. Shao, "Enhanced performances of dye-sensitized solar cells based on au-tio2 and ag-tio2 plasmonic hybrid nanocomposites," *Applied Surface Science*, vol. 430, pp. 415–423, 2018.

[126] K. Guo, M. Li, X. Fang, X. Liu, Y. Zhu, Z. Hu, and X. Zhao, "Enhancement of properties of dye-sensitized solar cells by surface plasmon resonance of ag nanowire core–shell structure in tio 2 films," *Journal of Materials Chemistry A*, vol. 1, no. 24, pp. 7229–7234, 2013.

[127] H. Jiang, H. Dai, J. Deng, Y. Liu, L. Zhang, and K. Ji, "Porous f-doped bivo4: Synthesis and enhanced photocatalytic performance for the degradation of phenol under visible-light illumination," *Solid state sciences*, vol. 17, pp. 21–27, 2013.

[128] W. Stöber, A. Fink, and E. Bohn, "Controlled growth of monodisperse silica spheres in the micron size range," *Journal of colloid and interface science*, vol. 26, no. 1, pp. 62–69, 1968.

[129] G. Bogush, M. Tracy, and C. Zukoski Iv, "Preparation of monodisperse silica particles: control of size and mass fraction," *Journal of non-crystalline solids*, vol. 104, no. 1, pp. 95–106, 1988.

[130] P. Dražar, "Levy david, zayat marcos (ed.): The sol-gel handbook: Synthesis, characterization and applications," *Chemické listy*, vol. 110, no. 3, pp. 229–230, 2016.

[131] A. A. Issa and A. S. Luyt, "Kinetics of alkoxysilanes and organoalkoxysilanes polymerization: a review," *Polymers*, vol. 11, no. 3, p. 537, 2019.

[132] G. Bogush and C. Zukoski Iv, "Studies of the kinetics of the precipitation of uniform silica particles through the hydrolysis and condensation of silicon alkoxides," *Journal of Colloid and Interface Science*, vol. 142, no. 1, pp. 1–18, 1991.

[133] t. f. e. Wikipedia, "File:stöber process." https://en.wikipedia.org/wiki/St%C3%B6ber_process#cite_note-Stober-1, 2019.

[134] I. A. Ibrahim, A. Zikry, and M. A. Sharaf, "Preparation of spherical silica nanoparticles: Stober silica," *J. Am. Sci*, vol. 6, no. 11, pp. 985–989, 2010.

[135] A. M. Michaels, J. Jiang, and L. Brus, "Ag nanocrystal junctions as the site for surface-enhanced raman scattering of single rhodamine 6g molecules," *The Journal of Physical Chemistry B*, vol. 104, no. 50, pp. 11965–11971, 2000.

[136] M. J. de Dood, B. Berkhout, C. M. van Kats, A. Polman, and A. van Blaaderen, "Acid-based synthesis of monodisperse rare-earth-doped colloidal sio2 spheres," *Chemistry of materials*, vol. 14, no. 7, pp. 2849–2853, 2002.

[137] E. R. Encina and E. A. Coronado, "On the far field optical properties of ag-au nanosphere pairs," *The Journal of Physical Chemistry C*, vol. 114, no. 39, pp. 16278–16284, 2010.

[138] J. Ye, B. Van de Broek, R. De Palma, W. Libaers, K. Clays, W. Van Roy, G. Borghs, and G. Maes, "Surface morphology changes on silica-coated gold colloids," *Colloids and Surfaces A: Physicochemical and Engineering Aspects*, vol. 322, no. 1-3, pp. 225–233, 2008.

[139] M. Lismont, C. A. Páez, and L. Dreesen, "A one-step short-time synthesis of ag@ sio2 core–shell nanoparticles," *Journal of colloid and interface science*, vol. 447, pp. 40–49, 2015.

[140] G. Bogush and C. Zukoski Iv, "Uniform silica particle precipitation: an aggregative growth model," *Journal of colloid and interface science*, vol. 142, no. 1, pp. 19–34, 1991.

[141] J. Bailey and M. Mecartney, "Formation of colloidal silica particles from alkoxides," *Colloids and Surfaces*, vol. 63, no. 1-2, pp. 151–161, 1992.

[142] H. Boukari, J. Lin, and M. Harris, "Small-angle x-ray scattering study of the formation of colloidal silica particles from alkoxides: primary particles or not?," *Journal of colloid and interface science*, vol. 194, no. 2, pp. 311–318, 1997.

[143] Y. Lu, Y. Yin, Z.-Y. Li, and Y. Xia, "Synthesis and self-assembly of au@sio2 core- shell colloids," *Nano Letters*, vol. 2, no. 7, pp. 785–788, 2002.

[144] J.-L. Gong, J.-H. Jiang, Y. Liang, G.-L. Shen, and R.-Q. Yu, "Synthesis and characterization of surface-enhanced raman scattering tags with ag/sio2 core–shell nanostructures using reverse micelle technology," *Journal of colloid and interface science*, vol. 298, no. 2, pp. 752–756, 2006.

[145] K. N'Konou, M. Chalh, V. Monnier, N. P. Blanchard, Y. Chevolot, B. Lucas, S. Vedraine, and P. Torchio, "Impact of ag@ sio2 core-shell nanoparticles on the photoelectric current of plasmonic inverted organic solar cells," *Synthetic Metals*, vol. 239, pp. 22–28, 2018.

[146] S. Vedraine, P. Torchio, A. Merlen, J. Bagierek, F. Flory, A. Sangar, and L. Escoubas, "Optical characterization of organic blend films integrating metallic

nanoparticles," *Solar Energy Materials and Solar Cells*, vol. 102, pp. 31–35, 2012.

[147] D. Kalyane, N. Kumar, N. Anup, K. Rajpoot, R. Maheshwari, P. Sengupta, K. Kalia, and R. K. Tekade, "Recent advancements and future submissions of silica core-shell nanoparticles," *International Journal of Pharmaceutics*, vol. 609, p. 121173, 2021.

[148] R. Ws, "Imagej," *US National Institutes of Health*, vol. 2007, 1997.

[149] C. Lopez, "Materials aspects of photonic crystals," *Advanced Materials*, vol. 15, pp. 1679 – 1704, 10 2003.

[150] L. Scriven, "Physics and applications of dip coating and spin coating," *MRS Online Proceedings Library (OPL)*, vol. 121, 1988.

[151] M. Brust, M. Walker, D. Bethell, D. J. Schiffrin, and R. Whyman, "Synthesis of thiol-derivatised gold nanoparticles in a two-phase liquid–liquid system," *Journal of the Chemical Society, Chemical Communications*, no. 7, pp. 801–802, 1994.

[152] R. T. Tom, A. S. Nair, N. Singh, M. Aslam, C. Nagendra, R. Philip, K. Vijayamohanan, and T. Pradeep, "Freely dispersible au@ tio2, au@ zro2, ag@ tio2, and ag@ zro2 core- shell nanoparticles: one-step synthesis, characterization, spectroscopy, and optical limiting properties," *Langmuir*, vol. 19, no. 8, pp. 3439–3445, 2003.

[153] K. Dhanalekshmi, K. Meena, and I. Ramesh, "Synthesis and characterization of ag@ tio2 core-shell nanoparticles and study of its antibacterial activity," *Int J Nanotechnol*, vol. 3, no. 5, p. 9, 2013.

[154] H. Baida, P. Billaud, S. Marhaba, D. Christofilos, E. Cottancin, A. Crut, J. Lerme, P. Maioli, M. Pellarin, M. Broyer, *et al.*, "Quantitative determination of the size dependence of surface plasmon resonance damping in single ag@ sio2 nanoparticles," *Nano letters*, vol. 9, no. 10, pp. 3463–3469, 2009.

[155] M. N. Polyanskiy, "Refractive index database." https://refractiveindex.info. Accessed on 2021-06-13.

[156] K. R. Raj and P. Murugakoothan, "Studies on the optical and mechanical properties of non-linear optical 3-aminophenol orthophosphoric acid (3-amphph) single crystal," *Optik*, vol. 123, no. 12, pp. 1082–1086, 2012.

[157] M. Green, "Thin-film solar cells: Review of materials, technologies and commercial status," *Journal of Materials Science: Materials in Electronics*, vol. 18, pp. 15–19, 01 2007.

[158] C. Droz, E. Vallat-Sauvain, J. Bailat, L. Feitknecht, J. Meier, and A. Shah, "Relationship between raman crystallinity and open-circuit voltage in microcrystalline silicon solar cells," *Solar Energy Materials and Solar Cells*, vol. 81, no. 1, pp. 61–71, 2004.

[159] A. Shah, H. Schade, M. Vanecek, J. Meier, E. Vallat-Sauvain, N. Wyrsch, U. Kroll, C. Droz, and J. Bailat, "Thin-film silicon solar cell technology," *Progress in photovoltaics: Research and applications*, vol. 12, no. 2-3, pp. 113–142, 2004.

[160] S. De, A. Ghosh, D. Sil, P. Sinha, and M. Bera, "Effect of surface recombination on the transit-time in heavily doped n+-p junction silicon solar cell," *Solid-state electronics*, vol. 38, no. 6, pp. 1270–1272, 1995.

[161] E. Tuominen, M. Acerbis, A. Hovinen, T. Siirtola, and J. Sinkkonen, "A method extracting solar cell parameters from spectral response by inverse laplace transform," *Physica Scripta*, vol. 1997, no. T69, p. 306, 1997.

[162] N. Li, B. E. Lassiter, R. R. Lunt, G. Wei, and S. R. Forrest, "Open circuit voltage enhancement due to reduced dark current in small molecule photovoltaic cells," *Applied Physics Letters*, vol. 94, no. 2, p. 13, 2009.

[163] C. M. Proctor and T.-Q. Nguyen, "Effect of leakage current and shunt resistance on the light intensity dependence of organic solar cells," *Applied Physics Letters*, vol. 106, no. 8, p. 23_1, 2015.

[164] D. Rosenblatt, A. Sharon, and A. A. Friesem, "Resonant grating waveguide structures," *IEEE Journal of Quantum electronics*, vol. 33, no. 11, pp. 2038–2059, 1997.

[165] S. Wang, R. Magnusson, J. S. Bagby, and M. Moharam, "Guided-mode resonances in planar dielectric-layer diffraction gratings," *JOSA A*, vol. 7, no. 8, pp. 1470–1474, 1990.

[166] Y.-C. Lee, C.-F. Huang, J.-Y. Chang, and M.-L. Wu, "Enhanced light trapping based on guided mode resonance effect for thin-film silicon solar cells with two filling-factor gratings," *Optics Express*, vol. 16, no. 11, pp. 7969–7975, 2008.

[167] P. M. Blanchard, D. J. Fisher, S. C. Woods, and A. H. Greenaway, "Phase-diversity wave-front sensing with a distorted diffraction grating," *Applied optics*, vol. 39, no. 35, pp. 6649–6655, 2000.

[168] M. Srinivasarao, "Nano-optics in the biological world: beetles, butterflies, birds, and moths," *Chemical reviews*, vol. 99, no. 7, pp. 1935–1962, 1999.

[169] V. E. Ferry, M. A. Verschuuren, M. C. v. Lare, R. E. I. Schropp, H. A. Atwater, and A. Polman, "Optimized spatial correlations for broadband light trapping nanopatterns in high efficiency ultrathin film a-si:h solar cells," *Nano Letters*, vol. 11, no. 10, pp. 4239–4245, 2011. PMID: 21875103.

[170] U. Paetzold, E. Moulin, D. Michaelis, W. Böttler, C. Wächter, V. Hagemann, M. Meier, R. Carius, and U. Rau, "Plasmonic reflection grating back contacts for microcrystalline silicon solar cells," *Applied Physics Letters*, vol. 99, no. 18, p. 181105, 2011.

[171] S. Rühle, S. Greenwald, E. Koren, and A. Zaban, "Optical waveguide enhanced photovoltaics," *Optics Express*, vol. 16, no. 26, pp. 21801–21806, 2008.

[172] T. Khaleque and R. Magnusson, "Light management through guided-mode resonances in thin-film silicon solar cells," *Journal of Nanophotonics*, vol. 8, no. 1, p. 083995, 2014.

[173] R. Dewan and D. Knipp, "Light trapping in thin-film silicon solar cells with integrated diffraction grating," *Journal of Applied Physics*, vol. 106, no. 7, p. 074901, 2009.

[174] S. Wang and R. Magnusson, "Theory and applications of guided-mode resonance filters," *Applied optics*, vol. 32, no. 14, pp. 2606–2613, 1993.

[175] M. Saleem, P. Stenberg, T. Alasaarela, P. Silfsten, M. Khan, S. Honkanen, and J. Turunen, "Towards athermal organic-inorganic guided mode resonance filters," *Optics express*, vol. 19, no. 24, pp. 24241–24251, 2011.

[176] S. Tibuleac and R. Magnusson, "Diffractive narrow-band transmission filters based on guided-mode resonance effects in thin-film multilayers," *IEEE photonics technology letters*, vol. 9, no. 4, pp. 464–466, 1997.

[177] M. R. Saleem, S. Honkanen, and J. Turunen, "Effect of substrate overetching and heat treatment of titanium oxide waveguide gratings and thin films on their optical properties," *Applied optics*, vol. 52, no. 3, pp. 422–432, 2013.

[178] M. S. Badar and M. R. Saleem, "Improved absorption efficiency of silicon (si) solar cells through resonant waveguide gratings (rwgs)–a hybrid design of rwg and si solar cell," *Optik*, vol. 128, pp. 50–56, 2017.

[179] W. Chegal, H. M. Cho, Y. jai Cho, and H. Du Cheong, "Analysis of guided-mode resonant grating filters by using a rigorous coupled-wave method," *Journal of the Korean Physical Society*, vol. 59, no. 2, pp. 326–331, 2011.

[180] Z. Zhang, S. Ito, B. O'Regan, D. Kuang, S. M. Zakeeruddin, P. Liska, R. Charvet, P. Comte, M. K. Nazeeruddin, P. Pechy, *et al.*, "The electronic role of the tio2 light-scattering layer in dye-sensitized solar cells," *Zeitschrift für physikalische chemie*, vol. 221, no. 3, pp. 319–327, 2007.

[181] L. Huang, B. Dong, X. Guo, Y. Chang, N. Chen, X. Huang, W. Liao, C. Zhu, H. Wang, C. Lee, *et al.*, "Waveguide-integrated black phosphorus photodetector for mid-infrared applications," *ACS nano*, vol. 13, no. 1, pp. 913–921, 2018.

[182] S. H. Badri, M. Gilarlue, and S. Gavgani, "Ultra-thin silicon-on-insulator waveguide bend based on truncated eaton lens implemented by varying the guiding layer thickness," *Photonics and Nanostructures-Fundamentals and Applications*, vol. 39, p. 100766, 2020.

[183] M. Agrawal and P. Peumans, "Broadband optical absorption enhancement through coherent light trapping in thin-film photovoltaic cells," *Optics express*, vol. 16, no. 8, pp. 5385–5396, 2008.

[184] B. J. Soller, H. R. Stuart, and D. G. Hall, "Energy transfer at optical frequencies to silicon-on-insulator structures," *Optics Letters*, vol. 26, no. 18, pp. 1421–1423, 2001.

[185] S. Pillai, , and M. Green, "Plasmonics for photovoltaic applications," *Solar Energy Materials and Solar Cells*, vol. 94, no. 9, pp. 1481–1486, 2010.

[186] N. C. Panoiu and R. M. Osgood Jr, "Enhanced optical absorption for photovoltaics via excitation of waveguide and plasmon-polariton modes," *Optics letters*, vol. 32, no. 19, pp. 2825–2827, 2007.

[187] S.-B. Rim, S. Zhao, S. R. Scully, M. D. McGehee, and P. Peumans, "An effective light trapping configuration for thin-film solar cells," *Applied Physics Letters*, vol. 91, no. 24, p. 243501, 2007.

[188] F. Lemarchand, A. Sentenac, E. Cambril, and H. Giovannini, "Study of the resonant behaviour of waveguide gratings: increasing the angular tolerance of guided-mode filters," *Journal of Optics A: Pure and Applied Optics*, vol. 1, no. 4, p. 545, 1999.

[189] T. Petrova, Y. N. Ponomarev, A. Solodov, A. Solodov, E. Glazkova, O. Bakina, and M. Lerner, "Absorption spectra of ethylene in different sio2/al2o3 aero-

gels," in *22nd International Symposium on Atmospheric and Ocean Optics: Atmospheric Physics*, vol. 10035, p. 100350N, International Society for Optics and Photonics, 2016.

[190] J. Wang, L. Yang, Z.-D. Hu, W. He, and G. Zheng, "Analysis of graphene-based multilayer comb-like absorption system based on multiple waveguide theory," *IEEE Photonics Technology Letters*, vol. 31, no. 7, pp. 561–564, 2019.

[191] M. Jerman, Z. Qiao, and D. Mergel, "Refractive index of thin films of sio 2, zro 2, and hfo 2 as a function of the films' mass density," *Applied optics*, vol. 44, no. 15, pp. 3006–3012, 2005.

[192] E. Chason, J. Shin, S. Hearne, and L. Freund, "Kinetic model for dependence of thin film stress on growth rate, temperature, and microstructure," *Journal of Applied Physics*, vol. 111, no. 8, p. 083520, 2012.

[193] N. Wostbrock and T. Busani, "Stress and refractive index control of sio2 thin films for suspended waveguides," *Nanomaterials*, vol. 10, no. 11, p. 2105, 2020.

[194] B. Parida, S. Iniyan, and R. Goic, "A review of solar photovoltaic technologies," *Renewable and sustainable energy reviews*, vol. 15, no. 3, pp. 1625–1636, 2011.

[195] Z.-Y. Huang, S.-W. Chiu, C.-W. Chen, Y.-H. Chen, L.-Y. Lin, K.-T. Wong, and H.-W. Lin, "Spontaneous formation of light-trapping nano-structures for top-illumination organic solar cells," *Nanoscale*, vol. 6, no. 4, pp. 2316–2320, 2014.

[196] D. Derkacs, S. Lim, P. Matheu, W. Mar, and E. Yu, "Improved performance of amorphous silicon solar cells via scattering from surface plasmon polaritons in nearby metallic nanoparticles," *Applied Physics Letters*, vol. 89, no. 9, p. 093103, 2006.

[197] K. Roy, S. Mukhopadhyay, and H. Mahmoodi-Meimand, "Leakage current mechanisms and leakage reduction techniques in deep-submicrometer cmos circuits," *Proceedings of the IEEE*, vol. 91, no. 2, pp. 305–327, 2003.

[198] G. V. Aguilar, "Introductory chapter: A brief semblance of the sol-gel method in research," in *Sol-Gel Method-Design and Synthesis of New Materials with Interesting Physical, Chemical and Biological Properties*, IntechOpen, 2018.

[199] A. I. G. Varela, M. Aymerich, D. N. García, Y. C. Martín, P. A. de Beule, E. Álvarez, C. Bao-Varela, and M. T. Flores-Arias, "Sol-gel glass coating synthesis for different applications: Active gradient-index materials, microlens arrays and biocompatible channels," *Recent Applications in Sol-Gel Synthesis*, p. 231, 2017.

Appendix A

Techniques and methods applied

A.1 Experimental techniques

A.1.1 Sol-gel method

Sol-gel is one of the most straightforward and widely used methods for producing thin films from a wide range of inorganic, hybrid, and nanocomposite materials. Metal oxides, especially those of silicon (*Si*) and titania (*Ti*), are made using this process. The method entails converting monomers into a colloidal solution (*sol*), which serves as a precursor for forming an interconnected network (or *gel*) of discrete particles or network polymers. It allows for a high level of control over crucial parameters as well as a level of versatility not possible with other traditional techniques, as it allows for the coating of a wide range of substrates and complex geometries, including substrates with holes or complicated shapes.

Figure A.1 provides a schematization of the reaction steps involved in the sol-gel synthesis, as well as a summary of the final products that could be obtained according to the variation in processing parameters. Sol-gel monoliths could be produced by *(i)* gelation of a solution of colloidal powders, *(ii)* hydrolysis and poly-condensation of alkoxide or nitrate precursors followed by hypercritical drying of the gel, or *(iii)* hydrolysis and poly- condensation of alkoxide precursors followed by aging and drying under ambient atmosphere. Sol-gel glasses are mainly produced by the third approach, which typically comprises 7 reaction steps (see figure A.1).

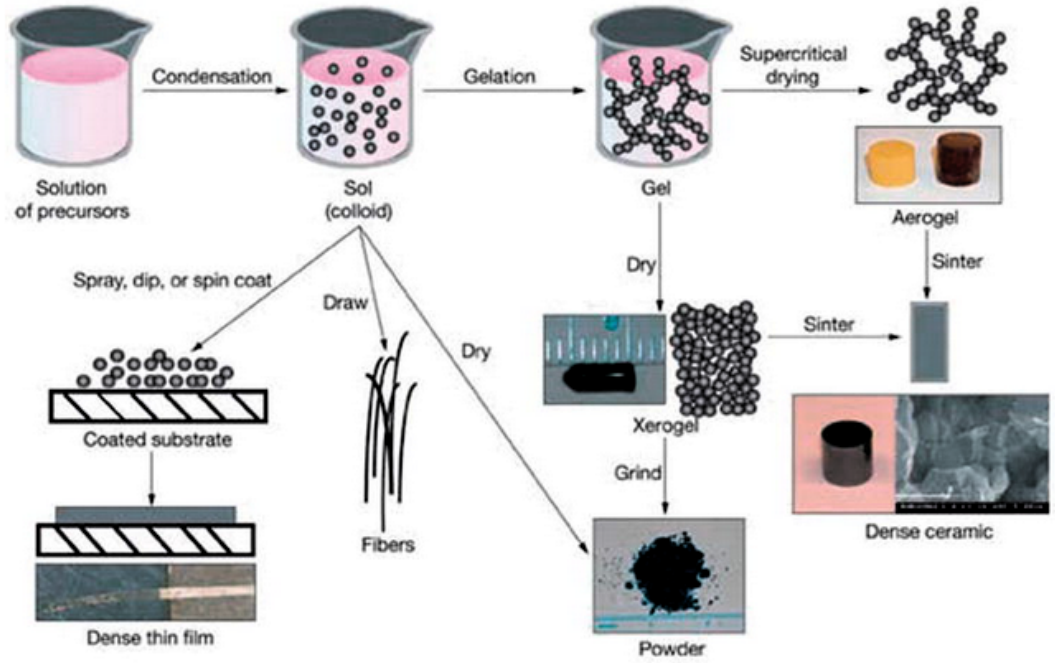


Figure A.1: Schematic representation of the different stages and routes of the sol–gel technology [198]

A.1.2 Depositing methods

Dip-coating, spin-coating, spray-coating, and flow-coating are only a few of the wet thin film coating techniques available. However, spin coating and dip coating were also considered in this project.

The spin coater was set to 2000 to 6000 revolutions per minute (rpm). The following conditions were set for the dip coater:

1. V_{up} = 25 mm/min
2. V_{dowm} = 25 mm/ min
3. Dip time = 6 sec
4. Distance = 150 mm
5. Room Temperature

and there are stages of dip coating that are schematically represented in Figure A.2,

such as controlled dipping and immersing speed.

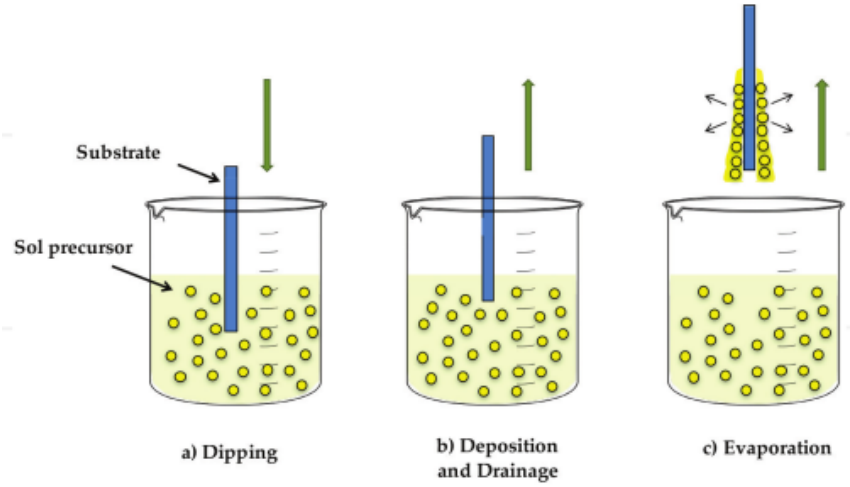


Figure A.2: Sequential stages of the dip-coating technique for thin film deposition: (a) the substrate is dipped and immersed in the sol precursor, (b) the substrate is withdrawn at constant speed rate, and (c) solvent evaporation yields to the gelation of the layer. [199]

Before we can start laying down layers, we must first set the atmospheric conditions. Then set the immersing speed at which the substrate to be coated would be immersed in the initial solution before being removed at a constant speed. Specifically, we can monitor the evaporation conditions by adjusting the withdrawal speed, allowing us to fine-tune film characteristics such as thickness, optical constants and inner structure. Because of the combined effects of viscosity, the substrate has a homogeneous surface. Evaporation occurs at the end of the operation, resulting in the gelation of the film. The coated substrates are then given a thermal treatment. [199].

A.2 Data analysis techniques

A.2.1 The UV-Vis spectrophotometer analysis

In order to do the optical measurement such as absorption, reflectance and transmission, the UV-Vis-NIR spectrophotometer Cary 5000 which is a high performance photometric in the 175-3300 *nm* range was used. Using a *Pb*-Smart detector, the Cary 5000 extends its *NIR* range to 3300 *nm*. It's an important tool for materials science research because of this. The Cary WinUV software, a modular Windows-based software that makes it simple to perform powerful analysis and monitor a variety of optional accessories, is controlled by the Cary WinUV software. Large accessories and integrating spheres for spectral and diffuse reflectance can be stored in the large sample compartment, which can be enlarged.

A Zero/Baseline Correction is applied before analyzing any samples, where a 100%T baseline correction (100%TBaseline) and a zero-line correction (0%TBaseline) to the sample scan (S) is performed with the raw transmission data and is given by:

$$\frac{(S-0\%TBaseline)}{(100\%TBaseline-0\%TBaseline)} \tag{A.1}$$

Where the instrument will perform a 100%TBaseline first, followed by a 0%TBaseline when performing a baseline collection.

A.2.2 *I-V* characteristics of photovoltaic device analysis

After incorporating the *a-Si* solar cells with *Ag/Au NPs*, SiO_2, TiO_2 nanospheres, $Ag@SiO_2$, $Ag@SiO_2$ core-shell *NPs* and silica waveguides, the *I–V* characterization was performed using the solar simulator for the performance of the solar cell. The standards measurement for device testing are:

1. Air mass 1.5 spectrum (AM1.5) for terrestrial cells and Air Mass 0 (AM0) for for

space cells,

2. Intensity of 100 mW/cm^2 (1 kW/m^2, one-sun of illumination)
3. Cell temperature of 25 $^{\circ}C$ (not 300 K),
4. Area illuminated is 2.2 cm^2.